

https://dspace.org/

Insighhts into hot deformation of medium entropy alloys Softening mechanisms microstructural evolution and constitutive modellinga comprehensive review

S.A Kareem; J.U Anaele; O.F Olanrewaju; E.D Adewale; N.C Osondu-Okoro ...

https://hdl.handle.net/10539/41153
WOS

Downloaded from a DSpace repository. https://dspace.org/

Journal of Materials Research and Technology 29 (2024) 5369–5401

Contents lists available at ScienceDirect

Journal of Materials Research and Technology

journal homepage: www.elsevier.com/locate/jmrt

Insights into hot deformation of medium entropy alloys: Softening mechanisms, microstructural evolution, and constitutive modelling—a comprehensive review

Sodiq Abiodun Kareem [a,*], Justus Uchenna Anaele [b], Olajesu Favor Olanrewaju [a,e], Esther Dolapo Adewale [a], Nkemakolam Chikodinaka Osondu-Okoro [b], Emmanuel Omosegunfunmi Aikulola [a], Samuel Olumide Falana [a], Bharat Gwalani [f], Michael Oluwatosin Bodunrin [c], Kenneth Kanayo Alaneme [a,d]

[a] Materials Design and Structural Integrity Group, Department of Metallurgical and Materials Engineering, Federal University of Technology Akure, P.M.B. 704, Ondo State, Nigeria
[b] Department of Metallurgical and Materials Engineering, Federal University of Technology, Owerri, Nigeria
[c] School of Chemical and Metallurgical Engineering, University of the Witwatersrand, Johannesburg 2050, South Africa
[d] Centre for Nanoengineering and Tribocorrosion, School of Mining, Metallurgy and Chemical Engineering, Faculty of Engineering & the Built Environment, University of Johannesburg, South Africa
[e] Department of Material Science and Engineering, Iowa State University, AMES, IA 50011, United States
[f] Materials Science and Engineering, North Carolina State University, Raleigh, NC, 27695-7907, United States

ARTICLE INFO

Keywords:
Medium entropy alloys
Hot deformation
Dynamic recrystallization
Processing maps
Constitutive modelling

ABSTRACT

The recent discovery of multicomponent principal alloys and the enhanced comprehension of their physical metallurgy have significantly advanced the understanding of microstructure engineering and material selection for high-tech applications. The exceptional combination of characteristics found in MEAs can be attributed to their distinctive phase constitution, which is aided by their multi-principal constituents. These properties are seldom encountered in ordinary alloys. Nevertheless, the use of these materials in their as-cast state is challenging due to issues such as the presence of heterogeneity in their chemical makeup, shrinkage porosity, unrefined dendritic structure, and the presence of a quasi-stable eutectic at grain boundaries. Consequently, the utilization of hot deformation methods for the purpose of achieving uniform and refined microstructures in as-cast MEAs has garnered significant interest as a viable approach to address these limitations. This review provides a comprehensive summary of the hot deformation characteristics of MEAs. Factors such as the alloy composition, the phase constituent, deformation parameters and recrystallization mechanisms were observed to influence the microstructural development and phase transition, flow curve characteristics, and mechanical characteristics of MEAs. Additionally, the use of processing map analysis for the determination of optimal processing zones for the hot deformation of MEAs was appraised. The discussion also encompassed the constitutive model description, molecular dynamics modeling, and machine learning algorithm for the prediction of the governing deformation mechanism and the deformation flow stress. Finally, future research directions are suggested.

1. Introduction

In 2004, the field of materials science witnessed remarkable strides as researchers delved into the unchartered territory of hyper-dimensional composition space [1]. This breakthrough materialized through the development of an innovative strategy for crafting metallic systems with intricate compositions yet no complex microstructures, marking a transformative shift in materials design. In the past, metallic alloys were often composed of one or two primary elements, along with many secondary alloying elements [1,2]. These minor elements were included in the alloy at concentrations as low as a few atomic ratios with the intention of improving the material's characteristics [2,3]. This alloy

* Corresponding author.
E-mail address: sodiqabiodunkareem@gmail.com (S.A. Kareem).

https://doi.org/10.1016/j.jmrt.2024.03.011
Received 1 December 2023; Received in revised form 15 February 2024; Accepted 1 March 2024
Available online 3 March 2024
2238-7854/© 2024 The Authors. Published by Elsevier B.V. This is an open access article under the CC BY-NC-ND license (http://creativecommons.org/licenses/by-nc-nd/4.0/).

design approach is basically the method which has perennially been in use for the development of an extensive array of metallic materials, which include aluminium alloys, nickel alloys, stainless steels, steels, bronze alloys, titanium alloys, among others [3–6]. The fundamental basis for the development of alloys through this methodology relies on the prevention of complex microstructures and the formation of heterogeneously distributed intermetallic phases since they can lead to a decrease in mechanical performance [7–9]. Indeed, it is commonly noted that the development of intermetallic compounds and phases is more likely when there is an increase in the concentration of alloying elements [10–12]. This results in a novel recommended technique for designing metallic alloys based on the concept of multiple principal elements.

In recent years, there has been a notable surge in the attention given to high-entropy alloys (HEAs) owing to their emergence as a novel category of multicomponent alloys [13–15]. Initially, the term "High--entropy alloys" referred to materials that consisted of five or more primary elements, with each element having a concentration ranging from 5 at.% to 35 at.%, and these elements were present in equimolar or nearly equimolar ratios [14,15]. Currently, multicomponent alloys that possess configurational entropies that exceed a threshold of 1.5 R (where R represents the gas constant) are considered HEAs [15,16]. The two definitions indicate that the fundamental idea behind the design of HEAs is to maximize configurational entropy in order to promote the formation of solid solutions rather than intermetallic compounds [16, 17]. Due to the pronounced influence of high entropy, several HEAs can exhibit microstructures characterized by simple body-centred cubic (BCC) and/or face-centred cubic (FCC) solid solution phases [15–18] [19]. As a result, some HEAs have been discovered to possess notable characteristics, including enhanced strength, outstanding wear resistance, remarkable corrosion resistance, and outstanding performance under both high and cryogenic temperatures [13–17].

Consequently, these HEAs have garnered significant attention for their potential applications in various fields [13–17]. Nevertheless, it should be noted that not all HEAs have the capability to exhibit a homogeneous solid solution microstructure. In several instances, the occurrence of structured intermetallic phases, complex compounds, or even disordered phases in so-called HEAs has been reported [20–23]. Consequently, there has been interest in understanding better the rules governing phase development in HEAs, which is a trendy subject of ongoing scholarly discourse [24–27].

In recent times, there has been a growing focus on the investigation of multicomponent alloys that possess equal or non-equiatomic compositions with configuration entropy between 1R and 1.5R [28–31]. This new class of multicomponent alloys have been reported to possess superior mechanical properties compared to HEAs and most conventional alloys. This is linked to the formation of a continuous sequence of strengthening mechanisms, including a hierarchical twin network which serves to protract the strain hardening. For instance, several non-equiatomic multicomponent alloys have been documented in the literature. These include $Fe_{40}Mn_{27}Ni_{26}Co_5Cr_2$ and $Fe_{42}Mn_{20}Ni_{30}Co_6Cr_2$ quinary alloys as well as $Cr_4Mn_{28}Fe_{40}Ni_{28}$ and $Cr_{10}Mn_{40}Fe_{40}Co_{10}$ quaternary alloys, CoCrNi and FeCrNi ternary alloys [3,30–33]. The alloys exhibit configurational entropies ranging from 1 R to 1.5 R at a random state, indicating their classification as medium entropy alloys (MEAs) [30–32]. Despite the decrease in configurational entropies, these non-equiatomic multicomponent alloys exhibit exceptional microstructures and mechanical properties that may be compared to, or even surpass, those of HEAs [32,33].

Nevertheless, due to the intrinsic complex nature of the composition and the significant variation in melting temperatures among the constituent elements in these alloys, considerable elemental segregation and phase formation are expected to take place throughout the process of solidification and cooling [34,35]. In order to prevent this occurrence, it is typically necessary to employ fast cooling and subsequent solid-state hot-working techniques such as forging, extrusion, and rolling [34,35]. The utilization of hot working (deformation) is very advantageous in the domain of metal forming operations, as it plays a crucial role in reducing defects and transforming cast ingots into fully refined products in desired forms and configurations [35,36]. Therefore, it is imperative to possess a comprehensive understanding of the plastic flow behavior during hot deformation and the underlying deformation mechanisms. This knowledge is essential for determining the optimal processing conditions during hot deformation and enhancing the microstructural characteristics of products fabricated utilizing MEAs. The influence of various factors, including processing method, alloy composition, and deformation variables, on the hot deformation behavior of a MEA has been observed. Processing maps have been developed to predict this behavior based on constitutive equations such as the dynamic material model (DMM) [37,38] and strain rate sensitivity (SRS) [38,39]. The topic of interest for scientists engaged in hot deformation studies is the evaluation of the efficacy of using processing maps to forecast workability and identify instability regimes for MEAs [40,41].

The absence of a thorough literature evaluation on the hot deformation behavior of MEAs has motivated the selection of this particular area of research for the present review. Currently, the most related reviews that are available in the literature cover different aspects of hot deformation studies on HEAs [41,42]. Given the apparent lack of existing literature on state-of-the-art reviews pertaining to the hot deformation behavior of MEAs, the present review endeavour was initiated. The following sections will begin by giving an overview of the significance of hot working in improving the mechanical properties of MEAs. Subsequently, a thorough investigation is carried out on the hot-deformation characteristics of MEAs, focusing on the softening mechanisms that occur at elevated temperatures, changes in microstructure, the use of processing maps to predict both safe and unsafe processing conditions, the analysis of constitutive equations, machine learning algorithm and molecular dynamics model for the calculation of predicted flow stress during hot deformation and the prevailing deformation mechanisms. This review also presents the future research directions in this area that would contribute to a more sustainable implementation of hot deformation in MEAs.

2. Influence of hot working process on the mechanical properties of MEAs

This section examines the impact of hot deformation on the mechanical characteristics of MEAs. MEAs have attracted growing interest owing to their remarkable mechanical characteristics, including but not limited to high mechanical strength, good ductility, and exceptional corrosion resistance. Hot deformation aids grain refinement and reduces defects, which contribute to the alloy's strengthening. Extensive research has examined the influence of hot deformation on the mechanical characteristics of MEAs, demonstrating that it can enhance the alloy's tensile strength, yield strength, ductility, and other mechanical properties [43,44]. Therefore, this study will review recent studies conducted on the hot deformation of these MEAs: $Ti_{65}(AlCrNb)_{35}$ [44], FeCoNiAlTiMo [45], CrCoNi [43], $Ni_2Co_1Fe_1V_{0.5}Mo_{0.2}$ [46], TiAlCrNbV [47]and determine their enhancement in the mechanical properties of the alloy.

$Ti_{65}(AlCrNb)_{35}$ MEA was investigated by Liao et al. [44] after the lightweight alloy had undergone a sequence of thermomechanical treatment (TMT) that includes homogenization, hot-rolling, cold rolling and annealing. Five samples were produced; the first was the homogenized cast samples, then the hot rolled 50% cold rolled 70% (HR50CR70) samples, and then three annealed HR50CR70 samples at 900 °C for 10 min (at 1.5 °C/s), 1000 °C for 3 min (at 5 °C/s) and 1100 °C for 1 min (at 15 °C/s). The HR50CR70 material displayed characteristic behavior commonly observed in highly deformed metallic materials, including limited strain hardening and abrupt necking. The tensile yield strength (TYS) 1475 MPa, ultimate tensile strength (UTS) of 1620 MPa and a uniform elongation (UE) of 7%, as seen in the

stress-strain curve in Fig. 1. The samples that underwent annealing at 900 °C achieved a recrystallization rate of 20% (see Fig. 2) exhibited a TYS of 1210 MPa, UTS of 1380 MPa, and UE of 9%. On the other hand, the annealed samples at 1000 °C underwent 50% recrystallization (see Fig. 2), had TYS of 1070 MPa, UTS of 1370 MPa, and a significantly higher UE of 24%. The annealed samples at 1100 °C that underwent annealing and achieved 95% recrystallization (see Fig. 2) exhibited a TYS of 1005 MPa, UTS of 1320 MPa, and a notable UE of 30%. The higher work hardening rate observed in the 95% partially recrystallized samples led to the aforementioned improvement in the strength-ductility balance and is attributable to the microstructural heterogeneity that is widely reported in materials with heterogeneous structures. Additionally, as the annealing time increased, the mechanical properties were improved as a result of the gradual replacement of the deformed structures with recrystallized structures. The mechanical characteristics of the TMT samples were superior to those of the homogenized cast samples. The TYS of the homogenized cast sample was 910 MPa, while the UTS was determined to be 1100 MPa, with UE of1 31%. The improvement in the mechanical properties was attributed to the heterostructure made up of smaller recrystallized grains and deformed bands.

$Ti_{65}(AlCrNbV)_{35-x}Zr_x$ (x = 3, 5, 7, and 10) MEA. The alloy was rolled under two different conditions; the first was cold rolled with 70% deformation strain (CR70), and the second was hot rolled initially to a strain of 50%, then cold rolled to a deformation strain of 70% (HR50CR70). The researchers also evaluated its properties under different annealing periods, which were 30, 40, 50, and 60 s. The as-cast MEAs demonstrated an upward trend in mechanical characteristics, specifically in terms of yield strength and ductility, when the Zr weight fraction was raised from 3 to 10 at a range of roughly 3–8%. The optimal balance of yield strength and ductility was seen in the as-cast Zr7 alloy, with values of 1015 MPa and 22.2%, respectively. The combined effect of the increased grain size and influence of solid solution strengthening achieved by the increased Zn weight fraction led to the excellent strength–ductility synergy observed. This optimum as-cast MEA was selected for two additional rolling processes and also annealed. The as-rolled samples exhibited a yield strength of approximately 1530 MPa, which remained consistent when subjected to a plastic strain ranging from roughly 5.0 to 7.5%. When the annealing was carried out at different times, an increase in the annealing time from 30 to 60 s caused the yield strength to reduce from approximately 1330–1100 MPa.

In contrast, the ductility of the sample exhibited a substantial rise to around 20%. A comparative analysis of the samples subjected to CR70 and HR50CR70 processing demonstrated that, in both the as-rolled and annealed states, the HR50CR70 samples consistently exhibited superior ductility compared to the CR70 samples. This can be linked to the effective elimination of defects and the refinement of grain sizes achieved through dynamic recrystallization (DRX) during the hot-rolling process subsequent to casting. In the context of various processing routes applied to Zr7 MEA samples, it was observed that the samples subjected to HR50CR70 processing and annealed for a duration of 30–50 s displayed favorable mechanical properties, specifically a yield strength exceeding 1200 MPa and a ductility surpassing 15%. The improved strength-ductility synergy was a result of the higher annealing temperature, which allowed for the HR50CR70 MEA to complete its recrystallization earlier, followed by rapid coarsening of the recrystallized grains. Also, the more significant accumulation of strain energy provided more driving force for enhancing the nucleation and grain growth rate of recrystallization. Notably, this resulted in excellent yield strength of 1350 MPa and ductility of 15.3% exhibited in the Zr7 MEA sample treated with HR50CR70 processing and annealed for 30 s. Moreover, the HR50CR70 Zr7 MEAs exhibited a specific yield strength of 264 MPa·g/cm3 and a ductility of 15.3%, surpassing that of conventional Ti alloys as well as other lightweight HEAs and MEAs.

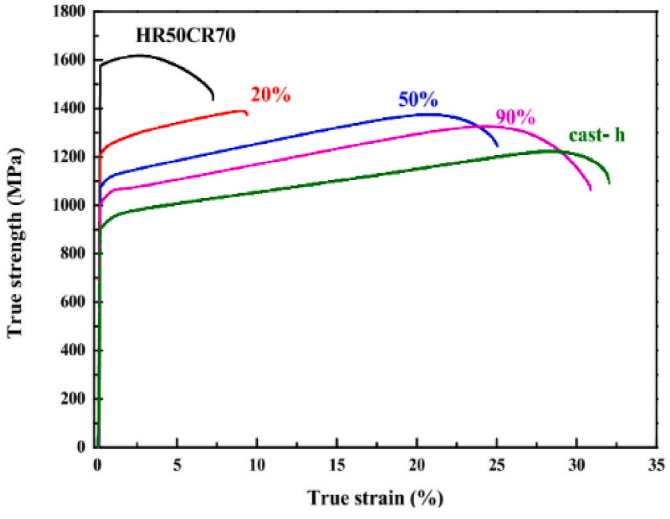

Fig. 1. The tensile stress-strain curves of HR50CR70 and annealed HR50CR70 Ti-65 alloys [44]. Culled with permission from Elsevier.

It can be, therefore, established from Liao et al. [44] and Chen et al. [47] study that the influence of annealing parameters (time, heating rate, and annealing temperatures) after hot working plays a critical role in enhancing the mechanical strength characteristics of MEAs.

There is a significant demand for metallic materials that exhibit exceptional tensile qualities at cryogenic temperatures in various sophisticated cryogenic applications. These applications include fusion magnets used in fusion reactors, storage tanks, transportation pipelines for liquefied nitrogen gas, cryogenic rocket engines, and others [43,45]. Kwon et al. [45] studied the influence of hot-rolling on the mechanical properties of a non-equiatomic $Fe_{50}Co_{25}Ni_{10}Al_5Ti_5Mo_5$ (at. %) ferrous MEA at room and cryogenic temperatures. The MEA samples were hot-rolled at 1150 °C to a thickness of 1.5 mm via multiple passes without further treatment. The HR samples were subjected to tensile test at temperatures of 298 K (25 °C) and 77 K (−196 °C), as well as a strain rate of 10^{-3} s^{-1}. The HR sample at 298 K revealed an outstanding ultimate tensile strength (UTS) of ~1.5 GPa, yield strength (YS) of 570 MPa and uniform elongation (UE) of ~15%.

On the other hand, at 77 K, a higher UTS of ~2.3 GPa and YS of ~1.3 GPa with a decent UE of ~11% were recorded. It was reported that when the current MEA was compared with other high-strength MEAs, as seen in Fig. 3, the current MEA had superior tensile properties. This was as a result of the improved solid solution strengthening (attributed to the addition of aluminum, titanium and molybdenum exhibiting larger atomic radii than the iron-cobalt-nickel of the bulk composition), precipitation strengthening effect (governed by the Orowan mechanism via pinning dislocation motion), dislocation strengthening effect (attributed to the hot rolling process and the thermally induced martensite transformation involving diffusionless shear deformation), boundary strengthening effect (attributed to the fine grain size of ~4.5 μm) and immense strain hardening during plastic deformation that is mainly attributed to the body centred cubic-deformation induced martensite transformation (BCC-DIMT), which is notably amplified in the present MEA, at both temperatures.

The influence of hot-isostatic pressing (HIP) on the cryogenic mechanical characteristics of direct energy deposition (DED)-fabricated CrCoNi MEAs was examined by Tran et al. [43]. The as-built and HIP-treated CrCoNi MEA-DED samples' mechanical strength characteristics were evaluated when uniaxial tensile tests were done at room (298 K or 25 °C) and cryogenic (77 K or −196 °C) temperatures. The results revealed that at 298 K, the CrCoNi MEA-DED after hot-isostatic pressing exhibited a reduction in yield strength and tensile strength (300 MPa and 773 MPa, respectively) compared to that of the as-built CrCoNi MEA-DED (557 MPa and 841 MPa). However, they exhibited similar elongation to that of the as-built CrCoNi MEA-DED (66%). At 77 K, the

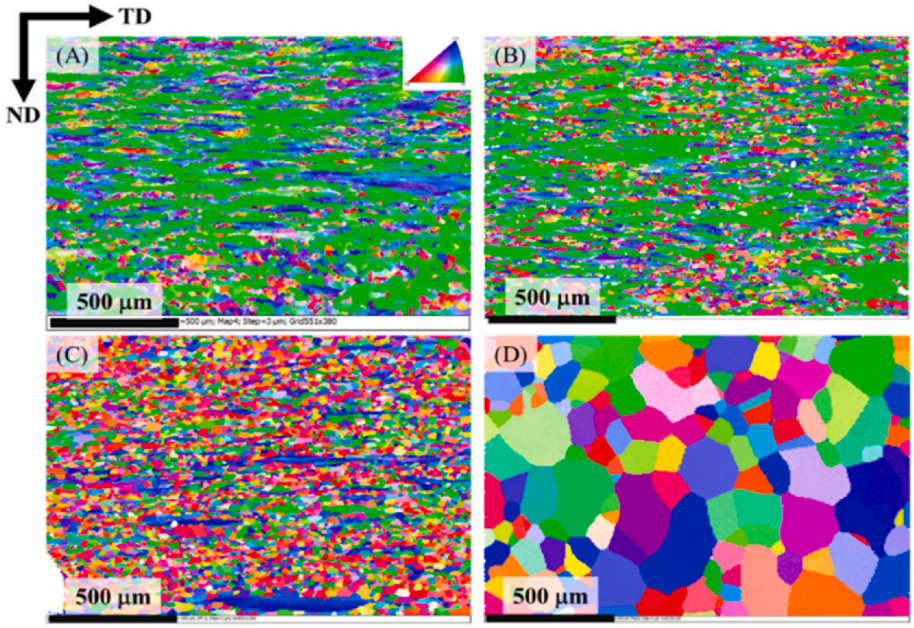

Fig. 2. The EBSD map of CR70 Ti-65 alloy after annealed for recrystallization of (a) 20%, (b) 50%, (c) 95%, and (d) homogenized Ti-65 alloys [44]. Culled with permission from Elsevier.

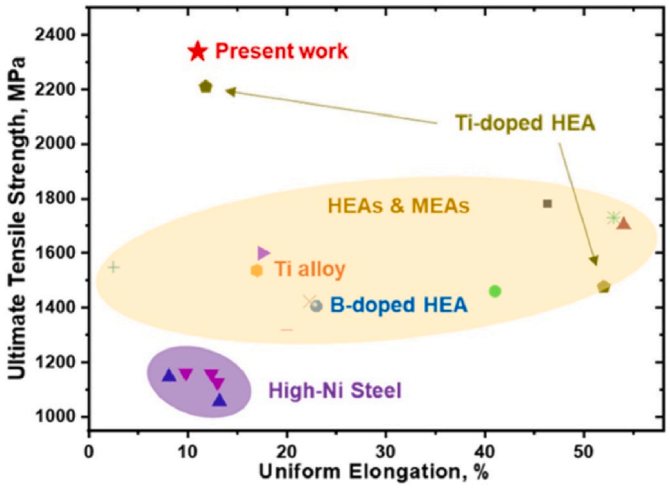

Fig. 3. Ultimate tensile strength versus uniform elongation of the current MEA and other HEAs/MEAs [45]. Culled with permission from Elsevier.

as-built CrCoNi MEA-DED showed typical trade-off tensile characteristics of increased yield and tensile strength (787 MPa and 1237 MPa, respectively) and decreased elongation to fracture (33%). At the same time, the HIP-treated CrCoNi MEA-DED was reported to show an excellent combination of high strength (557 MPa yield strength and 1147 MPa tensile strength) and preserved elongation (71%) at 77 K. It led to a notable increment in the strain energy density, exhibiting a 56% rise when compared to the conditions at ambient temperature. The observed phenomenon can be attributed to a substantial reduction in micropores following the hot isostatic pressing (HIP) process. In addition, the CrCoNi MEA-DED that underwent HIP treatment exhibited deformation twinning at lower strains, resulting in a consistent increase in work hardening behavior, and this delayed the occurrence of necking instability.

Furthermore, a comprehensive comparison was conducted on the mechanical strength characteristics of the CrCoNi MEA-DED with other CrCoNi MEAs produced through various processing methods, including casting-based and spark plasma sintering processes. The results highlighted the outstanding mechanical strength of CrCoNi MEA-DED treated with HIP at cryogenic temperatures, demonstrating the viability of using Directed Energy Deposition (DED) for fabricating CrCoNi MEAs. Grain boundary strengthening had minimal impact on the yield strength of CrCoNi MEA-DED. The primary contributor to yield strength was dislocation strengthening, especially prominent in the as-built structure compared to the HIP-treated CrCoNi MEA-DED. The decrease in strength in the HIP-treated MEA was attributed to the reduction in initial dislocation density, confirmed by the gradual decrease in dislocation density after HIP treatment. The exceptional elongation to fracture in the CrCoNi MEA-DED with HIP, compared to the as-built MEA-DED, was attributed to the combined effects of dislocation density reduction and deformation twinning. Calculations indicated that the twinning stress was lower than the maximum flow stress, suggesting ready activation of deformation twinning and contributing to improved elongation.

Kwon et al. [45] and Trans et al. [43] studies established that the processing of the MEA at cryogenic temperature had a very significant impact on their strength-ductility ratio. It is noted from these studies that processing MEAs at cryogenic temperatures helps to improve their strength without compromising the ductility. In addition, carrying out HIP treatment on the MEA showed the unique combination of very high strength and the preservation of a relatively good ductility at cryogenic temperatures as a result of the notable reduction of micropores coupled with the presence of thermally induced martensite (TIM) structures and the earlier activation of deformation twinning.

In a recent investigation conducted by Jiang et al. [46] on the creep properties of $Ni_2Co_1Fe_1V_{0.5}Mo_{0.2}$ MEA when subjected to tensile creep tests in the temperature range of 973–1073 K (700–800 °C) under initially applied stresses of 150–200 MPa for 168 h. From the result, samples tested at 1073 K/150 MPa, 1023 K/150 MPa, and 973 K/200 MPa fractured after 5.55, 54, and 128 h respectively. However, samples tested at 973 K/175 MPa and 973 K/150 MPa did not experience fracture throughout the 168-h test period (see Fig. 4a). This was attributed to the dominance of viscous dislocation glide mechanism in creep deformation and the absence of critical stress and strain levels. Furthermore, this MEA was evaluated against other HEAs/MEAs regarding its creep properties, as seen in Fig. 4b. It was revealed that the

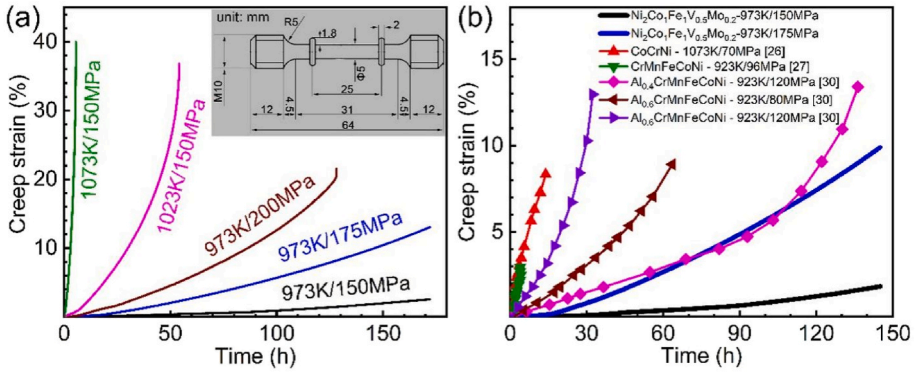

Fig. 4. (a) (b) Comparison for tensile creep properties of some MEAs and HEAs with the current MEA [46]. Culled with permission from Elsevier.

current $Ni_2Co_1Fe_1V_{0.5}Mo_{0.2}$ MEA exhibited superior creep properties at higher temperature and stress when compared to that of CrMnFeCoNi HEA and CoCrNi MEA. This phenomenon was ascribed to the elevated activation energy associated with the $Ni_2Co_1Fe_1V_{0.5}Mo_{0.2}$ MEA, with Mo and V possessing notably high activation energies for atomic diffusion. The formation of a solid solution involving Vanadium (V) and Molybdenum (Mo) was deemed advantageous for enhancing creep properties by restricting diffusion rates through their high activation energy. Thus, the inclusion of Mo and V in the $Ni_2Co_1Fe_1V_{0.5}Mo_{0.2}$ MEA was attributed to their substantial activation energy (456.3 kJ mol^{-1}) for creep deformation, which closely match that of the CrFeCoNiMo0.2 HEA (463 kJ mol^{-1}), stainless steel (460 kJ mol^{-1}), and nickel-based superalloys (443 kJ mol^{-1}).

In summary, MEAs subjected to hot deformation are studied to enhance their mechanical properties, with the primary goal being the preservation of their strength-ductility balance. The hot deformation significantly enhances the strength-ductility balance of the MEAs. It was established that recrystallized grains, twins present in the microstructure of the MEAs during hot deformation, significantly aided in enhancing the mechanical strength properties. The pinning effect on the motion of the dislocations led to precipitation strengthening, the presence of thermally induced martensite transformation involving diffusionless shear deformation and body-centred cubic-deformation induced martensite transformation (BCC-DIMT) also led to the enhanced mechanical strength observed in the MEAs. Furthermore, solid solution strengthening of certain elements of the MEA during hot deformation improved the mechanical properties. In addition to improving the alloy's properties, annealing parameters (i.e. the heating rate, annealing time and temperature) also played a significant role. Hence, it is imperative to optimize the annealing and the thermomechanical treatment parameters to enhance the mechanical properties. Due to these reasons, the thermomechanical treatment of MEA alloys, such as hot rolling, hot isostatic pressing, and creep deformation, enhances both their strength and ductility. Any combination of these techniques could result in a significant improvement in the mechanical properties of MEAs.

3. Microstructural evolution and phase transformations

The impact of microstructural evolution on MEA properties cannot be overstated. Microstructural evolution studies present to us the changes that occurred in the alloys during hot deformation processes. Microstructural changes ranging from grain refinement and precipitate redistribution, among others, show a significant impact on the MEAs' mechanical strength, ductility and toughness. Nonetheless, the microstructural evolution of MEAs is a multifaceted process that is yet to be fully comprehended. Nevertheless, a grasp of the factors that influence microstructural evolution can facilitate microstructure control and property customization of MEAs for specific applications. Several researchers have studied the microstructural evolution that occurs when MEAs are subjected to different hot deformation processes. These studies highlight the complex and temperature-dependent nature of microstructural evolutions in MEA and the importance of understanding these phenomena for tailoring MEA properties to specific applications. The potential for recrystallization and the influence of strain rate on grain size are key factors to consider in the design and processing of MEAs.

He et al. [48] investigated the extent of grain refinement during hot deformation of an equiatomic CrCoNi alloy. They found that higher deformation temperatures led to more uniform grains, indicating facilitated recrystallization at elevated temperatures. Grain size increased with higher strain rates, but the relationship between strain rate and grain size could have been more straightforward and depended on the specific temperature. The study presented that the samples were subjected to thermal compression, from 900 to 1100 °C deformation temperatures and varying strain rates of 0.01 and 1 s^{-1}. The initial microstructure prior to hot deformation exhibited homogenous grains with an average size of approximately 20 ± 0.8 μm for the alloy. Upon deformation at elevated temperatures, the grains in the CrCoNi alloys were observed to be more uniform than their counterparts, as evidenced by the post-deformation microstructure as seen in Fig. 5. At a deformation temperature of 900 °C and a strain rate of 0.01 s^{-1}, a typical necklace structure was detected which is attributed to DDRX (discontinuous dynamic recrystallization); however, with a rise in temperature, this structure gradually faded away, giving way to more equiaxed grains. These observations suggest that the recrystallization of the CrCoNr alloy is facilitated at higher temperatures, with the effect being more pronounced at 1100 °C.

Furthermore, it was observed that the grain size increased with an increase in strain rate (0.01–1 s^{-1}) upon deformation at higher temperatures (1100 °C) than that of 900–1000 °C. This is because the grain growth of recrystallized grains is accelerated as the temperature rises. In contrast, the effects of strain rate on grain size are not straightforward but ambiguous because at a specific temperature of 900 °C, decreasing the strain rate refines the average grain size, which means that slower deformation leads to smaller grain sizes. Then, at 1000 °C, a slight reduction in the grain size was observed from 0.01 to 1 s^{-1} strain rate, indicating that faster deformation does not necessarily lead to larger grain sizes. There was a decrease in the grain size as the temperature increased to 1100 °C and the strain rate increased from 0.01 to 0.1 s^{-1}, which means that slower deformation leads to smaller grain sizes. However, an increase was observed when the strain rate further increased to 1 s^{-1}, which means that faster deformation can lead to larger grain sizes. This indicates that the interactions between dislocates are dominant in grain evolution. These results suggest that the effects of strain rate on grain evolution are dependent on the specific temperature and can be ambiguous.

Also, Tran et al. [43] investigated the effect of hot isostatic pressing (HIP) on the microstructural feature of a direct energy deposition

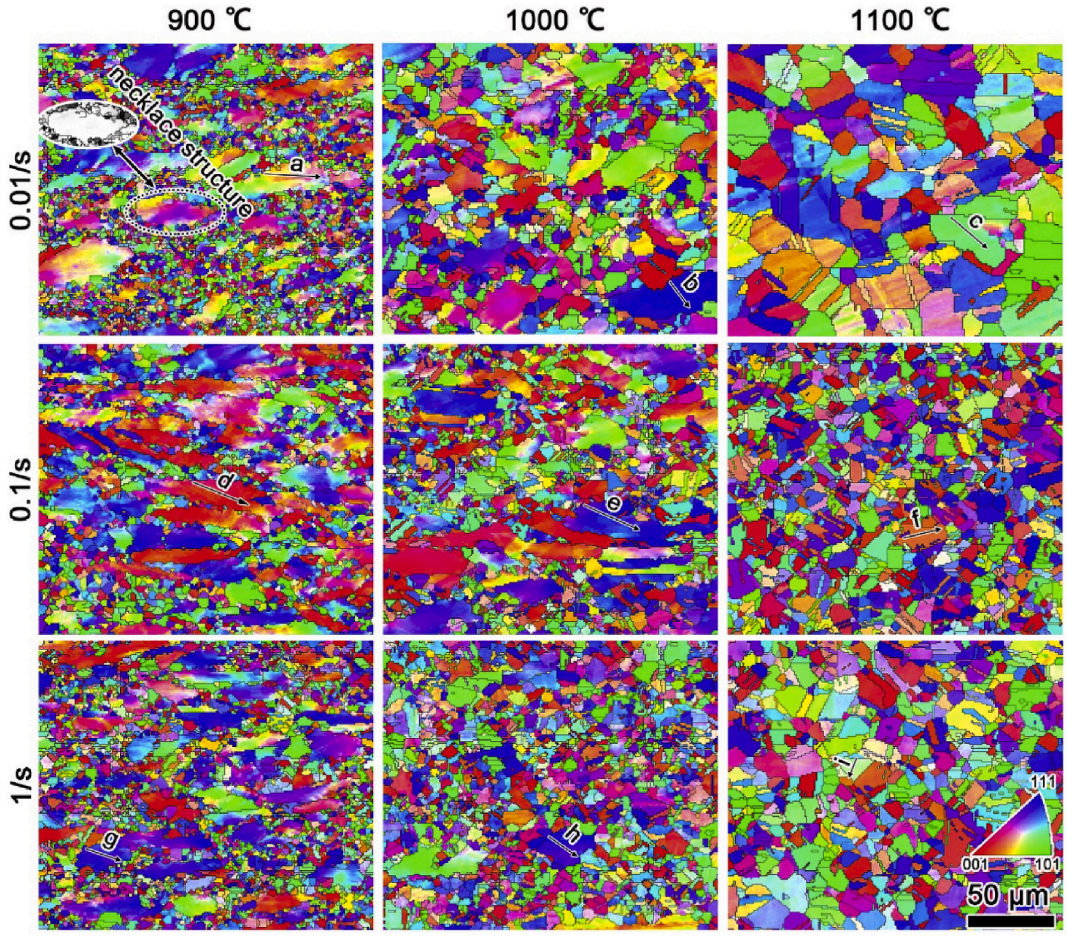

Fig. 5. EBSD IPF images of specimens deformed at different conditions [48]. Culled with permission from Elsevier.

processed (DED) CrCoNi MEA at room temperature and cryogenic temperature. In this particular investigation, MEA powders were utilized for additive manufacturing through the utilization of the DED process. Once the DED process was executed, the as-built specimens were then subjected to HIP at a temperature of 1150 °C and a pressure of 1000psi. The research revealed the stability of a single FCC phase after HIP treatment. HIP-treated specimens exhibited equiaxed grain morphology and a significant degree of recrystallization, which was not present in the as-built samples. Uniaxial tensile tests were conducted on both the as-built and HIP-treated CrCoNi MEA-DED specimens. The tests were performed at an engineering strain rate of 10^{-3} s^{-1} and were conducted at both room temperature (298 K or 25 °C) and cryogenic temperature (77 K or −196 °C). The phase configuration analysis indicated that the CrCoNi MEA-DED material consists exclusively of a single face-centred cubic (FCC) phase without any observable phase transformation subsequent to HIP treatment. This reinforces the stability of the FCC's single-phase post-HIP processing. The microstructure of both the as-built and HIP-treated CrCoNi MEA-DED specimens was scrutinized prior to and subsequent to the uniaxial test. The as-built sample displayed an uneven, predominantly columnar grain structure with low-angle grain boundaries (LAGBs) that were surrounded by high-angle grain boundaries (HAGBs). Conversely, the HIP-treated CrCoNi MEA-DED unveiled an equiaxed grain morphology and a noteworthy degree of recrystallization with intragranular orientation spread. The microstructure of the deformed specimen can be seen in Fig. 6.

In a similar study, Guan et al. [49] carried out hot compression tests on CrCoNi MEA from 700 °C to 1000 °C and at strain rates ranging from 0.001 to 1 s^{-1}. The result showed that high temperature and low strain rate conditions led to higher fractions of recrystallized grains with a necklace structure, primarily attributed to DDRX. To clarify, the observations of the microstructure revealed that the as-cast MEA is characterized by a coarse grain with an average grain size of 200 ± 50 μm and an FCC phase structure. At a deformation condition of 700 °C/0.001 s^{-1}, the grain boundaries were found to be significantly more prolonged and predominantly straight. However, the increased strain rate resulted in shorter grain boundaries and the emergence of numerous fine grains in the vicinity of the grain boundaries. A decrease in the strain rate from 1 s^{-1} to 0.01 s^{-1} or 0.001 s^{-1} at a temperature of 900 °C led to an increase in the number of fine grains and wider shear bands.

Similarly, when CrCoNi MEA was deformed at 1 s^{-1} at a temperature of 1000 °C, densely distributed deformed microstructures were observed, and as the strain rate decreased to 0.1 s^{-1}, a serrated grain boundary was observed in the coarse grains, alongside fine grains. However, an increase in recrystallized grains was noted, and this increased further as the strain rate decreased to 0.01 and 0.001 s^{-1} at 1000 °C. Thus, it is clear that higher fractions of recrystallized grains, exhibiting a necklace structure, are observed at high temperatures (900–1000 °C) and lower strain rates, with these changes in microstructure being attributed to DDRX and also with the occurrence of continuous dynamic recrystallization (CDRX) due to the recrystallized grains as in Fig. 7. It was also observed in samples deformed at 700 °C with a strain rate of 1 s^{-1}, due to the recrystallized grains seen along the grain boundaries.

Also, Liu et al. [50] studied the microstructural changes that occurred during the hot compression of polycrystalline CrCoNi at temperatures ranging from 900 to 1100 °C and a strain rate of 0.01 s^{-1}. They found that the degree of recrystallization and grain morphology varied with different heat treatment conditions, strain rates and annealing

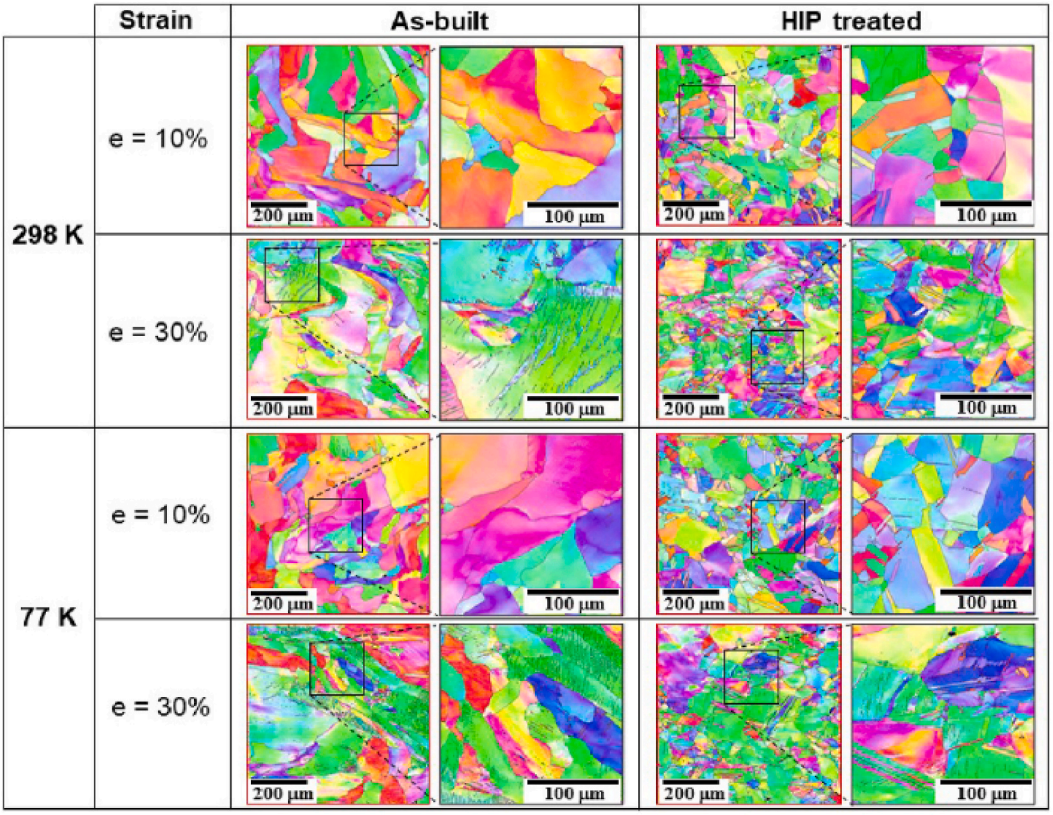

Fig. 6. The IPF map of deformed microstructures of as-built and HIP treated CrCoNi MEA-DED at different engineering strains at room (298 K or 25 °C) and cryogenic (77 K or −196 °C) temperatures [43]. Culled with permission from Elsevier.

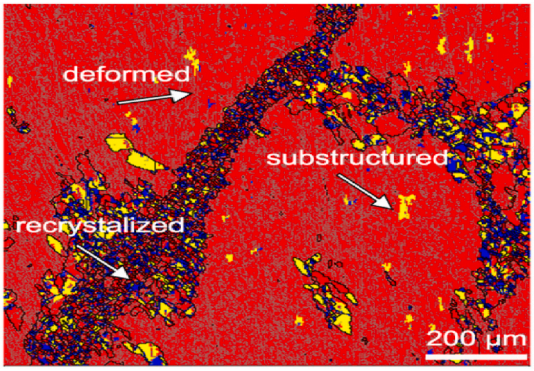

Fig. 7. (a) IAMA map showing the distribution of substructured grains (yellow), deformed grains (red) and recrystallized grains (blue) [49]. Culled with permission from Elsevier. (For interpretation of the references to color in this figure legend, the reader is referred to the Web version of this article.)

temperatures. Among their test samples, the ones compressed at a temperature of 1000 °C were selected for further annealing heat treatment, specifically at 650 and 750 °C for 0.5 and 1 h, respectively, in order to attain a structural composition of varying degrees of recrystallization. The analysis of microstructure revealed the presence of elongated grains in the samples that were subjected to hot compression at 1000 °C with a strain rate of 0.01–1 s^{-1}, followed by annealing at 650 °C/0.5–1 h and at 750 °C/0.5 h. On the other hand, samples compressed at a lower strain rate of 0.01 s^{-1} under all heat treatment conditions had a higher degree of equiaxed grains compared to samples compressed at higher strain rates of 0.1 s^{-1} and 1 s^{-1}.

Additionally, specimens annealed at a higher temperature of 750 °C/1 h also achieved a higher degree of equiaxed grains. However, for samples compressed at strain rates of 0.1 s^{-1} and 1 s^{-1}, those specimens annealed at 750 °C had more equiaxed grains than those annealed at 650 °C. However, the samples subjected to annealing at a temperature of 750/1 h and a strain rate of 1 s^{-1} displayed indications of grain coarsening after recrystallization. The number of equiaxed grains increased with the duration of annealing in the specimens annealed at the same temperature. It was observed that the discontinuous recrystallization with distinct nucleation occurred at the grain, and the newly formed crystallized grains were smaller in size than the other grains, such as subgrains and deformed grains. This finding suggested the presence of static discontinuous recrystallization under all conditions.

Furthermore, the specimens formed at 0.01 s^{-1} showed a higher degree of recrystallization, particularly under the annealing condition of 750 °C/1 h, where the recrystallization process was almost completed. Even though the majority of low-angle grain boundaries still existed in these large subgrains for samples deformed at 1000/0.1 s^{-1} and annealed at 759/0.5 h and samples deformed at 1000/1 s^{-1} and annealed at 650/0.5 h, the recrystallization degree generally increased with increased annealing temperature and annealing time. As a general trend, the recrystallization fraction increased as the strain rate decreased.

The microstructure of the deformed samples at various deformation conditions can be seen in Fig. 8.

Hot deformation and workability of a CrCoNi MEA were studied by Wang et al. [51]. The result indicated the presence of recrystallized grains at higher temperatures and the appearance of twins as the temperature increased. In their investigation, hot compression was performed at deformation conditions of 0.01–10 s^{-1}/800–1100 °C. The microstructural analysis that followed deformation disclosed that at a strain rate of 0.1 s^{-1} at 800 °C, the primary grains underwent perpendicular elongation along the compression axis, signifying the lack of recrystallization post-deformation. Upon elevating the deformation

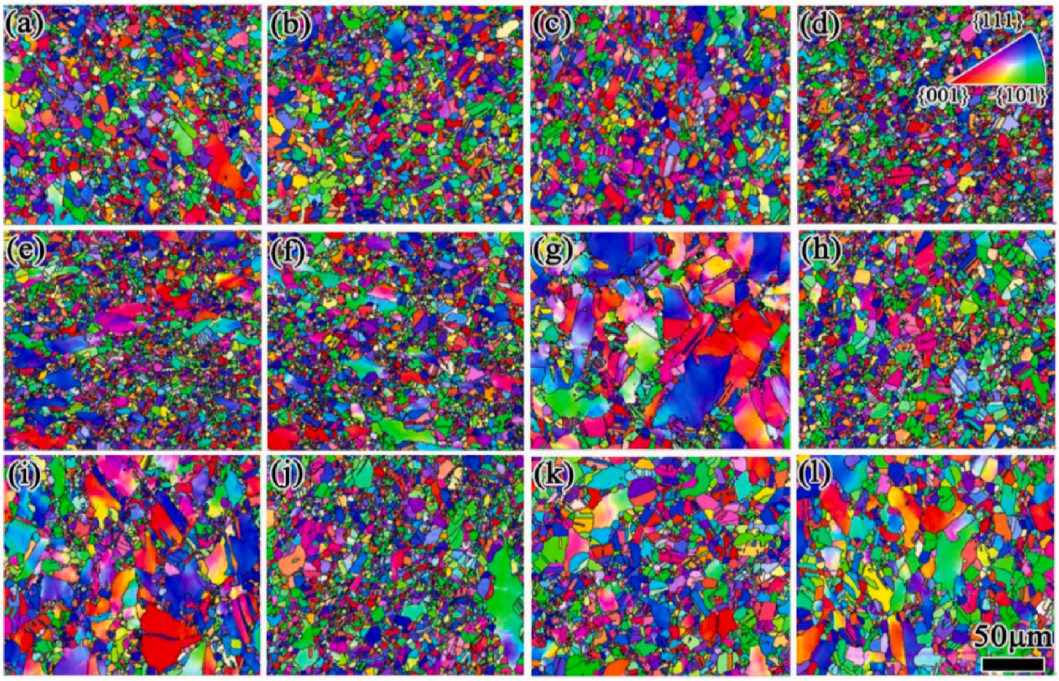

Fig. 8. The inverse pole figure maps of specimens compressed at different parameters. From the first column to the fourth column, specimens were annealed under 650 °C for 0.5 h, 650 °C for 1 h, and 750 °C for 0.5 h, 750 °C for 1 h. From the first row to the third row, specimens were compressed at 1000 °C–0.01/s, 1000 °C–0.1/s and 1000 °C-1/s respectively [50]. Culled with permission from Elsevier.

temperature to 900 °C, a few recrystallized grains were observed near the grain boundaries. Subsequently, with a further surge in temperature, the recrystallized grains exhibited growth. Specifically, in comparison to the temperature of 1000 °C, the recrystallized grains demonstrated further growth after the temperature was increased to 1100 °C, which was accompanied by the appearance of a few twins.

Yi et al. [52] studied the hot working characteristics of CoCrNi and $(CoCrNi)_{94}Ti_3Al_3$ MEAs. In this study, Ti and Al were added to CoCrNi MEA alloy to produce $(CoCrNi)_{94}Ti_3Al_3$, and both samples were compared. The presence of a necklace structure was observed in CoCrNi at relatively low temperatures and high strain rates. $(CoCrNi)_{94}Ti_3Al_3$ alloy displayed different behavior, with fully equiaxed grains and homogenous grain morphologies at higher temperatures and lower strain rates. In their study, the CoCrNi & $(CoCrNi)_{94}Ti_3Al_3$ samples were compressed at deformation conditions of 850–1100 °C/0.001–1 s^{-1}. In the exploration of CoCrNi alloy, it was observed that samples subjected to hot compression at relatively low temperatures and high strain rates exhibited a necklace structure formed by both fine and coarse grains for both MEA alloys. Although CoCrNi samples that underwent deformation at 850 °C/0.001–0.01 s^{-1}, 900–950 °C/0.01–1 s^{-1}, and 1000 °C/0.1–1 s^{-1} displayed an elevated quantity of the necklace structure compared to that of $(CoCrNi)_{94}Ti_3Al_3$ alloy, indicating a more significant occurrence of DDRX under these circumstances. The fine grains, encompassed by high-angle grain boundaries (HAGBs), were identified as the DDRXed grains, while the coarse grains contained a high density of sub-grain boundaries and low-angle grain boundaries (LAGBs). A more significant proportion of LAGBs were noted when the MEA underwent hot compression at a high strain rate and/or low temperature. Then, as the temperature increases and strain rate reduces for samples deformed at 950 °C/0.001 s^{-1} and 1000 °C/0.001–0.01 s^{-1}, the density of LAGBs reduces, exhibiting equiaxed grains, thereby indicating the formation of a completely recrystallized structure.

In the case of $(CoCrNi)_{94}Ti_3Al_3$ MEA, the necklace structure was also detected at 900–1000 °C/0.01–0.1 s^{-1}, but as the temperature increased to 1100 °C, it was no longer observed after hot deformation—the LAGBs in their plastic-deformed coarse grains and no aggregation distribution within their grain interior. A notable reduction in the quantity of LAGBs was seen as the temperature rose from 900 to 1000 °C for all strain rates. In addition, it was observed that with a strain rate of 0.001 s^{-1}, the grains exhibited a fully equiaxed structure and underwent complete recrystallization, leading to the development of relatively homogeneous grain morphologies.

Typically, achieving fully recrystallized grain structures through hot working necessitates relatively high temperatures and lower strain rates. At higher temperatures and lower strain rates, discontinuous dynamic recrystallization serves as a crucial mechanism for grain refinement, resulting in the development of a uniform grain structure. Also, the effect of strain rate on the grain size may not be direct as the diffusion pathways during hot working of MEAs are not straightforward. It is noted from some of the studies reviewed that the influence of strain rate on grain refinement is not consistent. Also, the deformation heating effect at strain rate >0.01 s^{-1} can influence the anomalous behavior of the microstructures. Hence, further studies should be conducted to understand these anomalies fully. Furthermore, it is observed that CoCrNi MEA is the most considered alloy in this section of this review, and very little information on other MEAs can be retrieved from the literature. Hence, microstructural evolution during hot deformation of other MEAs should be carried out. Also, some of the experiments are not fully isothermal. Therefore, further research should also be carried out under this condition.

4. Hot deformation behavior of MEAs

MEAs have demonstrated distinctive microstructures and favorable characteristics [53–57]. MEAs such as CrCoNi produced through direct energy deposition (DED) exhibit high ultimate tensile strength (UTS) of 874 MPa, yield strength of 621 MPa, and elongation to fracture of 45% [58]. Jiang et al. [46] also discovered that $Ni_2Co_1Fe_1V_{0.5}Mo_{0.2}$ MEA possessed excellent creep properties under the stresses of 150–200 MPa and within the temperature range of 973–1073 K (700–800 °C).

However, the hot deformation characteristics of different MEAs have been investigated by numerous researchers in the past five years. This is

to further discover and improve the reliability of MEAs by understanding their deformation mechanisms under increased temperatures. However, there has been little to no review of this literature on MEAs. Therefore, this study will systematically review the plethora of recent studies conducted on the hot deformation of MEAs and determine their optimum deformation parameters and mechanisms.

4.1. Effect of deformation temperature, strain, and strain rate on MEAs

Understanding the correlation between the hot working parameters (such as temperature, strain rate, and strain) and the flow behavior of MEAs is projected to be one of the best approaches toward the optimization of the hot deformation process [53]. In this section, the effect of temperature, strain, and strain rate on the flow behavior of MEAs is evaluated. Several authors, including Qiao and Zhu [53], He et al. [48], Liua et al. [59], Guan et al. [49], Yi et al. [52], Wang et al. [51], Tran et al. [43] have recently studied the hot deformation behavior of MEAs in order to understand the mechanisms of deformation and expand their practical applications. Qiao and Zhu [53] investigated the flow behavior of Al–Cr–Fe–Ni MEAs at working temperatures of 800–1100 $^{\circ}C$ and 0.001 to 1 s^{-1} strain rates. The flow curves presented in Fig. 9 showed that, as strain increases, flow stress starts to drop after reaching a peak stress value due to the effect of DRX. The flow behavior of the alloy exhibits a trend of rapid increase in flow stress during the initial stages of deformation. It reaches a maximum value before gradually decreasing with growing strain. The impact of temperature and strain rate on the plastic flow characteristics of AlCrFeNi MEA is clearly depicted in Fig. 10. It is noted that the flow stress diminishes as the temperature rises. These stress-strain curves demonstrate initial work hardening,

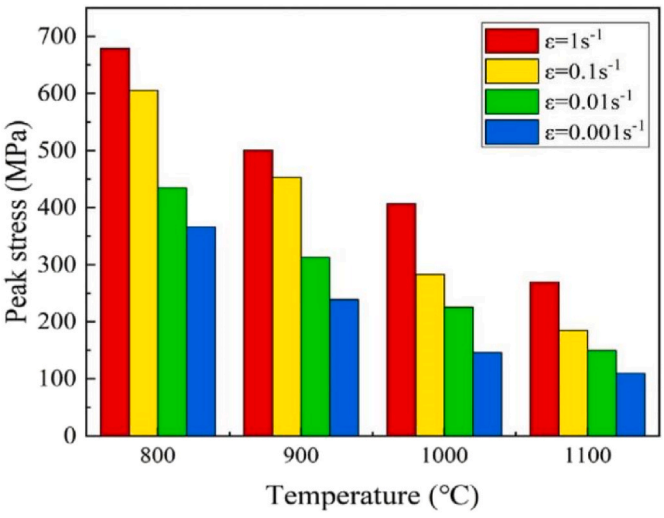

Fig. 10. Effects of deformation temperature and strain rate on the peak stress of AlCrFeNi MEA [53]. Culled with permission from Elsevier.

marked by the multiplication of dislocations and the creation of sub-grain boundaries, resulting in an elevation of flow stress. Subsequently, after reaching the peak stress, the curves indicate dynamic softening as deformation advances at elevated temperatures and substantial strain, facilitated by the grain boundary mobility mechanism. It is noted that some of the flow curves attained steady-state stress after the peak stress, which has been classically linked to DRV. However, the

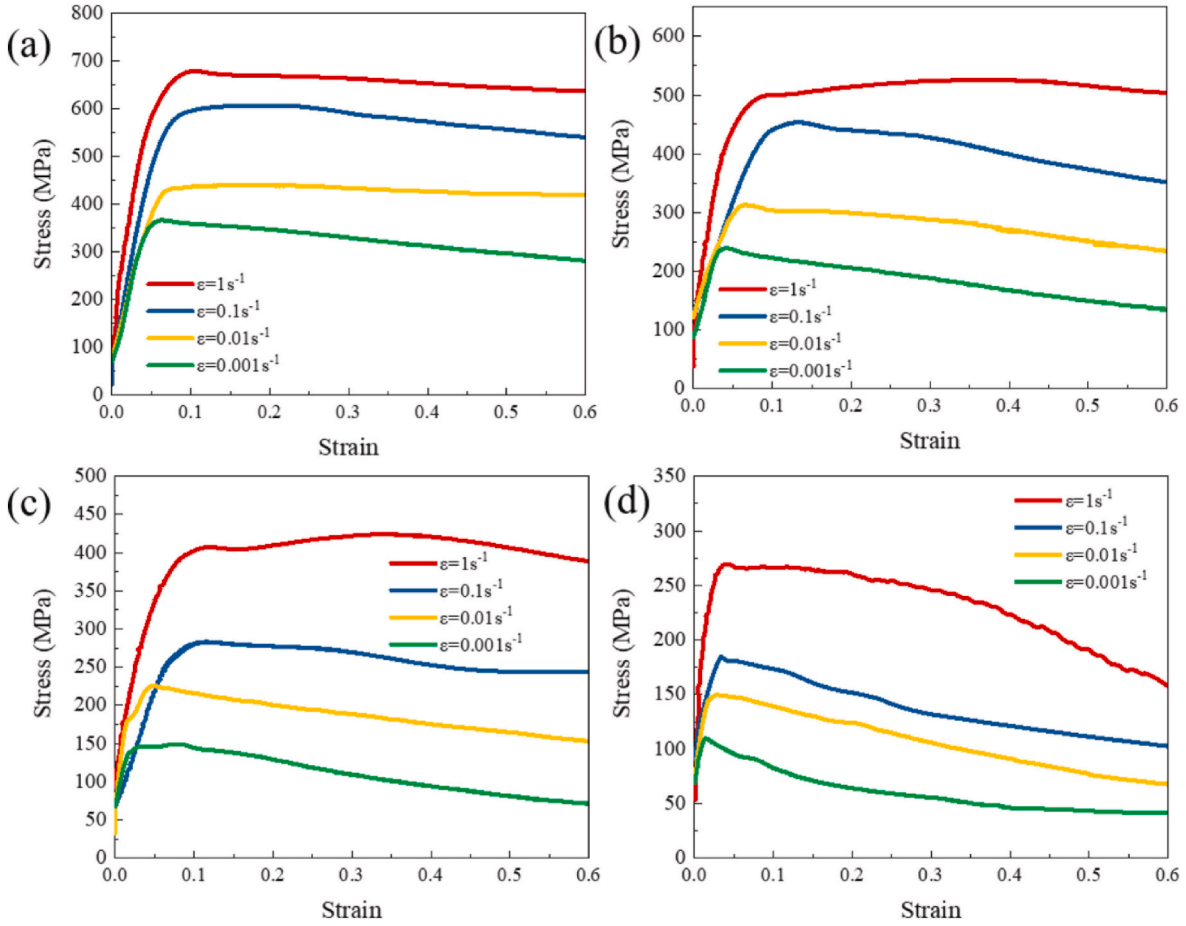

Fig. 9. True stress–strain curves of AlCrFeNi MEA under different forming temperature and strain rates. (a) 800 $^{\circ}C$ (b) 900 $^{\circ}C$ (c) 1000 $^{\circ}C$ (d) 1100 $^{\circ}C$ [53]. Culled with permission from Elsevier.

authors failed to establish this phenomenon in this work.

Guan et al. [49] and Yi et al. [52] investigated the hot working characteristics of Al-free MEAs. They observed a difference in their flow behavior when compared with those reported previously by Qiao and Zhu [53]. Guan et al. [49] studied the hot workability of the CrCoNi MEA at strain rates of 0.001 to 1 s^{-1} and temperatures in the range of 700–1000 ℃ and the flow curves are presented in Fig. 11. It is noted that the change in flow stress at temperatures in the range of 900–1000 °*C* is much lesser when compared to the change in flow stress observed around 700 ℃ at any given strain rate. The flow behavior of the Al-free MEA exhibited no evident peak stress (Fig. 11); instead, the flow stress progressively increases with the activation of multiple dislocations until it attains dynamic equilibrium due to DRV. This flow behavior is quite different from those reported by Qiao and Zhu [53] in Fig. 9. The absence of peak stress may be attributed to the occurrence of a high stacking fault energy (SFE) associated with CrCoNi MEA. The influence of hot-working parameters on the rate of dynamic softening and work hardening is presented in Fig. 12. The positive work-hardening rate persists as true stress rises with true strain. The peak stress is observed in the initial phase of deformation, and the work hardening rate increases at lower temperatures and higher strain rates, reaching zero at a true strain of 0.1.

In a related study, Wang et al. [51] investigated the hot working characteristics of CrCoNi MEA subjected to compression at strain rates of 0.01 to 10 s^{-1} and temperatures ranging from 800 to 1100 ℃. The flow curves presented in this paper showed remarkable similarity with those reported by Guan et al. [49] in Fig. 11. The flow stress diminishes with decrease in strain rate and increasing temperature. It is noted that in the hot deformation process, work hardening prevails over dynamic softening, leading to a continuous upsurge in flow stress with strain. Although the occurrence of peak stress is absent due to the DRX effect, dynamic equilibrium is eventually achieved as the flow stress stabilizes, attributed to the equilibrium between work hardening rate and dynamic softening. The material shows a high strain hardening rate during thermal deformation, and this is attributed to the movement of dislocation nucleation positions towards the grain boundaries from the intragranular sites.

Fu et al. [60] investigated the dynamic deformation characteristics of FeCrNi MEA at various temperatures and strain rates. The compressive yield strength of the MEA rises notably, from 667 MPa to 1312 MPa, as the strain rate intensify from 1×10^{-4} s^{-1}–2410 s^{-1}, indicating considerable sensitivity to strain rate. The results confirm that temperature and strain rates significantly affect the flow behavior of MEAs. The results also suggest that MEAs exhibit characteristic thermal-softening resistance depending on their composition [61]. The hot deformation behavior of FeCrNi MEA was further compared to CoCrFeMnNi HEA. The flow curves and strain hardening response of the MEA and HEA are presented in Fig. 13. The deformation occurred in three distinct stages: I-III. At the initial stage, stress rose to 886 MPa due to dislocation proliferation, leading to strain hardening effect (stage I). Stage II deformation is characterized by severe competition between the dynamic softening effect and strain hardening. In the final deformation process (stage III), flow stress is observed to decline drastically with strain after attaining a peak value of 1480 MPa, and this is due to the effect of localized large plastic work, which led to temperature rise and consequent flow softening. It was observed that the MEAs exhibited a higher strain-hardening rate than the HEA. It is explained that the MEAs were more resistant to thermal softening than the HEAs due to their ability to undergo higher twinning, which results in greater grain refinement than their HEA counterparts [60,62]. According to Fu et al. [60], the mechanism governing the high strain sensitivity of FeCrNi MEA during the thermal deformation process is induced twinning deformation behavior. The emergence of multiple deformation twins within the grains suggests that the FeCrNi MEA has a low stacking fault energy (SFE). In another study, Jiang et al. (2021) confirmed that the strain rate sensitivity (SRS) of $Ni_2Co_1Fe_1V_{0.5}Mo_{0.2}$ MEA is strongly dependent on the deformation temperature and strain rate. It was explained that the flow stress increases with strain rate at lower deformation temperatures (25 °*C*), leading to a positive value of the SRS. At a deformation temperature between 400 and 700 °*C*, the flow stress slightly decreases as the strain rate increases, leading to a decrease in flow serration and a negative regime of SRS. At 800 °*C*, the flow behavior shows a favorable SRS

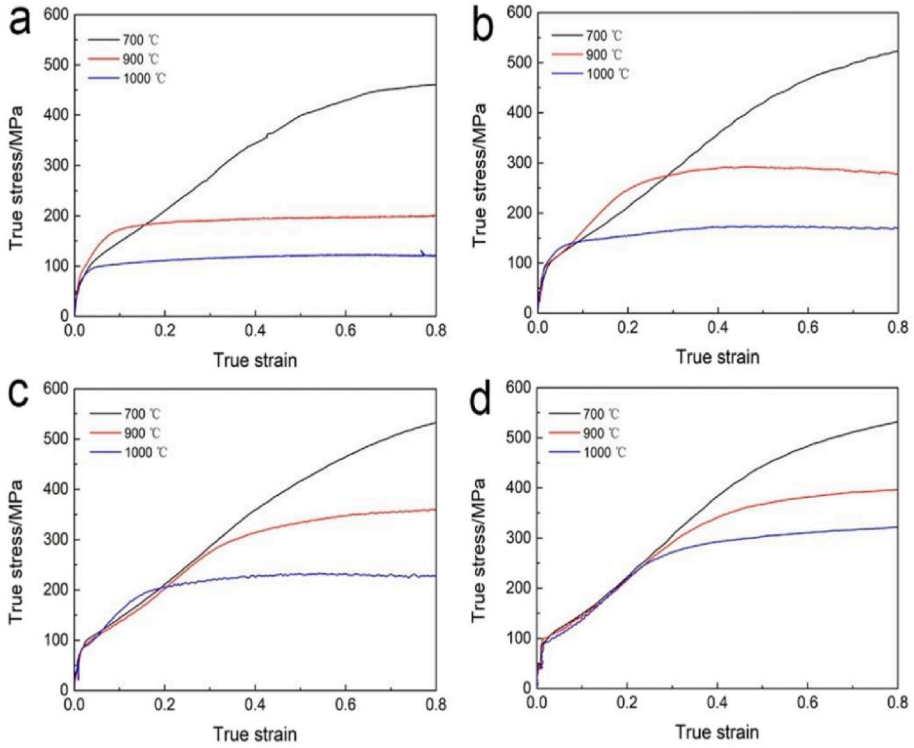

Fig. 11. Flow curves of CrCoNi MEA at different strain rates (a) 0.001 s^{-1} (b) 0.01 s^{-1} (c) 0.1 s^{-1} (d) 1 s^{-1} [49]. Culled with permission from Elsevier.

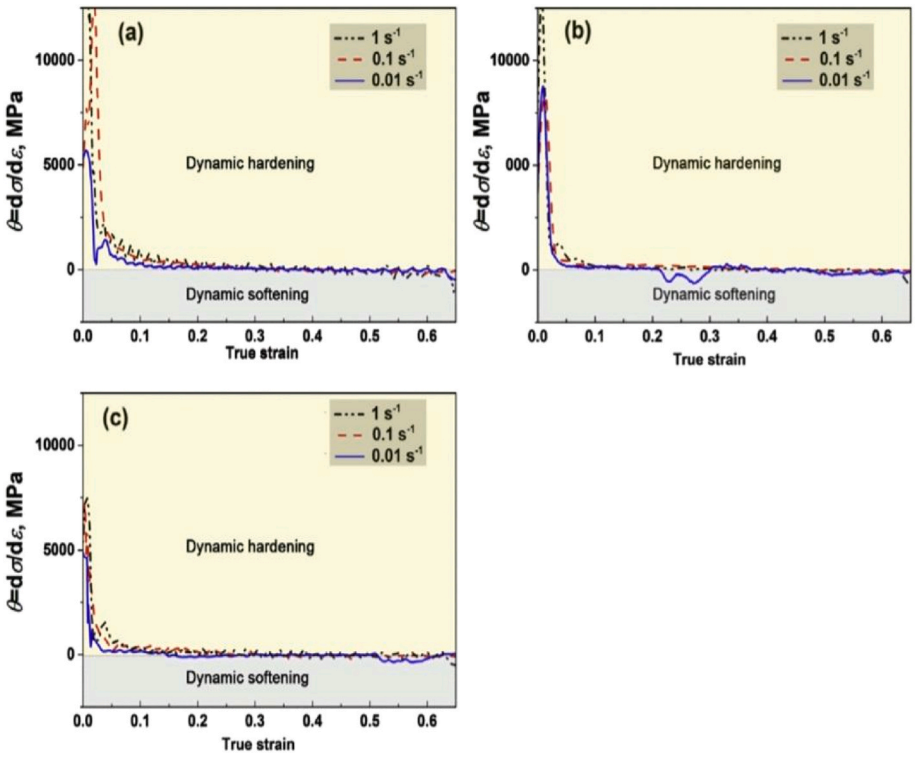

Fig. 12. Effect of strain rate on strain hardening and dynamic softening rate at (a) 900 °C (b) 1000 °C, and (c) 1100 °C [48]. Culled with permission from Elsevier.

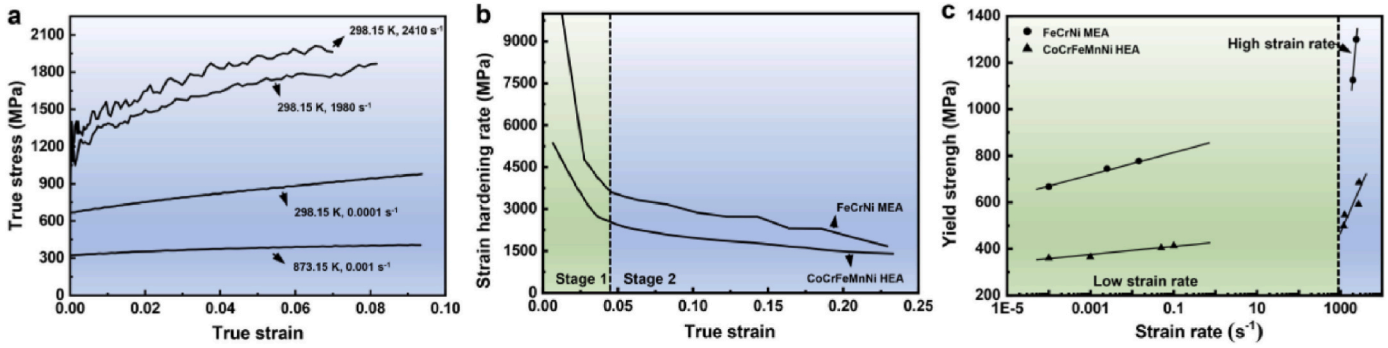

Fig. 13. (a) Flow curves of FeCrNi MEA at various temperatures (b) strain hardening response of FeCrNi MEA and FeCoCrNiMn HEA at strain rate of 10^{-4} s^{-1} (c) Strengths of FeCrNi MEA and the FeCoCrNiMn HEA at varying strain rates [60]. Culled with permission from Elsevier.

regime evident with the increase of flow stress with strain rate and vice versa. It can be deduced from these studies that the thermal deformation of MEA is sensitive to thermally induced microstructural characteristics like deformation twinning, dislocation slip, stacking faults (SFs), solute drag, and diffusion.

4.2. Dynamic softening and deformation mechanisms of MEAs

This section is dedicated to discussions relating to the various dynamic softening and deformation mechanisms of MEAs. Most researchers have shown the hot deformation mechanisms in MEAs to be dependent on deformation temperature, strain, and strain rate [12]. The reason is that strain rate and deformation temperature directly affect the movement of dislocations and migration of grain boundaries. At increasing deformation temperatures, the grain boundaries are thermally activated, leading to dislocation climb and the occurrence of dynamic softening by mechanisms DRV and DRX, usually under conditions of lower strain rates [63]. The mechanism of hot deformation in MEAs is controlled by two competing processes of strain hardening and dynamic softening effects. Under conditions of high deformation temperature and lower strain rates, the grain boundaries accumulate energy and become mobile, resulting in the activation of the DRX process [53]. Formation of DRX grains occurs in MEAs with high stacking fault energy by the mechanism of continuous dynamic recrystallization (CDRX) [48]. MEAs having low stacking fault energy, such as Al–Cr–Fe–Ni MEAs, undergo softening by discontinuous dynamic recrystallization (DDRX) [52,64,65].

Jiang et al. [66] studied the hot deformation mechanisms in $Ni_2Co_1Fe_1V_{0.5}Mo_{0.2}$ MEA at high temperatures. It is observed that dynamic softening occurs by the mechanisms of DRV and DRX. The observation agrees with the report of several authors, including [67,68]. The microstructural evolution associated with the mechanisms of thermal deformation of $Ni_2Co_1Fe_1V_{0.5}Mo_{0.2}$ MEA at varied temperatures and strain rates is presented in Fig. 14. The study observed that the predominant plastic deformation at 25 °*C* is caused by deformation at slip on {111} planes (Fig. 14a). Dislocation interactions related to cross-slip and climb is the dominant deformation mechanism at temperatures in the range of 400–600 °*C*, as shown by the abundance of curved

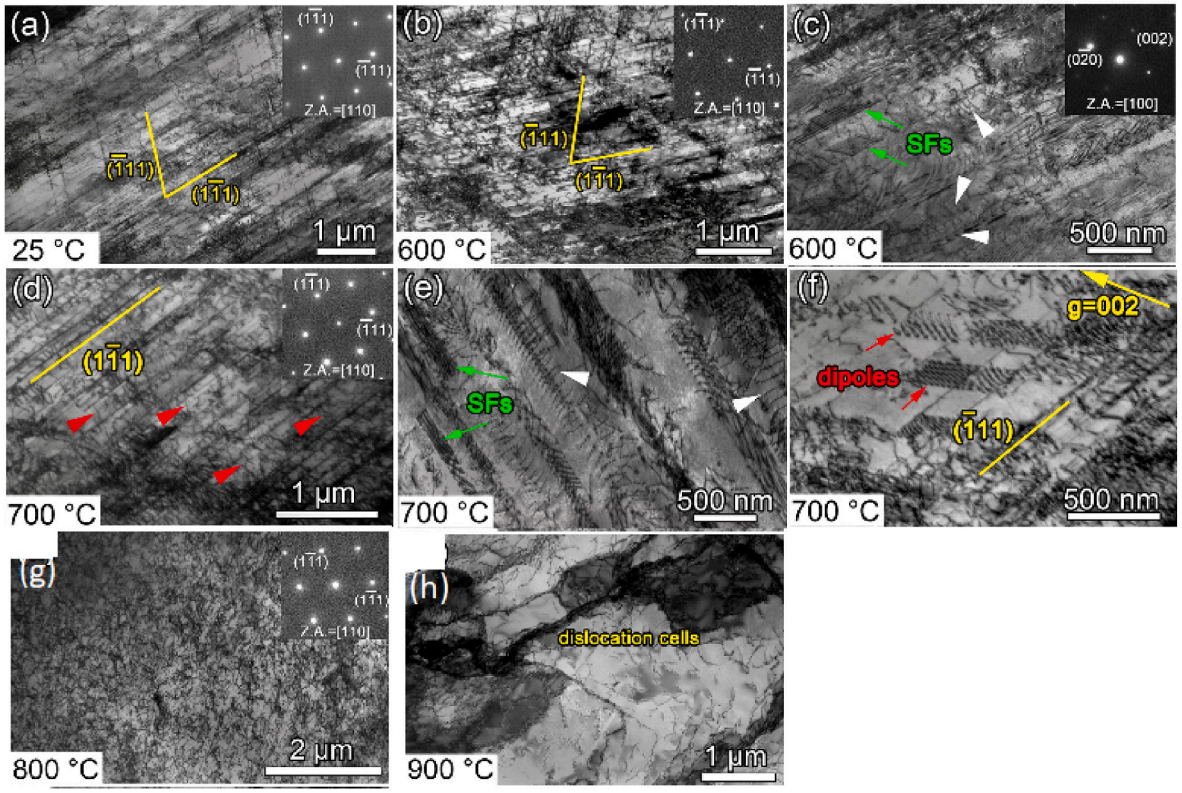

Fig. 14. Microstructural evolution associated with the mechanisms of thermal deformation of $Ni_2Co_1Fe_1V_{0.5}Mo_{0.2}$ MEA at varied temperatures: (a) showing deformation at slip {111} planes at 25 °*C*; (b) and (c) cross-slip and climb dislocations at 600 °*C*; (d), (e), and (f) dislocations, SFs, and dipoles at 700 °*C* (g) homogeneous solute atoms and characteristic cross-slip dislocations at 800 °*C* (h) formation of dislocation cells and DRX grains at 900 °*C*. Culled with permission from Elsevier.

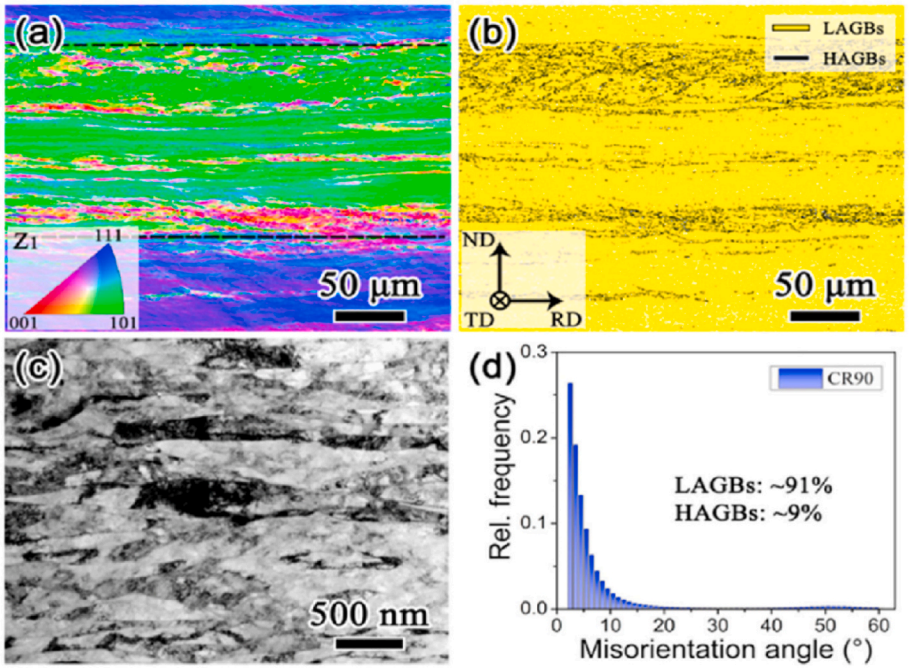

Fig. 15. Microstructures of the cold-rolled Ni_2CoFe MEA (a) EBSD crystal orientation map with IPF color code of Z_1//TD. RD: rolling direction; TD: transverse direction; ND: normal direction. (b) Grain boundary (GB) map with low- and high-angle GBs (LAGBs: 2°–15°, HAGBs: >15°) marked by yellow and black lines, respectively (c) Bright-field TEM image from RD-ND plane. (d) The distribution of the GB misorientation angle [69]. Culled with permission from Elsevier. (For interpretation of the references to color in this figure legend, the reader is referred to the Web version of this article.)

dislocation lines that are not parallel to the {111} planes (Fig. 14b and c). Formation of diverse dislocations (Fig. 14d), SFs (Fig. 14e), and dipole loops (Fig. 14f) emerge as the primary deformation mechanism at 700 °*C*. When deformation temperature rises to 800 °*C*, the free energy of mixing, the diffusivity of solute atoms, and the number of vacancies are all high enough to produce a homogeneous distribution of solute atoms and leading to the activation of cross-slip deformation mechanism (Fig. 14g). At high temperature (900 °*C*), both dislocation cross-slip processes and diffusion-controlled recovery mechanisms dominate the plastic deformation process (Fig. 14h). DRX grains are formed at high deformation temperatures by the mechanism of cell walls and sub-grain boundaries formation.

High deformation temperatures trigger flow softening and suppress the effect of strain hardening mec High deformation temperatures trigger flow softening and suppress the effect of the strain-hardening mechanism of metal flow during the hot deformation process [57]. Gu et al. [69] explained the phenomenon of dynamic softening associated with MEAs from a different point of view. Gu et al. [69] associated the formation of DRX with the interaction of twinning boundaries with the low-angle grain boundaries (LAGBs, 2°–15°) and high-angle grain boundaries (HAGBs, >15°), as illustrated in Fig. 15. The Ni_2CoFe MEA exhibits a high stacking fault energy (SFE), causing plastic deformation through dislocation slip mechanism rather than mechanical twinning. The substantial addition of Cr to the $Ni_2CoCrFe$ MEA resulted in a reduced SFE. However, the alloy nevertheless underwent thermal deformation by the dislocation glide mechanism, which is characterized by the formation of dislocation cells and the appearance of dense dislocation walls in deformed microstructures. This result suggests that the prevalent deformation mechanism during the hot processing of MEAs is highly sensitive to their compositional design. The volume fraction of DRX grains is observed to increase with deformation temperature as DRX grains are formed by annealing twins formation and dislocation migration mechanisms. Wang et al. [70] observed a similar result.

Fu et al. [60] investigated the dynamic deformation behavior of FeCrNi MEA at different strain rates and temperatures. Stacking faults, dislocation slip, slip bands, and deformation-induced twin networks are the primary characteristics of the microstructures of the FeCrNi MEA after hot deformation. The TEM images of FeCrNi MEA at a strain rate of 2410 s^{-1} are presented in Fig. 16. The microstructure confirmed the occurrence of large dislocation cross-slip and dislocation parallel-slip within the grains. Heavy dislocation density is formed at considerable strain, which causes the elongated (deformed) grains to eventually break into fine subgrains, nanotwin structures, and slip bands. The schematic illustration of microstructural evolution and mechanisms of dynamically recrystallized (DRXed) grains formation during hot deformation of FeCrNi MEA is presented in Fig. 17. Random dislocations arise early during the shear deformation process and quickly accumulate along the shear direction, creating channels that later form elongated dislocation cells (Fig. 17a and b). These dislocation cells become narrow as misorientation increases, which eventually transforms them into elongated and small subgrains through the recovery process (Fig. 17c and d). Ultrafine DRX equiaxed grains with high-angle grain boundaries are formed with the rotation of grain boundaries at 30° following the increase in shear stress and deformation temperature (Fig. 17e). DRX grains are observed to nucleate by the mechanism of rotational dynamic recrystallization (RDRX). The MEA exhibited high resistance to dynamic softening due to the deformation twinning, dislocation slip, and deformation-induced stacking fault as described in Fig. 16. Yi et al. [52] studied the DRX mechanism of CoCrNi and $(CoCrNi)_{94}Ti_3Al_3$ MEAs subjected to hot deformation at temperatures and strain rates ranging from 850 to 1100 °*C* and 0.001 to 1 s^{-1} respectively. Deformation of the MEAs is reported to occur by dynamic softening due to dislocation recovery, DRX, and grain growth. It is observed that at higher temperatures and lower strain rates, bands are replaced by thick necklace structures, and the DRX grains nucleate by the mechanism of DDRX through the formation of sub-grain structures within and around the grain boundaries. The discontinuous dynamic recrystallized (dDRXed) grains are characterized by fine structures surrounded by HAGBs, whereas the plastic-deformed grains with a high density of sub-grain are

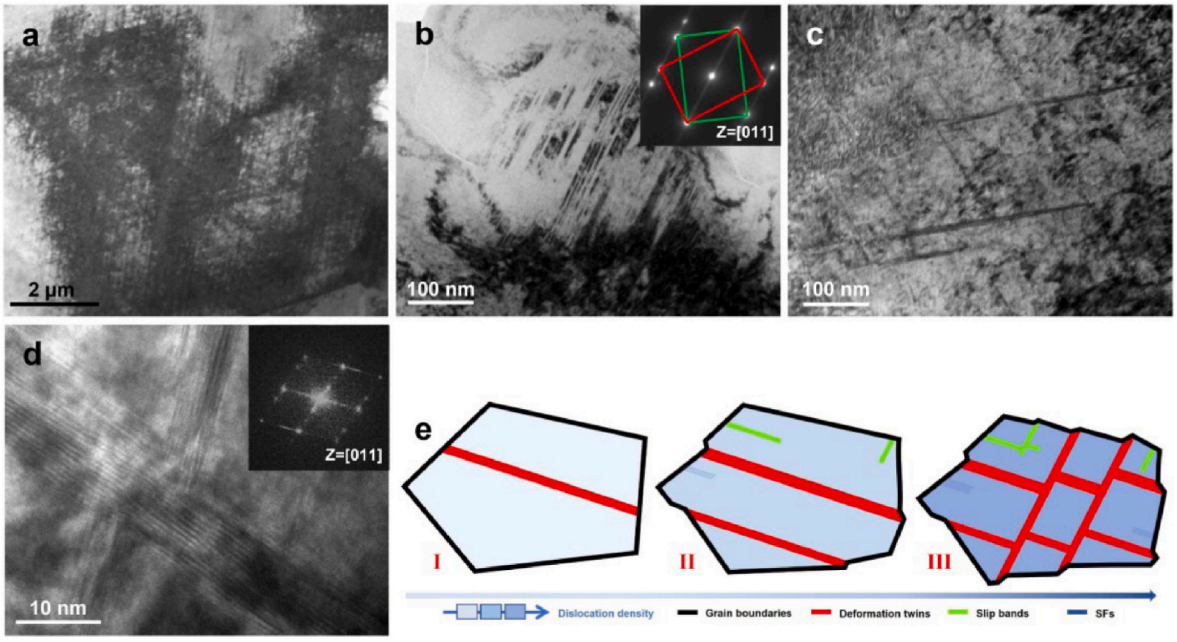

Fig. 16. Microstructural characteristics of the deformed cylindrical specimen conducted at a loading strain rate of 2410 s^{-1}. (a) HAADF TEM image showing the dislocation slip; bright-field (BF) TEM images showing (b) the nanotwins and (c) the multiple nanotwins; (d) HRTEM image showing the multiple nanotwins; (e) schematic diagram of the microstructural characteristics during the deformation process and the darker blue in background color meaning the higher dislocation density. Stage I showing the initial coarse grain, with annealing twins in the grain interior; stage II showing the appearance of stacking faults (SFs), slip bands and deformation induced twins; stage III showing the activation of multiple twinning network systems [60]. Culled with permission from Elsevier. (For interpretation of the references to color in this figure legend, the reader is referred to the Web version of this article.)

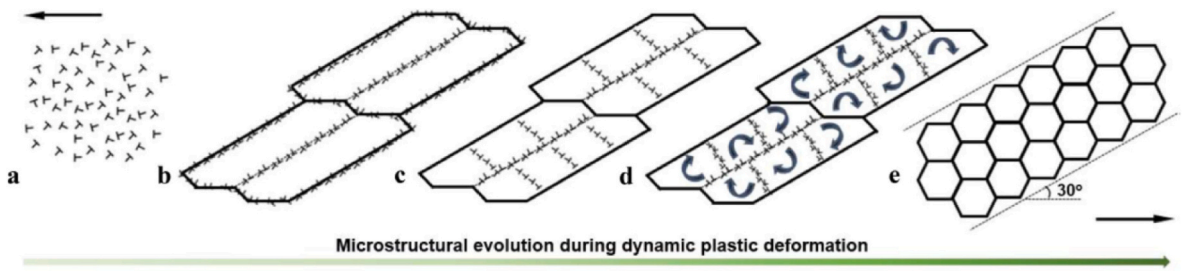

Fig. 17. Schematic illustration of microstructural evolution during hot deformation of FeCrNi MEA (a) Random dislocations; (b) dislocation cells; (c) subgrains; (d) grain boundary reorientation; (e) ultrafine DRXed equiaxed grains [60]. Culled with permission from Elsevier.

coarse. The higher volume fractions of the dried grains are generated under conditions of higher deformation temperatures and lower strain rates during the thermal deformation of the MEA. The condition for achieving a complete DRX grain by DDRX mechanism is found to be at a temperature of 1000 $^{\circ}C$ and a strain rate of 0.001 s^{-1}. Deformation bands surrounded by LAGBs are characteristic structures in the alloy deformed at lower temperatures and higher strain rates. Due to the solid solution hardening effect, the inclusion of Ti and Al into CoCrNi MEA facilitated dynamic recrystallization. The hot deformation characteristics of CoCrNi MEA are found to be sensitive to the alloy constitution (Ti and Al micro-alloying) as well as the hot deformation parameters such as strain, strain rate, and deformation temperature. Schneider and Laplanche [56] studied the mechanism of hot deformation in CrFeNi MEA. Hot deformation of the MEA is reported to occur by accommodating dislocation glide mechanisms at low strains.

At low temperatures and a strain of 1.9%, deformation is characterized by a heavy dislocation network and planar dislocation glide on various slip systems, which are indicative of the dominance of the strain hardening mechanism. At large strains (> 4.5%), deformation is observed to occur by the nanotwinning mechanism. Twining may accelerate the rate of work hardening depending on the temperature because of the dynamic Hall-Petch effect, which is a dynamic decrease in mean grain size with increasing deformation. Deformation by twinning mechanism is observed above a critical resolved shear stress of 165 MPa. The dynamic Hall-Petch effect tends to diminish at high deformation temperatures due to the attendant decrease in the stacking fault energy and resultant annihilation of the dislocation cells. Hua et al. [71] studied the deformation mechanism of CoCrNi MEA subjected to nano-indentation at temperatures ranging from 1 K to 500 K (−272 °C–227 °C). It is observed that the deformation mechanism under high-temperature nanoindentation is heavily influenced by the multiple principal element effect and proceeds by nucleation and movement of dislocations. The study observed that higher temperatures cause thermal vibrations to mobilize partial dislocations that are pinned by local chemical fluctuations and release them during thermal deformation. As the deformation temperature increases, the twin structures disappear, leading to the formation of a prismatic dislocation loop by a thermally activated double cross-slip mechanism. He et al. [48] studied the hot

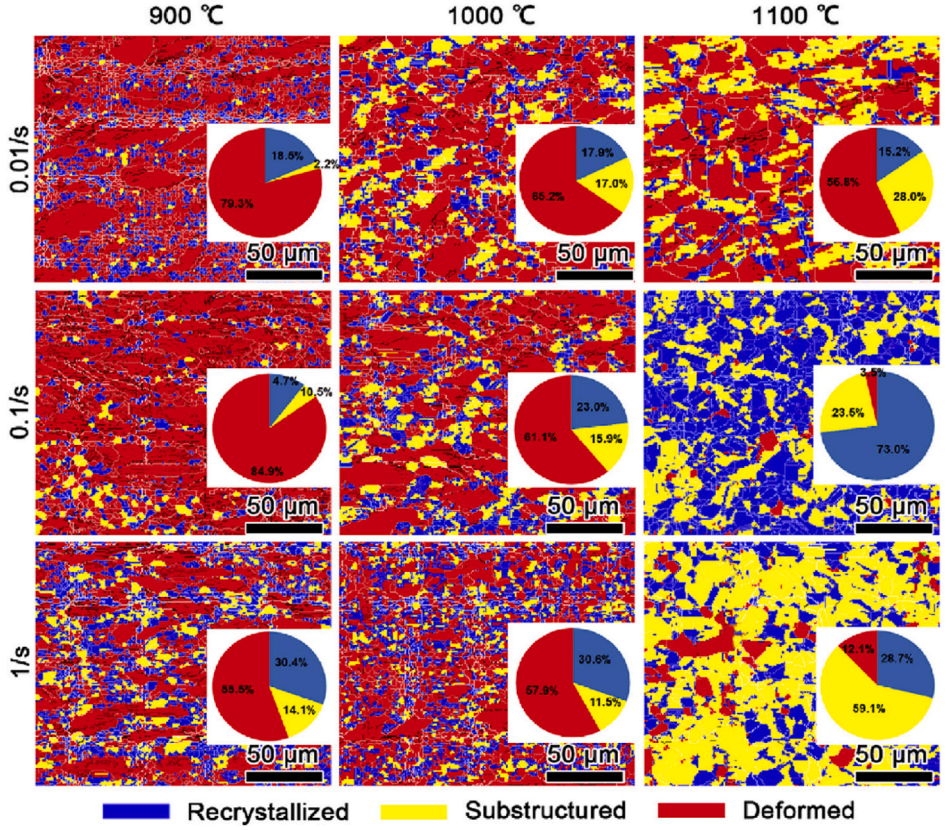

Fig. 18. EBSD images of recrystallized, substructured, and deformed grains in CrCoNi MEA at various deformation parameters. The pie charts illustrate the area fractions of these grains [48]. Culled with permission from Elsevier.

deformation mechanism of CrCoNi MEA subjected to hot deformation at temperatures and strain rates ranges of 900–1000 °*C* and 0.01 to 1 s^{-1}, respectively. The study noted that the hot deformation of CrCoNi MEA occurs by DRX grain formation, as illustrated in Fig. 18. Hot deformation of the MEA is reported to occur by mechanisms of dislocation interactions, DRV, DRX, and grain growth. DRX grains nucleate preferentially at grain boundaries by CDRX mechanism through progressive formation of high angle grain boundaries (HAGBs) within grains at a temperature of 1000 °*C* and strain rates from 0.1 to 1 s^{-1}. The continuous rotation of sub-grains forms the HAGBs. There are several $\Sigma 3$ annealing twins found in the DRX grains, indicating the occurrence of deformation by strain-induced grain boundary migration (SIGBM).

The several mechanisms of hot deformation of MEAs evaluated in this work is summarized in Table 1.

In summary, the numerous studies examined in this section highlight that the flow curves of MEAs are influenced by deformation temperatures, strain, and strain rates (see Table 1). The hot deformation behavior is primarily dictated by the interaction of dislocations with microstructural features, resulting in work hardening, DRV, and/or DRX mechanisms. The hot deformation mechanisms in MEAs are dynamic and, as such, compete for dominance, often transitioning from one mechanism to another based on prevailing parameters like temperature, strain, and strain rate. Conditions of elevated temperatures and lower strain rates favor the DRX softening mechanism, while the work hardening mechanism dominates during the initial deformation stages, typically at lower deformation temperatures. It can be deduced from the works reviewed thus far that as the hot deformation parameter is varied, the prevalent flow mechanism is accompanied by specific structural changes ranging from dislocations and induces twin networks, precipitation, grain boundary migration, and stacking faults to slip band formation. The hot deformation behavior is, therefore, structure-sensitive. Hence, the flow properties can be controlled by tuning the composition of the MEA.

4.3. Reasons for the differences in hot deformation behavior of MEAs and HEAs

It is observed that the flow stress exhibited a decline in response to the decrease in strain rate and increasing temperature. This finding confirms that MEAs, similar to their HEAs counterparts reported in existing literature, exhibit positive strain rate sensitivity [41,42]. Nevertheless, it has been noted that in the hot deformation process, the phenomenon of work hardening predominates during the deformation, thereby resulting in a progressive increase in flow stress with strain due to the activation of multiple dislocations. This resulted in the absence of peak stress in most MEAs reported in this paper [49,60]. The observed phenomena exhibit a contrast to the behavior of HEAs, where the peak stress is often more pronounced at lower levels of strain counterbalanced by the DRX or DRV in the majority of flow curves documented in the currently available study [41,42]. Even while most MEAs do not exhibit the peak stress phenomena, dynamic equilibrium is ultimately reached at higher strain when flow stress stabilizes as a result of the balance between work hardening rate and dynamic softening [49,60].

The MEAs were found to have a higher strain-hardening rate than the HEA, indicating that they were more resistant to thermal softening. This is because the MEAs were able to experience higher twinning, which leads to a larger degree of grain refinement than the HEAs [60,62]. The gradual work hardening behavior, leading to a postponement of necking instability onset, is attributed to the early initiation of deformation twinning at low strains in the MEAs [60,62]. Nevertheless, the heightened resistance to deformation, reflected in the elevated flow stress observed in MEAs. This is undesirable for shaping metallic materials into diverse profiles. This increased resistance implies greater tool wear and higher activation energy during the hot working process, potentially raising the overall cost of metal forming [41]. Therefore, the most suitable processing parameters established by a dynamic materials modeling approach would be highly beneficial. The next section of this study discusses the hot deformation processing map development utilizing the dynamic materials model for the purpose of optimizing the microstructure, mechanical properties, and processing–cost efficiency of hot-working these novel MEAs.

5. Theory of processing maps development from dynamic materials models (DMM)

The hot deformation processing maps serve as visual representations depicting the interplay between temperature, strain rate, and flow stress. These maps are valuable tools for optimizing process parameters and gaining insights into the deformation characteristics of materials. They aid in pinpointing both stable and unstable deformation regions, offering predictions about the microstructure and mechanical properties of a material across varying processing conditions [41,72,73]. Utilizing a processing map is valuable in pinpointing the most suitable processing conditions for materials, mainly when dealing with elevated temperatures and strain rates [74].

To create processing maps, experimental data are collected across various combinations of temperature and strain rate. This data is subsequently subjected to mathematical models and mapping techniques to

Table 1
Hot deformation mechanisms in some MEAs.

References	MEAs	Hot deformation parameters	Hot deformation mechanisms
Jiang et al. [66]	NiCoFeVMo	Hot tensile deformation at the temperature range of 25–1000 °*C* and strain rates of 10^{-2} to 10^{-4} s^{-1}	Hot deformation is characterized by competition between work hardening and dynamic softening. Dislocation interactions govern the work hardening regime while DRV and DRX controls the dynamic softening mechanism
Fu et al. [60]	FeCrNi	The extrusion ratio and temperature are 7:1 and 1150 °*C*, respectively.	Dynamic softening due to the formation of twinning, dislocation slip, and deformation-induced stacking faults. DRX grains are observed to nucleate by the mechanism of rotational dynamic recrystallization (RDRX).
Yi et al. [52]	CoCrNi and $(CoCrNi)_{94}Ti_3Al_3$ MEAs	Hot compression was carried out at temperatures and strain rates ranging from 850 to 1100 °*C* and 0.001 to 1 s^{-1} respectively.	Hot deformation occurred by mechanisms of dislocation recovery, DRX and grain growth. The nucleation of DRX grains occurred by the mechanism of DDRX through the formation of sub-grain structures within and around the grain boundaries.
Schneider and Laplanche [56]	CrFeNi MEA	Hot tensile deformation at a temperature range of 77–873 K (−196 to 600 °C) and strain rate of 10^{-3} s^{-1}	Hot deformation occurs by accommodating dislocation glide mechanisms at low strains. Deformation by twinning mechanism is observed above a critical resolved shear stress of 165 MPa
Hua et al. [71]	CoCrNi MEA	Nanoidentation at temperatures ranging from 1 K to 500 K (−272–227 °C).	The deformation mechanism is heavily influenced by the multiple principal element effects and proceeds by nucleation and movement of dislocations.
He et al. [48]	CrCoNi MEA	Hot compression was carried out at temperatures and strain rates ranging from 900 to 1000 °*C* and 0.01 to 1 s^{-1} respectively.	Hot deformation occurs in mechanisms of dislocation interactions, DRV, DRX, and grain growth. DRX grains nucleate at grain boundaries by CDRX and strain induced grain boundaries migration (SIGBM) mechanisms.

produce contour maps that illustrate distinct deformation mechanisms and material responses [76]. Key parameters, such as power dissipation efficiency, instability parameters, and flow localization indicators, are calculated to interpret the material's behavior during deformation. This method proves highly effective in optimizing process parameters for hot working, and its utilization has extended to enhancing thermal processing technology [41,77].

The theory of processing maps offers a systematic approach to analyzing the behavior of materials during hot deformation. It yields valuable insights into optimizing processing parameters and predicting changes in the material's microstructure by accounting for factors like instability mechanisms, dynamic recrystallization, and energy utilization [76–78]. This theory revolves around two core parameters: strain rate (ε) and temperature (T), along with the material's flow stress. Plotting these parameters logarithmically on a scale allows processing maps to highlight distinct regions corresponding to various deformation mechanisms and microstructural alterations. The foundation of this theory lies in the concepts of instability mechanisms and the dynamic material model [75].

In order to determine the predominant deformation mechanism within different map regions, the instability mechanisms entail an analysis of the strain rate sensitivity exponent (m) and the activation energy for deformation (Q). Instability maps help identify regions where dynamic recrystallization, strain-induced precipitation, or other instabilities occur during deformation [79]. With the use of the dynamic materials model (DMM), data from hot deformation tests can be analyzed to find the dominant deformation mechanisms operative across various temperature-strain rate regimes [80–82].

The dynamic materials model (DMM), initially suggested by Prasad et al. [76], forms the basis for processing maps. It is a potent tool that analyses the data generated by the hot deformation experiments in order to pinpoint the active governing deformation mechanisms in the various temperature-strain rate regions [76]. These models aid in comprehending material flow characteristics during hot deformation and offer guidance for optimizing processing techniques [83]. The dynamic material model takes into account the material's flow stress and the power dissipation ratio to assess its behavior. It also analyses the energy dissipation as a result of microstructural evolution during hot deformation [53,77]. The total power input (P) of the system during the deformation is primarily composed of two distinct quantities, first the dissipative quantity (G) and second the dissipative covariate quantity (J), which are represented in Eq. (1) [53]:

$$P = \sigma\varepsilon = \int_0^{\varepsilon} \sigma d\varepsilon + \int_0^{\sigma} \varepsilon d\sigma = G + J \tag{1}$$

In this context, G represents the dissipative quantity, signifying the energy expended in plastic deformation, primarily transformed into thermal energy. The dissipative covariate quantity J denotes the power expended in the course of microstructure evolution, σ is the flow stress (MPa), and ε is the strain.

At constant T and ε; σ is related to $\dot{\varepsilon}$ by a power law relationship [53] as follows:

$$\sigma = K\dot{\varepsilon}^{m} \tag{2}$$

where m – strain rate sensitivity, K – material coefficient, and $\dot{\varepsilon}$ – strain rate

The quantity of energy dissipated during hot deformation (i.e., the ratio of G & J) [53] can be expressed in terms of m as follows:

$$m = \frac{\partial J}{\partial G} = \frac{\dot{\varepsilon}\partial\sigma}{\sigma\partial\dot{\varepsilon}} = \left|\frac{\partial(ln\,\sigma)}{\partial(ln\,\dot{\varepsilon})}\right| \approx \frac{\Delta log\ \ log\,\sigma}{\Delta log\ \ log\,\dot{\varepsilon}}_{\dot{\varepsilon}T} \tag{3}$$

At constant T and $\dot{\varepsilon}$, the dissipated covariate (J) is given as [79]:

$$J = \int_0^{\sigma} \dot{\varepsilon}\partial\sigma = \frac{m\sigma\dot{\varepsilon}}{m+1} \tag{4}$$

where strain resistivity $(m) = 1$, the dissipation coordination achieves its maximum value J_{max} when the material is in the ideal linear dissipation condition, and J_{max} is consequently given as [79]:

$$J_{max} = \frac{\sigma\dot{\varepsilon}}{2} \tag{5}$$

The power dissipation factor (η), which is the ratio of the actual dissipation coefficient (J) to the maximum dissipation coefficient (J_{max}) is expressed as [53,79]:

$$\eta = \frac{J}{J_{max}} = \frac{2m}{m+1} \tag{6}$$

Eq. (6) establishes a correlation linking the efficiency of power dissipation to the processing parameters. The fluctuation of η concerning the processing parameters—temperature (T) and strain rate (ε)—gives rise to the formation of the power dissipation map. The notion of unstable flow occurring during plastic deformation has been theoretically framed by employing the maximum entropy principle. This principle posits that the generated entropy within the system is lower than the applied strain rate, leading to instability. The application of this principle results in an equation delineating the material's unstable flow during plastic deformation [84].

$$\xi(\dot{\varepsilon}) = \frac{\partial ln\left[\frac{m}{m+1}\right]}{\partial ln\,\dot{\varepsilon}} + m < 0 \tag{7}$$

where $\xi(\dot{\varepsilon})$ is a dimensionless quantity that denotes the instability parameter, the variation of $\xi(\dot{\varepsilon})$ with temperature and strain rate constitutes an instability map.

In the instability map, when the instability parameter $\xi(\dot{\varepsilon})$ is negative, it indicates that flow instability occurred during the deformation in the region [84]. The creation of hot deformation processing maps involves overlaying a power dissipation map and an instability parameter map [79], represented as a plot of logarithmic strain rate against deformation temperatures [85].

5.1. Processing map analysis on MEAs

Processing maps based on the dynamic material model (DMM) have been successfully utilized for the analysis of MEAs for microstructure identification and optimization of deformation parameters. The utilization of hot processing maps empowers the manipulation of MEAs' microstructures, examination of deformation mechanisms, exploration of instability regions, and prognostication of optimal hot deformation parameters, all aimed at achieving favorable material properties. Researchers have delved into the utilization of the theory of processing maps to investigate the hot deformation behavior of MEAs. For instance, the work by Qiao and Zhu [53] focused on the hot deformation of AlCrFeNi MEA and developed processing maps to optimize the processing parameters. The processing map was utilized to evaluate the inherent processability of AlCrFeNi MEA and aid in identifying the optimal deformation parameters to enhance workability. Hot compression tests were conducted at diverse temperatures ranging from 800 °C to 1100 °C, along with different strain rates ranging from 0.001 s^{-1} to 1 s^{-1}. According to the processing map (illustrated in Fig. 19), the optimum zone lies within a temperature range of 950–1050 °C and a strain rate range of 0.001–0.01 s^{-1}. This region falls within the stable region, characterized by high power dissipation efficiency and the avoidance of flow instability.

Consequently, it ensures the most efficient energy dissipation during hot deformation while sidestepping flow instability. Thus, this parameter becomes the most desirable choice for achieving the desired

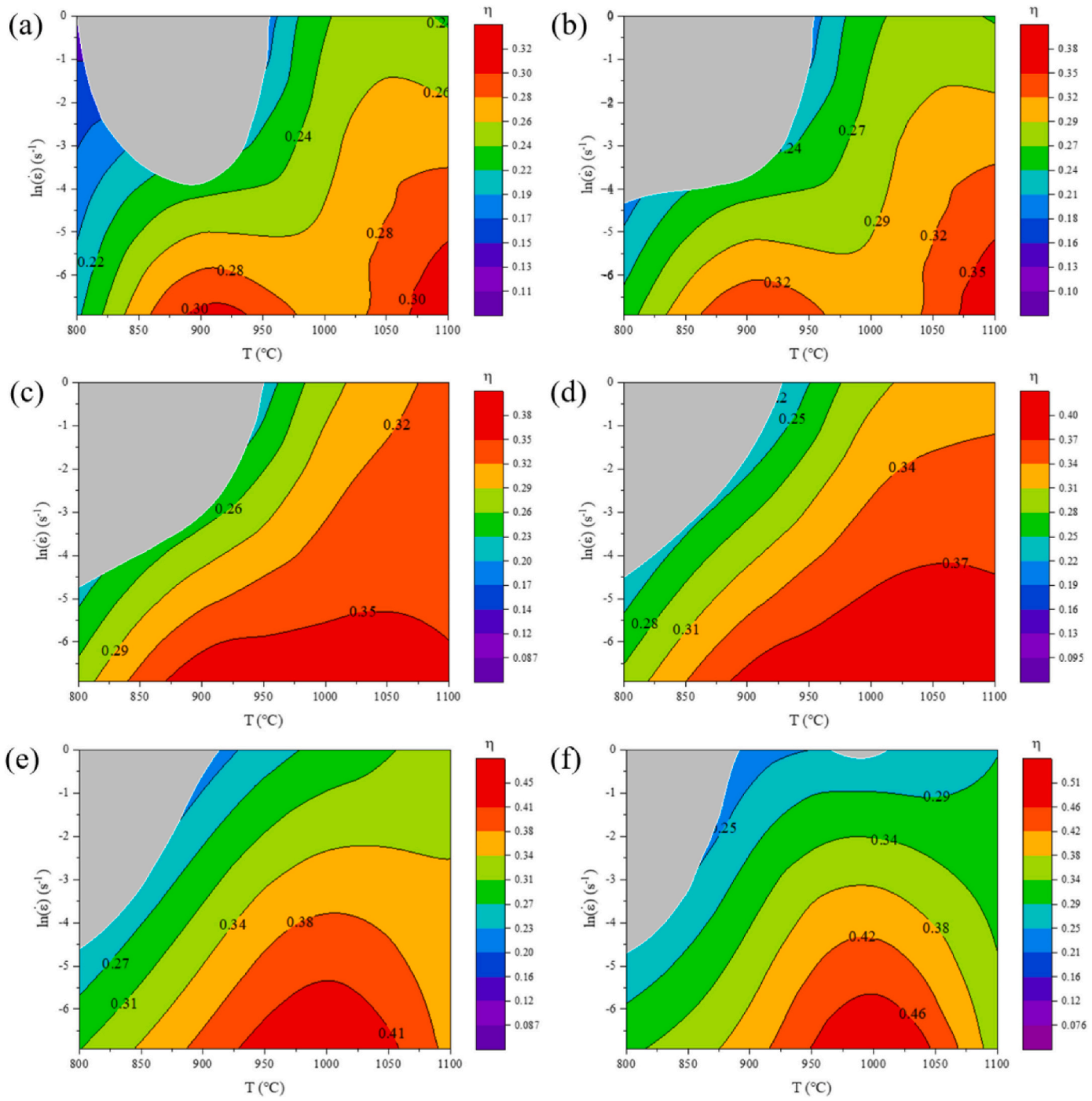

Fig. 19. Processing maps of AlCrFeNi at different strains (a) $\varepsilon = 0.1$ (b) $\varepsilon = 0.2$ (c) $\varepsilon = 0.3$ (d) $\varepsilon = 0.4$ (e) $\varepsilon = 0.5$ (f) $\varepsilon = 0.6$ [53]. Culled with permission from Elsevier.

deformation behavior and mechanical properties of AlCrFeNi MEAs. The unsafe region (flow instability) occurs at low deformation temperatures of 800–950 °C and high strain rates exceeding 0.1 s^{-1}, with the microstructure at the plastic deformation instability mainly composed of micro-defects such as cracks.

Conversely, the safe region (flow stability) emerges at temperatures above 950 °C and strain rates below 0.01 s^{-1}; the microstructure within the plastic deformation stability region exhibits a uniform and fine-grained structure, indicating the absence of micro-defects like cracks. This uniform and fine-grained structure resulted from dynamic recrystallization (DRX) during the deformation process. Notably, the primary deformation mechanism for the AlCrFeNi alloy appears to be DRX. According to the authors, the flow stress initially increases and then consistently decreases with increasing strain, which is a typical hallmark of DRX in the hot deformation process.

Another study conducted by Nayan et al. [86] demonstrated the use of processing maps for analyzing the hot deformation behavior of multi-component alloys and understanding their microstructure and mechanical characteristics under varying processing conditions. Hot-compression tests were carried out over a temperature range of 800 °C–1030 °C and strain rates ranging from 10^{-3} to 10^{-1} s^{-1}. According to the processing map generated for the NiTiCuFe multi-component alloy, the stable domain spans temperatures from 900 °C to 1030 °C and strain rates from 10^{-3} to $10^{-1.2}$ s^{-1}. In this region,

deformation predominantly occurs through dislocation glide mechanisms coupled with the fragmentation of the dendrites. These mechanisms resulted in a crack–free microstructure composed of bonelike and continuous saw-tooth features observed within the microstructure of the stable regime. Conversely, unstable deformation occurs within temperature ranges of 800 °C–1020 °C, combined with respective strain rates of 10^{-3} to 10^{-1} s^{-1}. The unstable regime exhibits microstructural instabilities (mainly the high extent of wedge cracks found in their microstructures) originating from localized plastic flow or adiabatic shear banding.

Within this stable region, the material undergoes deformation via multiple mechanisms, including dislocation glide and DRX, leading to favorable microstructures suitable for engineering applications. These conditions are considered the optimum thermomechanical processing (TMP) conditions, striking a balance between plastic deformation stability and workability, resulting in high power dissipation efficiency and favorable mechanical properties.

Zhang et al. [77] investigated the hot deformation behavior of $CrFeNiSi_{0.15}$ alloy, a novel MEA with high-temperature stability, excellent mechanical properties, and significant potential for industrial applications. This was accomplished through isothermal compression tests spanning a temperature range of 900–1200 °C and a strain rate range of 0.001 to 1 s^{-1}. Utilizing the dynamic material model (DMM), the processing map for $CrFeNiSi_{0.15}$ MEA was formulated. These maps serve to depict the interplay between energy consumption and structural alterations during the thermal deformation of the alloy.

Based on the processing map obtained from the article, the domain of apparent flow stability for $CrFeNiSi_{0.15}$ MEA was identified within the temperature range of 900–1100 °C and a strain rate range of 0.01 to 10 s^{-1}. Selecting appropriate deformation parameters from this range could enhance the material's processing performance, aligning it with secure regions for thermomechanical processing. Within the stability region, microstructure evolution primarily involves full DRX. Full DRX occurs by the reduction of subgrains and LAGBs as a result of continuous absorption of dislocations within the grains by the subgrains boundaries during the DRX process, which can be converted into HAGBs of new grains. This phenomenon pointed to DDRX as the dominant nucleation mechanism in this region.

In contrast, the instability region primarily resides in the temperature range of 900–985 °C and a strain rate range of 0.12 to 1 s^{-1}. Here, the microstructure features inhomogeneous material flow, leading to crack formation and material fracture during deformation. This instability can be attributed to the notable velocity gradient of the material within the processing map's instability region, which contributes to shear bands and other forms of non-uniform deformation, ultimately leading to crack formation. At lower temperatures, like 900 °C, the sluggish dislocation movement results in the accumulation of dislocations at grain boundaries, promoting grain boundary cracking. The processing map analysis indicates optimal working conditions for $CrFeNiSi_{0.15}$ MEA within the two domains. The first domain spans a temperature range of 900–985 °C and a strain rate range of 0.001 to 0.12 s^{-1}, while the second domain extends from 985 to 1200 °C with a strain rate range of 0.001 to 10^{-1} s^{-1}. The processing map reveals that the alloy's efficiency value increases with rising deformation temperature in the high strain rate domain (0.05 to 1 s^{-1}) yet decreases with declining strain rate in the high-temperature range (1100–1200 °C). The alloy achieves peak efficiency at around 39% under a deformation parameter of 1200 °C/1 s^{-1}. This study further unveils the complete dynamic recrystallization occurring at this specific parameter.

Wang et al. [51] conducted hot compression tests on the CrCoNi alloy and developed processing maps across a deformation temperature range of 800–1100 °C and a strain rate of 0.01–10 s^{-1}. The processing map for the CrCoNi alloy was categorized into two distinct domains defined by power dissipation efficiency and instability criteria. From the processing map, Domain I represented the instability domain. This domain corresponds to samples deformed under lower temperatures and higher strain rate conditions, exhibiting lower power dissipation efficiency. The microstructure in this zone primarily consisted of elongated grains with a non-uniform size distribution. This characteristic of dominance by dynamic recovery (DRV) as DRX grains was not observed in the microstructure because recrystallization commences at deformation temperatures below 900 °C.

On the processing map, Domain II, in contrast, represents the stability region. This region corresponds to specimens deformed at elevated temperatures and lower strain rates. The stability domain of the CrCoNi alloy demonstrated a wider scope, with strain having minimal impact on processing performance. The microstructure within this region predominantly comprised equiaxed grains displaying a uniform size distribution, which is due to the higher temperatures and lower strain rates that allow the material to undergo DRX and produce a more homogeneous structure, which makes the DRX process dominant in this region. From the processing map, the safe region for the CrCoNi alloy during thermal deformation spanned two ranges: a deformation temperature span of 800–900 °C and a strain rate interval of 0.01–0.02 s^{-1}, alongside a deformation temperature range of 900–1100 °C and a strain rate range of 0.02–10 s^{-1}. The optimal zone for the CrCoNi alloy within thermal deformation was established to be the deformation temperature range of 900–1100 °C and the strain rate range of 0.01–0.1 s^{-1}. Within this zone, the alloy exhibited high power dissipation efficiency and decreased instability, indicating efficient processing with minimal risk of deformation failure. The flow stress values of the alloy within this zone were also relatively low, underscoring the alloy's facile deformation potential within this parameter range. These findings were instrumental in identifying safe processing conditions that lead to desired microstructures and mechanical properties.

In summary, it was observed that the MEAs showed optimal processing features with deformation conditions of high temperature and lower strain rates for predominantly most of the alloys studied in this section (see Table 2). In these conditions, the microstructure of the MEAs is comprised of more homogenous structures with refined grains that are uniformly distributed. In contrast, the instability regions were mainly observed at low temperatures and high deformation strain rates. The dominant microstructural features at these instability regions show defects such as micro-cracks, grain boundary cracking as a result of sluggish dislocation movement, localized plastic flow or adiabatic shear bands, and inhomogeneous materials flow.

Therefore, the hot deformation processing map analysis provides a comprehensive approach to unraveling the complex behavior of multicomponent alloys under extreme thermal conditions. By merging graphical representation with theoretical insights, this methodology empowers material scientists to finely adjust processing parameters and anticipate microstructural changes, thus propelling material design and engineering. Integrating theoretical frameworks with empirical data equips researchers to calibrate processing parameters precisely and foresee shifts in microstructural dynamics, ultimately fostering significant progress in the hot deformation studies of MEAs.

6. Constitutive description of material flow in medium entropy alloys

Material scientists have shown significant interest in incorporating constitutive models to explain the behavior of metallic systems under diverse deformation conditions, including deformation temperatures, strain, and strain rates. This interest is particularly evident in the realm of implementing hot deformation techniques like forging, rolling, and extrusion, among other related processes. The primary goal in developing these models was to offer a comprehensive understanding and analysis of the behavior exhibited by metallic systems during hot deformation processes [41]. The effectiveness of these models as input frameworks in the finite element technique for optimizing the hot working process has led to the achievement mentioned earlier. Traditionally, studying the hot deformation properties of metallic materials

Table 2
Summary of the optimum hot working regimes and instability regimes in different MEA systems with their corresponding microstructural transitions under different deformation parameters.

S/N	Author	Composition	Deformation parameters	Initial microstructure	Final microstructure	Safe hot working regime	Unsafe hot working regime
1	Qiao and Zhu [53]	AlCrFeNi	Hot compression from 800 °C to 1100 °C and 0.001 s^{-1}–1 s^{-1}.	The MEA is primarily composed of a disordered BCC (A2) phase and an ordered BCC (B2) phase. The grain boundaries correspond to the Fe–Cr rich BCC phases and the ultrafine interconnected phases are Ni–Al rich phases.	–	Safe working regions occurred at T and $\dot{\varepsilon}$ of >950 °C and 0.01 s^{-1}	Unsafe region occurred at T and $\dot{\varepsilon}$ of 800~950 °C and >0.1 s^{-1}
2.	Nayan et al. [86]	NiTiCuFe	800 °C to 1030 °C) and strain rate of 10^{-3} t0 10^{-1} s^{-1}, and true strain rates, 10^{-3}, 10^{-2}, and 10^{-1} s^{-1} to true strains, ε, of ~0.7	The microstructure was composed of two solid-solution phases; BCC and FCC dendritic grains with bone-like and saw-tooth features	BCC Fe-rich, BCC b-Ti-rich, FCC Cu-rich, and FCC Ni-rich solid-solution phases.	Safe working regions occurred at T and $\dot{\varepsilon}$ of 900 °C–1030 °C and of 10^{-3} to $10^{-1.2}$ s^{-1}	The unstable deformation of the multi-component alloy occurs at T = 800 °C–880 °C and $\dot{\varepsilon} = 10^{-3}$ to $10^{-1.4}$ s^{-1} as well as T = 950 °C–1020 °C and $\dot{\varepsilon} = 10^{-1.4}$ to 10^{s} s^{-1}
3.	Zhang et al. [77]	$CrFeNiSi_{0.15}$	Isothermal compression tests.	Equiaxed grains with an average size of about 186.41 ± 6.28 μm.	A fine and homogenous grain, formed through dynamic recrystallization (DRX).	Two safe regions exist 900–985 °C/0.001–0.12 s^{-1} and 985–1200 °C/ 0.001 – 1 s^{-1}	The unsafe region occurred at T and $\dot{\varepsilon}$ of 900–985 °C and 0.12 to 1 s^{-1}.
4.	He et al. [48]	CrCoNi	Hot compression from 900 °C to 1000 °C and 0.01 to 1 s^{-1}	The microstructure of the MEA was composed of uniform grains with an average grain size of about 20 ± 0.8 μm,	In general, a typical necklace structure is detected in the CrCoNi specimens compressed at 900 °C, The necklace structure disappears gradually with increasing temperature and more equiaxed grains are observed.	–	–
5.	Jiang et al. [46]	$Ni_2Co_1Fe_1V_{0.5}Mo_{0.2}$	Tensile creep tests at the temperature range of 973–1073 K (700–800 °C) under initial applied stresses of 150–200 MPa.	The microstructure of the as-annealed MEA which is composed of coarse grains mostly in mm.	Under low stress, temperature and strain rate, the microstructure was composed of planar dislocations with random entanglements; high stress, low temperature and low to medium strain rate; microstructures were homogeneous scattering of curved dislocations; microstructures composed of sub-grain structures under the low stress, high temperature and high strain conditions.	–	–
6.	Wang et al. [51]	CrCoNi	Hot compression at 800–1100 °C and strain rate range of 0.01–10 s^{-1}.	The as-cast material was composed of FCC.	Equiaxed grains with uniform grain size was observed due to DRX	Two safe regions exist, the first at T and $\dot{\varepsilon}$ of 800–900 °C and 0.01–0.02 s^{-1}, and the second at T and $\dot{\varepsilon}$ of 900–1100 °C and of 0.02–10 s^{-1} respectively	The unsafe region occurred at T and $\dot{\varepsilon}$ of 900–1100 °C and 0.02–10 s^{-1}
7.	Tran et al. [43]	CrCoNi	Hot Isostatic Pressing (HIP) at 1150 °C, 1000 atm for 4 h.	The as-built CrCoNi MEA-DED shows primarily elongated columnar grain structure with LAGBs features surrounded by high angle grain boundaries (HAGBs) indicating the inhomogeneous microstructure due to fast cooling during the DED process.	The HIP treated CrCoNi MEA-DED reveals the grain structure with an equiaxed morphology. After HIP treatment, a significant amount of recrystallization twins, indicating the relaxation of internal residual stresses.	–	–
8.	Guan et al. [49]	CrCoNi	Hot compression at 700–1000 °C and strain rate range of 0.001–10 s^{-1}.	The as-cast MEA exhibits a coarse-grained structure. The average grain size is 200 ± 50 μm	The deformed samples possess increased amounts of recrystallized grains as the strain decreases at high temperatures.	–	–

involved a trial-and-error approach, proven to be both costly and time-consuming [41]. The precise prediction of flow stress using different constitutive models has attracted considerable attention among researchers working on the hot deformation of metallic systems. Finite element methods have been applied to integrate these models into simulation processes, enabling researchers to quickly comprehend and enhance the deformation characteristics of alloys and composites. Constitutive models play a crucial role in accurately predicting flow stresses, as well as facilitating the calculation of activation energy and stress exponents. These parameters are not only valuable in identifying the type of mechanism governing deformation but also in evaluating the comparative hot workability of a material. In the subsequent sub-sections, the various models used in predicting the hot deformation flow stress, the mechanisms influencing deformation in MEAs, and the relative hot workability of MEAs are discussed.

6.1. Constitutive analysis (kinetic analysis of deformation)

$$Q = R\left\{\frac{\partial ln\ \ ln\ \dot{\varepsilon}}{\partial ln\ \ ln\ [sinh\ \ sinh\ (\alpha\sigma)]}\right\}_T \left\{\frac{\partial ln\ \ ln\ [sinh\ \ sinh\ (\alpha\sigma)]}{\partial(1/T)}\right\} = Rn'\left\{\frac{\partial ln\ \ ln\ \sigma}{\partial(1/T)}\right\}_{\dot{\varepsilon}} = R\beta\left\{\frac{\partial \sigma}{\partial(1/T)}\right\}_{\dot{\varepsilon}} = Rn\left\{\frac{\partial ln\ \ ln\ [sinh\ \ sinh\ (\alpha\sigma)]}{\partial(1/T)}\right\}_T \tag{18}$$

Constitutive equations play a crucial role in defining the deformation process of any material system, taking into account the thermo-mechanical processes that govern the conditions of grain refinement. The commonly employed constitutive equation is the Arrhenius type, which characterizes deformation parameters like flow stress, deformation temperature, and strain rate. These parameters are integrated and represented through the Zener-Holloman parameter (Z), as depicted in Eqs. (8)–(13) [42,87–89]. Eqs. (9)–(11) represent the power, exponential, and hyperbolic-sine laws, respectively.

$$Z = \dot{\varepsilon}\ exp\left(\frac{Q}{RT}\right) = Af(\sigma) \tag{8}$$

$$Z = \dot{\varepsilon} exp\ \ exp\left(\frac{Q}{RT}\right) = A\sigma^n \tag{9}$$

$$Z = \dot{\varepsilon}\ exp\left(\frac{Q}{RT}\right) = A_2\ exp\ (\beta\sigma)^{n'} \tag{10}$$

$$Z = \dot{\varepsilon} exp\ \ exp\left(\frac{Q}{RT}\right) = A_3[sinh\ (\sigma\alpha)] \tag{11}$$

$$\dot{\varepsilon} = A[sinh\ \ sinh\ (\alpha\sigma p)\ ]^n\ exp\left(\frac{-Q}{RT}\right) for\ all\ \sigma \tag{12}$$

$$\sigma = \frac{1}{\alpha} ln\left\{\left(\frac{Z}{A}\right)^{\frac{1}{n}} + \left[\left(\frac{Z}{A}\right)^{\frac{2}{n}} + 1\right]^{\frac{1}{2}}\right\} \tag{13}$$

In the equations, $\boldsymbol{\varepsilon}$, Q, n, R, $\boldsymbol{\sigma}$, T represent the strain rate in s^{-1}, activation energy in J/mol, stress exponent, gas molar constant (8.314 J/mol.K), the stress in MPa, and deformation temperature, respectively. The values $\boldsymbol{\alpha}$, A, *and* $\boldsymbol{\beta}$ are material constants. Many researchers use Eq. (13) to represent the constitutive equation for material alloy systems. The values of $\boldsymbol{\alpha}$, A (s^{-1}), n, and Q (kJ/mol) are crucial in modeling the deformation behavior of MEAs. The equation for strain rate can also be expressed as Eq. (14):

$$\dot{\varepsilon} = AF(\sigma) exp\ \ exp\left[-\frac{Q}{RT}\right] \tag{14}$$

$$F(\sigma) = \{A'\sigma^{n'} < 0.8\ A''\ exp\ (\beta\alpha)\alpha\sigma > 1.2\ Asin\ h^n(\alpha\sigma)\ \text{for all values of}\ \alpha\sigma \tag{15}$$

The expression in Eq. (15) is utilized in designing the pathways for representing the flow stress. A flow stress curve for martensitic stainless steels was designed by Derazkola et al. [78]. The strain rate formula can be reformulated in Eqs. (16) and (17). Furthermore, by taking the log function of both sides in Eq. (18), the activation energy is formulated in Eq. (18) and determined using Eq. (19). Similarly, by taking the log function of Eqs. (16) and (17), the constants n′, n, $\boldsymbol{\alpha}$, *and* $\boldsymbol{\beta}$ can be determined and expressed in Eqs. (20)–(23) [78,90,91].

$$ln\ \ ln\ \dot{\varepsilon} = n'\ ln\ \ ln\ \sigma + ln\ A' - \frac{Q}{RT} \tag{16}$$

$$ln\ \ ln\ \dot{\varepsilon} = \beta\sigma + ln\ \ ln\ A'' - \frac{Q}{RT} \tag{17}$$

$$ln\ \ ln\ [sinh\ \ sinh\ (\alpha\sigma)] = -\ ln\ \ ln\ A \Big/ n + ln\ \ ln\ \dot{\varepsilon} \Big/ n - \frac{Q}{nRT} \tag{19}$$

$$n' = \left[\frac{\partial ln\ \ ln\ \dot{\varepsilon}}{\partial ln\ \ ln\ \sigma}\right]_T = \left[\frac{\partial ln\ \ ln\ \sigma}{\partial ln\ \ ln\ \dot{\varepsilon}}\right]_T^{-1} \tag{20}$$

$$\beta = \left[\frac{\partial ln\ ln\ \dot{\varepsilon}}{\partial \sigma}\right]_T = \left[\frac{\partial \sigma}{\partial ln\ \ ln\ \dot{\varepsilon}}\right]_T^{-1} \tag{21}$$

$$\alpha = \frac{\beta}{n'} \tag{22}$$

$$n = \left[\frac{\partial ln\ \ ln\ \dot{\varepsilon}}{\partial ln\ \ ln\ (sinh\ \ sinh\ (\ \alpha\sigma)\ \alpha\sigma) sinh\ \ sinh}\right]_T \tag{23}$$

n is determined from the slope of the ln $\boldsymbol{\varepsilon}$ vs. ln $\boldsymbol{\sigma}$, and the value Q/n is used in getting the experimental values of Q, determined from the slope of ln $\boldsymbol{\sigma}$ vs. 1/RT. These values are used in calculating the power creep law expressed in Eq. (24), where G, b, and D represent the shear modulus, magnitude of the Burgers vector, and diffusion coefficient. Hot deformation mechanisms are either by climb-controlled or viscous glide technique. The value of n' determines whether the deformation technique is a climb-controlled or viscous glide technique. n' values ~2, the mechanism of deformation is by grain boundary sliding, but at values of ~3–4, the mechanism of deformation is by the viscous glide of dislocation; at ~4.5 to 6, the mechanism of deformation is by dislocation climb, while values above 8 signify cross-slip of screw dislocation [92].

$$\dot{\varepsilon} \propto \frac{GbD}{kT}\left(\frac{b}{d}\right)^p \left(\frac{\sigma}{G}\right)^{n'};\ D \propto exp\ (-Q\ /\ RT) \tag{24}$$

MEAs is a novel field of research with few researchers employing constitutive equations to analyze the alloys' hot deformation behavior. The research includes Wang et al. [51], Yi et al. [52], Jiang et al. [46], and Qiao and Zhu [53]. The researchers utilized the Arrhenius equation in modeling the constitutive equations. In Qiao and Zhu's [53] research on CrCoNi, the values of n and A are obtained from the slope and intercepts of ln Z and ln (sinh ($\boldsymbol{\alpha\sigma}$)) shown in Fig. 20. The hot deformation parameters for developing the hyperbolic sine law for MEAs from the

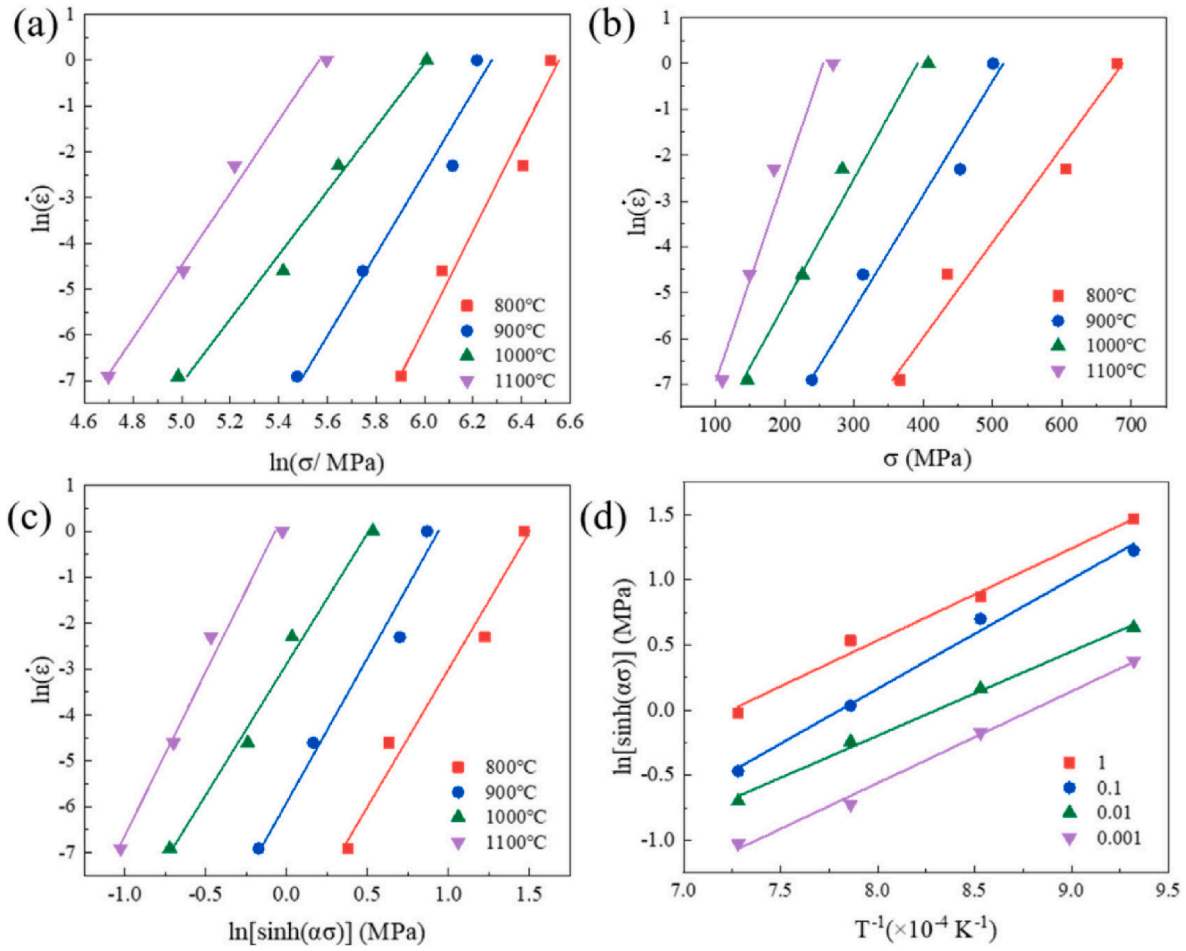

Fig. 20. Diagram of strain rate and flow stress at different temperatures. (a) β plot (b) n' plot (c) n plot (d) Q plot [53]. Culled with permission from Elsevier.

three research are shown in Table 3.

6.2. Model validation

Many models, such as the Arrhenius model, Artificial Neural Network model, Zerilli-Armstrong model, and Johnson-Cook model, have been utilized to predict the hot deformation behavior of many alloys. However, modeling the hot deformation behavior of MEAs is still relatively new, making the Arrhenius model the only utilized technique for the hot deformation of MEAs. The accuracy of the models is evaluated using statistical techniques such as regression (R), root square mean (RMSE), average absolute relative (AARE), relative error (RE), and

Table 3
Hot deformation parameters of the hyperbolic sine law for MEAs.

MEAs	α (MPa^{-1})	Strain	Deformation parameter	Dominant Deformation Mechanism	A (s-1)	n	Q (kJ/mol)	Reference
CrCoNi	0.004480	0.20	800 °C–1100 °C 0.01 s^{-1}–10 s^{-1}	DRX	1.9552×10^{23}	14.696	348.91	[51]
CrCoNi	0.004159	0.25	800 °C–1100 °C 0.01 s^{-1}–10 s^{-1}	DRX	7.70699×10^{22}	12.824	376.17	[51]
CrCoNi	0.003906	0.30	800 °C–1100 °C 0.01 s^{-1}–10 s^{-1}	DRX	4.8966×10^{23}	12.155	409.96	[51]
CrCoNi	0.003714	0.35	800 °C–1100 °C 0.01 s^{-1}–10 s^{-1}	DRX	5.7865×10^{23}	11.804	432.39	[51]
CrCoNi	0.0035746	0.40	800 °C–1100 °C 0.01 s^{-1}–10 s^{-1}	DRX	1.9657×10^{24}	11.3282	450.591	[51]
CrCoNi	0.003460	0.45	800 °C–1100 °C 0.01 s^{-1}–10 s^{-1}	DRX	2.1705×10^{24}	11.060	459.34	[51]
CrCoNi	0.003361	0.50	800 °C–1100 °C 0.01 s^{-1}–10 s^{-1}	DRX	3.3938×10^{24}	10.742	468.79	[51]
CrCoNi	0.003288	0.55	800 °C–1100 °C 0.01 s^{-1}–10 s^{-1}	DRX	5.7543×10^{24}	10.398	477.86	[51]
CrCoNi	0.003212	0.60	800 °C–1100 °C 0.01 s^{-1}–10 s^{-1}	DRX	3.1110×10^{24}	10.019	478.25	[51]
$(CoCrNi)_{94}Ti_3Al_3$	0.0043585	1.0	850 °C–1000 °C 0.001 s^{-1}–1 s^{-1}	DRX	2.9779×10^{15}	5.456	401.080	[52]
$Ni_2Co_1Fe_1V_{0.5}Mo_{0.2}$		0.7	700 °C–800 °C 0.001 s^{-1}–1 s^{-1}	DRV/DRX		3.1	456.300	[46]

standard deviation (S.D.) shown in Eqs. (25)–(29). Each statistical technique relatively determines the predictive capability, stability, and reliability of a model.

The accuracy of a model increases as the R-value approaches 1 and RE, RMSE, AARE, error, and S.D. values approach 0. The Mi, Ai, N, M, and A represent the predicted flow stress values, experimental values, number for the training data, average predicted flow stress values, and average actual flow stress values, respectively.

$$R = \frac{\sum_{i=1}^{n}(A_i - \underline{A})(M_i - \underline{M})}{\sqrt{\sum_{i=1}^{n}(M_i - \underline{M})^2 \sum_{i=1}^{n}(A_i - \underline{A})^2}} \tag{25}$$

$$RMSE = \sqrt{\frac{\sum_{i=1}^{n}|M_i - A_i|^2}{N}} \tag{26}$$

$$AARE(\%) = \frac{1}{n}\sum_{i=1}^{n}\left|\frac{M_i - A_i}{A_i}\right| \times 100\% \tag{27}$$

$$RE(\%) = \left|\frac{M_i - A_i}{A_i}\right| \times 100\% \tag{28}$$

$$S.D. = \sqrt{\frac{N\sum x^2 - (\sum x)^2}{N(N-1)}} \tag{29}$$

By using the alternative hyperbolic constitutive equation in Eq. (8) for MEAs, stating that the ασ value is essential in determining the suitability of the alloy for low or high stresses. Values of $\alpha\sigma < 0.8$ indicate low stress, and values of $\boldsymbol{\alpha\sigma}>1.2$ indicate high stress. The MEAs studied by Wang et al. [51] calculated the activation energy to be 450.59 kJ/mol from the obtained values of n_1, β, and α for CrCoNi with dynamic recrystallization as the dominant deformation mechanism. The research considered the effect of varying strain on the strain hardening exponent (n) and activation energy (Q). Increasing strain is accompanied by decreasing n value and increasing Q values. The research also concludes that the flow stress of the MEA is strain-rate sensitive. After obtaining the values for α, n, Q, and A, there is a need to account for the strain dependence, which is achieved through a six-order polynomial line fitting technique.

Although the polynomial fitting technique helps the model imitatively predict alloys' hot deformation behavior, the conventionally utilized Zener Holloman's parameter neglects the effect of strain on stress, creating a deviation between the predicted and experimental behavior. Zener Holloman's parameter is modified into Eq. (30) to accommodate this variation. Other modifications that accommodate the temperature-dependent elastic modulus (E) and diffusion coefficient (D) can also be employed, resulting in Eq. (31). In Eq. (31), α′ and B are the modified stress multiplier and the hyperbolic sine constant. These modifications have not been employed yet in MEAs. The Q-values for CrCoNi ranged from 348 to 478 kJ/mol, and the n-values ranged from 10 to 14.6 in Wang et al. [9] research. In comparison, Yi et al. [52] reported the Q-values of CoCrNi and $(CoCrNi)_{94}Ti_3Al_3$ as 401 kJ/mol and 566 kJ/mol. The R-squared value for $(CoCrNi)_{94}Ti_3Al_3$ was 0.981, which shows an acceptable level of accuracy.

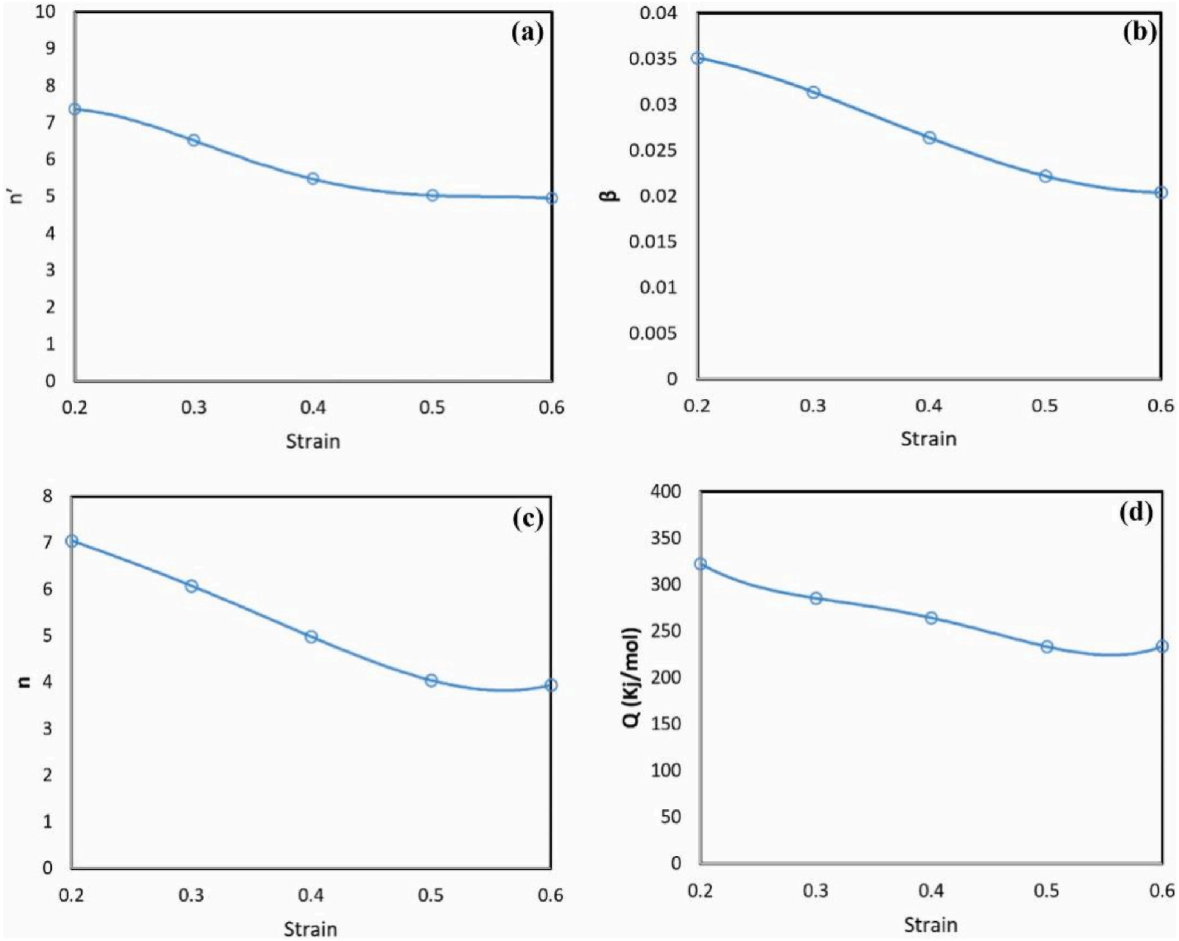

Fig. 21. The strain-dependent relationship for n', β, n, and Q for the hot deformation of CrCoNi [94]. Culled with permission from Elsevier.

$$Z = \dot{e}exp\ \ exp\left(\frac{Q}{R(T+10)}\right) = \dot{\varepsilon}^{4/3}\ exp\left(\frac{Q}{R(T+10)}\right) \tag{30}$$

$$\dot{e}\ \Big/\ D_{(T)} = B\left[sinh\ \ sinh\left(\alpha^{'}\sigma/E_{(T)}\right)\right]^{5} \tag{31}$$

The acceptable levels of accuracy imply that varying values of Q and n can be obtained typically true considering the CoCrNi alloy, making the analysis sometimes unreliable. The values for self-diffusion activation of Co, Cr, and Ni are 228.5, 441.9, and 276.7 kJ/mol, respectively. The mean self-diffusion of the MEA is 315 kJ/mol, which is substantially lower than the lowest experimental value obtained for the alloy. To account for this discrepancy, the variation was attributed to the microstructural attributes of the alloy [93,94]. To account for the differences and improve the model's reliability, the threshold stress (σ_{th}) and predefined stress exponents (n) can be included in defining Zener Holloman's parameter modification in Eqs. (32) and (33).

$$Z = A^{'}(\sigma - \sigma_{th})^{n^{'}} \tag{32}$$

$$lnZ = ln\ A^{'} + n^{'}\ ln\ \ ln\ (\sigma - \sigma_{th}) = lnA + nln\{sinh\{\alpha(\sigma - \sigma_{th})\}\} \tag{33}$$

The six-order polynomial shown in Eq. (34) is for strain compensation in the Arrhenius model. The polynomial function shown in Fig. 21 shows a relationship between the material constant and strain for CrCoNi. The flow stress (σ) for a given strain value (ε) can be expressed in Eq. (35). By using this technique, the reliability of the Arrhenius model is hence improved to predict the flow stress at any temperature and strain rate for the considered Zener-Holloman's parameter.

$$\begin{Bmatrix} \alpha = \alpha_0 + \alpha_1\varepsilon + \alpha_2\varepsilon^2 + \alpha_3\varepsilon^3 + \alpha_4\varepsilon^4 + \alpha_5\varepsilon^5 + \alpha_6\varepsilon^6 & Q = Q_0 + Q_1\varepsilon + Q_2\varepsilon^2 + Q_3\varepsilon^3 + Q_4\varepsilon^4 + Q_5\varepsilon^5 + Q_6\varepsilon^6 \\ n = n + n\varepsilon + n\varepsilon^2 + n_3\varepsilon^3 + n_4\varepsilon^4 + n_5\varepsilon^5 + n_6\varepsilon^6 & ln\ \ ln\ A = A_0 + A_1\varepsilon + A_2\varepsilon^2 + A_3\varepsilon^3 + A_4\varepsilon^4 + A_5\varepsilon^5 + A_6\varepsilon^6 \end{Bmatrix} = \begin{Bmatrix} \alpha = \alpha(\varepsilon) = (\alpha_0 + \alpha_1\varepsilon + \alpha_2\varepsilon^2 + \alpha_3\varepsilon^3 + \alpha_4\varepsilon^4 + \alpha_5\varepsilon^5 + \alpha_6\varepsilon^6) & Q = Q(\varepsilon) = Q_0 + Q_1\varepsilon \\ n = b(\varepsilon) = b_o\ exp\ (\varepsilon/b_1) + b_2 & ln\ \ ln\ A = \ A(\varepsilon) = A_0 + A_1\varepsilon \end{Bmatrix} \tag{34}$$

$$\sigma = \frac{1}{\alpha}\left\{sin\ h^{-1}\left(\frac{Z}{A}\right)^{1/n}\right\} = \frac{1}{\alpha}ln\ \ ln\left\{\left(\frac{Z}{A}\right)^{1/n} + \left[\left(\frac{Z}{A}\right)^{2/n} + 1\right]^{1/2}\right\} \tag{35}$$

6.3. Further discussions

The novelty of modeling the hot deformation behavior of MEAs has only attracted the attention of a few researchers who have only used the Arrhenius model in predicting the hot deformation behavior. However, it is believed that models such as the Artificial Neural Network (ANN), Zerilli-Armstrong (ZA), Johnson-Cook (JC), and DRV/DRX can be utilized in predicting the hot deformation behavior of MEAs. Each model has pros and cons depending on the accuracy, predictability, reliability, and amount of training data.

The ANN model shows very high reliability compared to other models because it works in the similitude of the human brain and requires a large amount of basic processing or training data to produce reliable results. The large amount of training data required to train the model is to determine the accurate relationship between input and output data. The utilization of ANN models for MEA might take longer to achieve because of the large amount of training data required to ensure its proper functionality. There are three parts to any ANN model: the input, hidden, and output. The input and output are easily understood; however, the hidden part is referred to as a black box that does not rely on a specific relationship between the output and input data for improved accuracy. The general formula for the ANN model is shown in Eq. (36), where w, n, and b are the weight parameter, number of input nodes, and bios, respectively. The w and activation functions k and j (neuron functions) are vital for the model [53,89].

$$net = \left(\sum_{i=1}^{n} w_{kj}x_j\right) + b \tag{36}$$

Developing the Zerilli-Armstrong model for MEAs will favor modeling high-strain rates and low-temperature deformation behavior [95–98]. The constitutive equation works better in modeling the flow stress for crystalline metals. The flow stress is determined using Eq. (37), simplified using Eq. (38), and modified using Eqs. (39)–(41). In Eqs. (37)–(41), $\boldsymbol{\varepsilon}$, σ, and T* represent the strain rate, the flow stress, and the homologous temperature, while n, C_1, C_2, C_3, C_4, C_5, and C_6 represent the materials constants. Also, S_1 and I_1 represent the slope and intercept of a plot between lnσ and T*, while parameters such as n_1, B_{01}, n_2, B_{02} are obtained from the plots of the ZA model [95].

$$\sigma = c_0 + B_0\varepsilon^n\ exp\ \ exp\ (-\beta_0 T + \beta_1 Tln\dot{\varepsilon}) \tag{37}$$

$$ln\ \ ln\ \sigma = (ln\ B_0 - 0.00344T) + nln\varepsilon \tag{38}$$

$$\sigma = B_0\left(\varepsilon\ /\ \varepsilon_p\right) + B_0\varepsilon^n\ exp\ (-\beta_0 T + \beta_1 Tln\dot{\varepsilon}) \tag{39}$$

$$\sigma = (C_1 + C_2\varepsilon^n)exp\ (\ -(C_3 + C_4\varepsilon)T^* + (C_5 + C_6T^*)ln\dot{\varepsilon}) \tag{40}$$

$$\{\sigma = (C_1 + C_2\varepsilon^n)exp\ (\ -(C_3 + C_4\varepsilon)T^*\ I_1 = ln(C_1 + C_2\varepsilon^n)\ \ S_1 = -(C_3 + C_4\varepsilon)\ ln\ \sigma = ln(C_1 + C_2\varepsilon^n)exp\ (-(C_3 + C_4\varepsilon)T^* + (C_5 + C_6T^*)ln\dot{\varepsilon})\ S_2 = C_5 + C_6T^* \tag{41}$$

DRV/DRX models have a futuristic applicability for predicting the hot deformation behavior of MEAs. The model is designed to accommodate the three stages of deformation, which are the flow stress, strain hardening, and softening stages. The first stage uses Eqs. (42)–(44) until a peak stress value is obtained. A non-linear portion follows this up to the beginning of the second stage, modeled with Eq. (43). The non-linear portion in the second stage has many complications associated with it, but the linear portion is modeled using Eqs. (45) and (46), while the non-linear portion of the model is predicted using Eqs. (47)–(52) [96]. The notations σ_s, σ_p, ε_s, and ε_p represent steady-state stress, peak-point stress, steady-state strain, and peak-point strain, respectively.

$$\frac{\sigma}{\sigma_p} = \left[\left(\frac{\varepsilon}{\varepsilon_p}\right)exp\ \ exp\left(1 - \frac{\varepsilon}{\varepsilon_p}\right)\right]^{C_1} \tag{42}$$

$$ln\ \ ln\left(\frac{\sigma}{\sigma_p}\right) = C_1\left[ln\ \ ln\left(\frac{\varepsilon}{\varepsilon_p}\right) + \left(1 - \frac{\varepsilon}{\varepsilon_p}\right)\right] \tag{43}$$

$$C_1 = a_5 + b_5 + c_5\ ln\ \ ln\ \dot{\varepsilon} \tag{44}$$

$$b_5 = \frac{\partial C_1}{\partial T}\ ;\ c_5 = \frac{\partial C_1}{\dot{\varepsilon}} \tag{45}$$

$$\sigma = \sigma_p - k\left(\varepsilon - \varepsilon_p\right) \tag{46}$$

$$k = -\ \ a_6 e^{b6T}\dot{\varepsilon}^{c6} \tag{47}$$

$$b_6 = \frac{\partial ln\ \ ln\ (-k)}{\partial T}\ ;\ c_5 = \frac{\partial ln\ \ ln\ k}{\dot{\varepsilon}} \tag{48}$$

$$\sigma = \sigma_s + (\varepsilon_p - \varepsilon_s) exp\left[C_2\left(\varepsilon\left(\varepsilon - \frac{\varepsilon_p}{2} - \frac{\varepsilon^2}{\varepsilon_p}\right)\right)\right] \quad (49)$$

$$ln\ ln\left[\frac{\sigma - \sigma_s}{\sigma_p - \sigma_s}\right] = C_2\left(\varepsilon - \frac{\varepsilon_p}{2} - \frac{\varepsilon^2}{2\varepsilon_p}\right) \quad (50)$$

$$C_2 = a_7 + exp\ (b_7 T) + \dot{\varepsilon}^{c7} \quad (51)$$

$$b_7 = \frac{\partial ln C_2}{\partial T}\ ;\ c_7 = \frac{\partial ln C_2}{\dot{\varepsilon}} \quad (52)$$

Also, the Johnson-Cook model can be applied to model the hot deformation behavior of MEAs at high strain rates. The model is represented in Eqs. (53) and (54), with the modified form in Eq. (55). The variables $\boldsymbol{\sigma}$, n, $\boldsymbol{\varepsilon}$, $\boldsymbol{\dot{\varepsilon}}$, and $\boldsymbol{\varepsilon}_o$ refer to the flow stress, strain hardening exponent, strain, strain rate, and reference strain rate, respectively. The constants A, B, and C represent the strain-hardening behavior of the alloy; A, B, and C represent the yield stress, increased strength resulting from strain hardening, and the strain rate sensitivity, while $C1$and $C2$ parameters account for strain dependence of the alloy. MATLAB capabilities would be employed to minimize the error in curve fitting. Note that even with the curve-fitting capabilities of MATLAB, it is difficult to model the beginning portion of the model and cannot capture strain state sensitivity [97,98].

$$\sigma = (A + B\varepsilon^n)(1 + Cln\ (\dot{\varepsilon} / \dot{\varepsilon}_o) \quad (53)$$

$$\sigma = (A + B\varepsilon^n)((1 + Cln\ (\dot{\varepsilon} / \dot{\varepsilon}_o))(1 - \{(T - T_{room}) / (T_{melt} - T_{room})\}^m) \quad (54)$$

$$\sigma = (A + B\varepsilon^n)\left(1 + C_1\ ln(\dot{\varepsilon} / \dot{\varepsilon}_o) + C_2\ ln\ (\dot{\varepsilon}/\dot{\varepsilon}_o)^2\right)\left(1 - \{(T - T_{room}) / (T_{melt} - T_{room})\}^m\right) \quad (55)$$

Finally, microstructure evolution modeling is a great modeling technique that can find application in modeling the hot deformation behavior of MEAs. The model utilizes specialized techniques such as finite element techniques, crystal plastic mechanics, cellular automata, Monte Carlo, phase field, molecular dynamics, and quantum mechanics. These techniques are constantly being improved to ensure enhanced reliability. Although these techniques are relatively new, coupled with the novel nature of modeling MEAs, the utilization might take longer. The subsequent section delves into novel modeling approaches for predicting flow stress under varied deformation conditions.

7. Machine learning models

In the field of materials engineering, the application of machine learning (ML) techniques has substantially enhanced the forecasting of flow curves across various hot working conditions. Fig. 22 provides a schematic representation of ML constitutive modeling. When employing ML for predicting flow stress, experimental data from hot deformation experiments is randomly divided into training (80%) and testing (20%) groups. The ML model's predictive capability is developed by training it to recognize patterns between the input and output data, with the testing data validating the model's accuracy. The input data encompasses deformation temperature, strain rate, and strain, enabling the ML model to capture the intricate interactions between these variables in the hot deformation of materials, ensuring accuracy and applicability to new data [99].

To enhance material processing conditions and develop methodologies that produce desired outcomes, the utilization of machine learning (ML) models is imperative. Widely used ML techniques, including Generalized Regression Neural Network (GRNN), Artificial Neural Network (ANN), Support Vector Regression (SVR), and Random Forest (RF), are employed to predict flow stress under diverse processing parameters. Accurate predictions of material parameters, such as flow stress, are crucial for process design and optimization, and well-trained machine learning models play a pivotal role in providing these essential insights.

7.1. Support Vector Regression (SVR)

Support Vector Regression (SVR) is a supervised learning approach for regression problems. The objective is to determine a function that maximizes the margin and fits the data effectively using Eqs. (56)–(60). SVR aims to find the ideal weights and bias to reduce error while respecting the ε-insensitive tube limitations. Errors within this range are ignored thanks to the ε-insensitive tube, which allows for tolerance around expected values. Using this tube to fit the data and maximize the margin, SVR aims to produce precise regression predictions [99,100].

$$\frac{1}{2}\|\omega\|^2 + C\sum_{i=1}^{N}(\xi_i + \xi_i^*)\Big) \quad (56)$$

$$y_i - \omega x_i - b \le \varepsilon + \xi_i \quad (57)$$

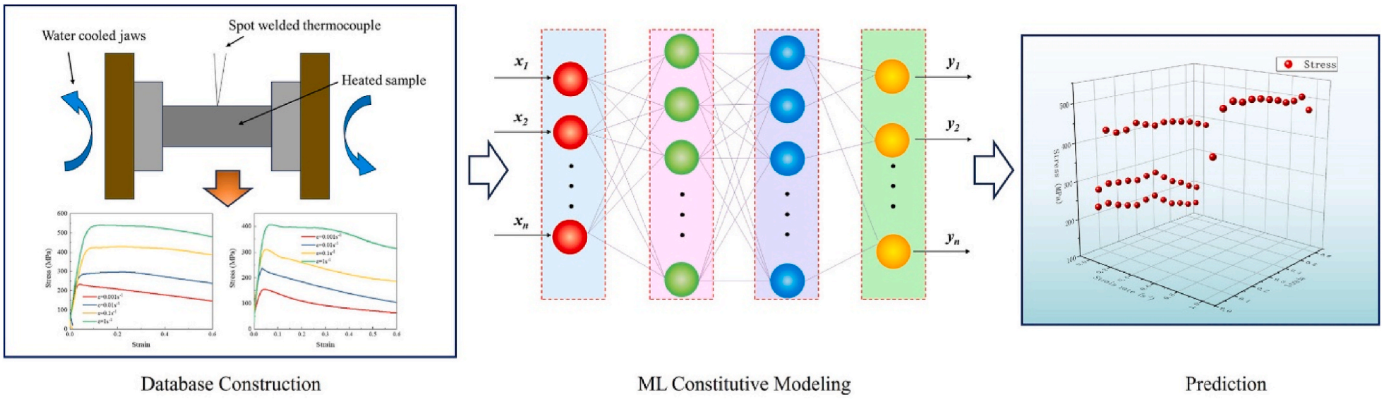

Fig. 22. Schematic of Machine Learning Models [99]. Culled with permission from Elsevier.

$$\omega x_i + b - y_i \leq \varepsilon + \xi_i^* \tag{58}$$

$$\xi_i + \xi_i^* \geq 0 \, for \, i = 1, \ldots, N \tag{59}$$

$$f(x) = \omega . x + b \tag{60}$$

where N represents number of samples and features, x_i represents the i_{th} feature vector and y_i represents the target value for the i_{th} sample, the goal is to find the function *f(x)* that predicts the continuous target *y*, *w* represents weights associated with features, *b* represents the bias term, ξ_i, ξ_i^* represent slack variable, ε represents insensitive tube, and C represents regularization parameter controlling the trade-off between maximizing the margin and minimizing the errors.

7.2. The artificial neural network (ANN) model

There are two main classifications of ANN models – feed-backward neural networks and feed-forward neural networks. The feed-forward neural network is categorized into single-layer perception, multi-layer perception, and radial basis function network, while the feed-backward is categorized into Kohonen's self-organizing map (SOM), Hopfield network, Bayesian Regularized neural network (BRANN), Competitive networks, and art models [101]. However, the back-propagation artificial neural network (BP-ANN) approach is the most widely used artificial neural network (ANN) model. The model replicates the functioning of the human brain by acting as a highly linked processing unit for detailed data analysis [102]. Because of its exceptional self-adaptive and self-learning qualities, the BP neural network has become a potent analytical tool for simulating the hot deformation behavior of metallic materials in recent years. The BP neural network model is especially well-suited for issues where the input-output interactions are uncertain, as it generally consists of input, hidden, and output layers. It can predict unknown values by efficiently learning from big datasets without making assumptions about predetermined connections [53,103].

Artificial Neural Network (ANN) models use backpropagation techniques to modify internal parameters throughout the training phase iteratively represented in Eqs. (61)–(63). This repeated modification aims to reduce prediction mistakes and increase prediction accuracy overall. Because of this training, ANN models show they can generalize well, making precise predictions for data examples that have not yet been observed. This adaptability highlights the usefulness of ANN models in various contexts [99].

$$z_j = \varnothing\left(\sum_{i=1}^{N} \omega_{ij}^{(1)} x_i + b_j^{(1)}\right) \tag{61}$$

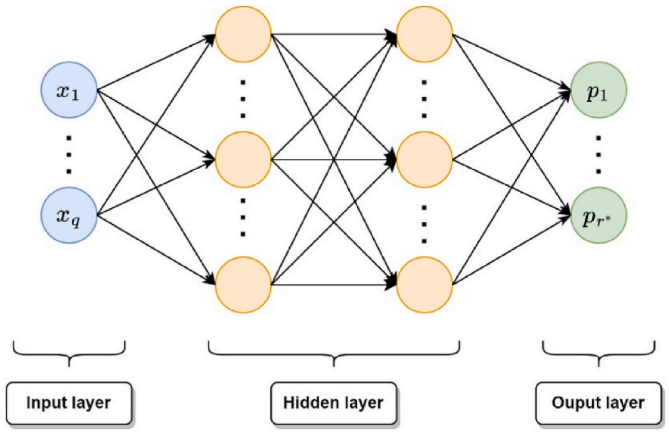

Fig. 23. Schematic of the ANN model [104]. Culled with permission from Elsevier.

$$y_k = \varnothing\left(\sum_{j=1}^{M} \omega_{kj}^{(2)} z_j + b_k^{(2)}\right) \tag{62}$$

$$\hat{y}_k = g(y_k) \tag{63}$$

where z_j represents the output of j_{th} node in the hidden layer; $\omega_{ij}^{(1)}$ represents the weight between the i_{th} input and j_{th} hidden node; $b_j^{(1)}$ represents the bias for the j_{th} hidden node, y_k represents the output of k_{th} node in the hidden layer; $\omega_{kj}^{(2)}$ denotes the weight between the j_{th} input and k_{th} hidden node; $b_k^{(2)}$ represents the bias for the k_{th} hidden node.

In ANN models, there are simple models, such as the deep neural network (DNN) [104], shown in Fig. 23, and more complex ones [105]. In general, three layers make up a DNN: input, hidden, and output layers, while complex ANN models such as neural network potential (Version 2) are used by [105] for the deformation of CrCoNi MEA trained using density functional theory (DFT). The collinear spin-polarized DFT calculations performed on the Vienna Ab initio Simulation Package (VASP) for the CrCoNi MEA were developed using the n2p2 algorithm, which was made possible via the Large-scale Atomic/Molecular Massively Parallel Simulator (LAMMPS) interface built into n2p2. Non-collinear spin configurations were considered; however, it was shown that they had little effect on the chemical ordering tendency.

7.3. Generalized Regression Neural Network (GRNN)

A commonly employed neural network for regression tasks is the Generalized Regression Neural Network (GRNN), specifically designed for predicting continuous numerical values. It operates as a radial basis function network, comprising four layers: the input layer representing input features, the pattern layer employing radial basis functions (typically Gaussian kernels) to compute distances between input data and stored patterns using Eq. (64), the summation layer that aggregates distances for each pattern, and the output layer generating the regression result. GRNN utilizes radial basis functions to determine activations in the pattern layer when presented with a new input. The ultimate regression output is formed by combining these activations in the summation layer and processing them through the output layer [98, 106–109].

$$\varnothing_i(x) = \left(-\frac{\|x - \mu_i\|^2}{2\sigma_i^2}\right) \tag{64}$$

where μ_i represents the mean vector of the i_{th} pattern, and σ_i represents the spread parameter.

7.4. Random Forest (RF)

The Random Forest (RF) ensemble learning technique is primarily designed to address regression challenges. In its training phase, RF creates numerous decision trees and subsequently averages the predictions from each tree. Each decision tree within the forest is constructed independently, utilizing a subset of attributes and samples to forecast a numerical outcome. The strength of RF lies in its ability to mitigate overfitting, noise, and outliers due to the combination of multiple trees and the randomization in feature selection and sample bootstrapping [99,110].

Qiao and Zhu [53] investigated the hot deformation characteristics of AlCrFeNi MEA using ML techniques to comprehend the intricate relationship between flow stress and hot deformation behavior. They developed two constitutive models employing Artificial Neural Networks ANN and SVM. The standard structures of ANN and SVM algorithms, as illustrated in Fig. 24, were trained to identify inherent correlations in the experimental training data between input variables

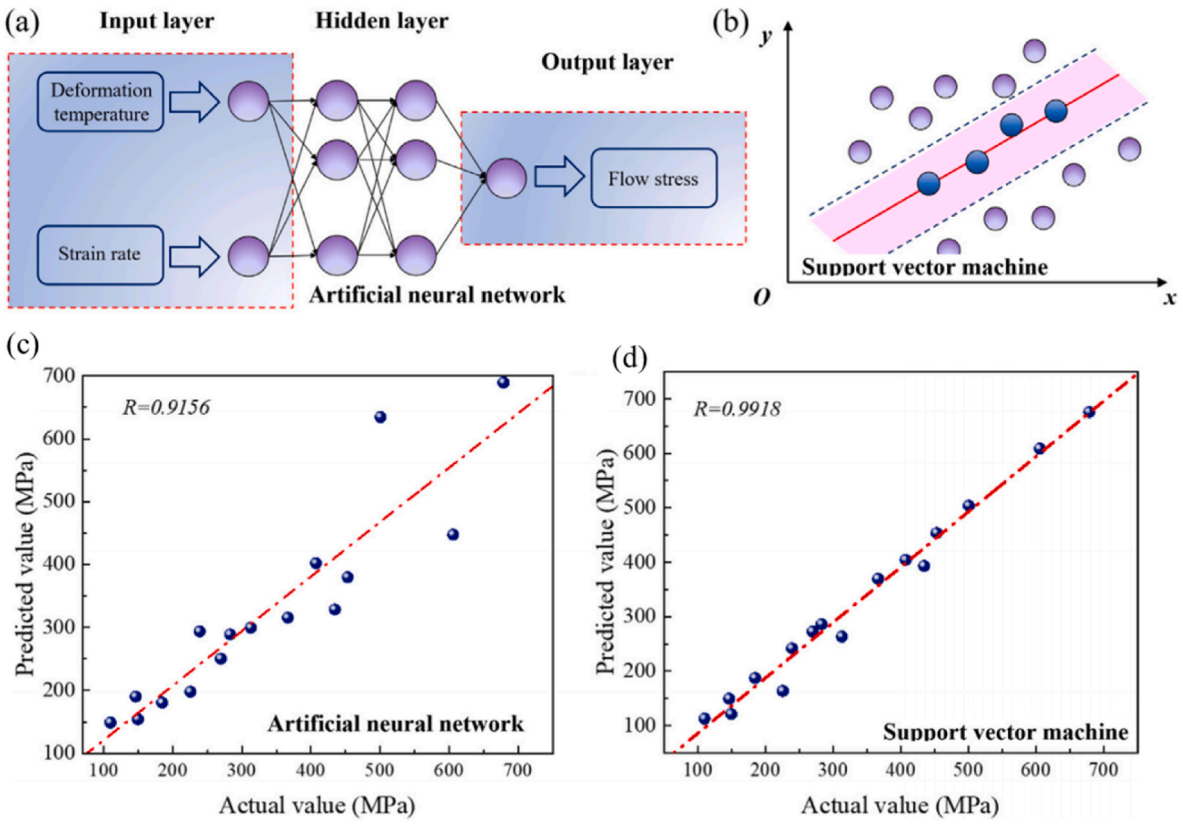

Fig. 24. Schematics and regression analysis of ANN and SVM for AlCrFeNi MEA [53]. Culled with permission from Elsevier.

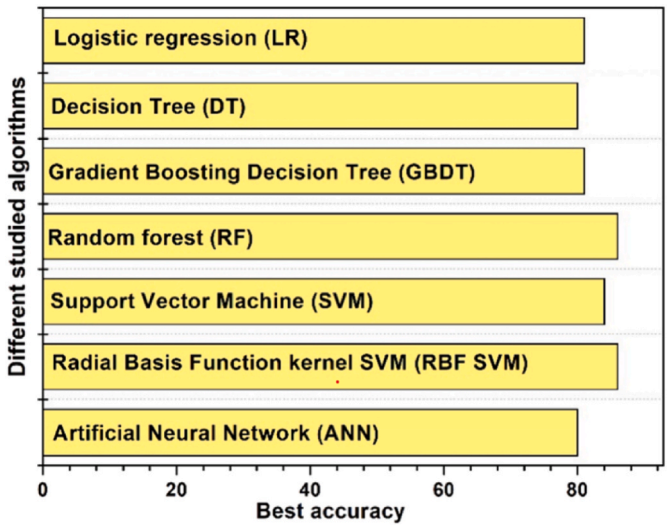

Fig. 25. The accuracy of various machine learning (ML) [111]. Culled with permission from Elsevier.

(the logarithms of strain rate and deformation temperature) and the output variable (flow stress). Prior to the training process, the input and output variables were scaled within the range of 0–1 to ensure uniformity among variables. Normalizing these variables is crucial for maintaining consistency within the same range. The normalization equation is shown in Eq. (65).

$$X' = \frac{X - 0.95X_{min}}{1.05X_{max} - 0.95X_{min}} \tag{65}$$

where X represents the actual experimental data, $X_{\min}$ and $X_{\max}$ represent the minimum and maximum value of X, respectively, and X' represents the normalized value of the X.

For more accuracy, the backpropagation (BP-ANN) technique was applied, and the Bayesian regularization algorithm was used to improve generalization capacity further. To reduce errors and eventually provide the desired result, the procedure entails continuously adjusting the weights and thresholds of networks. Using an iterative process guarantees that suitable parameters are chosen for optimal model performance. From Fig. 24, the SVM model exhibits good agreement between experimental and projected flow stress values, with little dispersion. However, the ANN model has a divergence from the asymptote in the distribution of data points. In quantitative terms, better training success is usually indicated by higher R values (almost 1) and lower $AARE$ values. The values of R and $AARE$ for the ANN model are 0.9156 and 0.5531%, respectively, whereas those for the SVM model are 0.9918 and 0.4531%. This comparison demonstrates how well the SVM model predicts the hot deformation behavior of AlCrFeNi MEAs under a range of hot operating circumstances by efficiently learning from experimental data. To support the claim of Qiao and Zhu [53], Dewangan et al. [111] showed the accuracy of various machine learning models shown in Fig. 25. From Fig. 25, SVM had higher accuracy than ANN. However, Random Forest (RF) and Radial Basis Function Kernel SVM (RBF SVM) had the highest accuracy.

8. Molecular dynamics

Molecular dynamics (MD) simulation serves as an appropriate approach for examining the evolution of deformation in alloy systems. Researchers have employed MD investigations to explore the underlying mechanisms governing deformation processes, encompassing phenomena such as phase transitions, mechanical properties, compositional influences, effects of defects, and stacking fault energy (SFE). However, utilizing the MD technique poses challenges due to limitations in

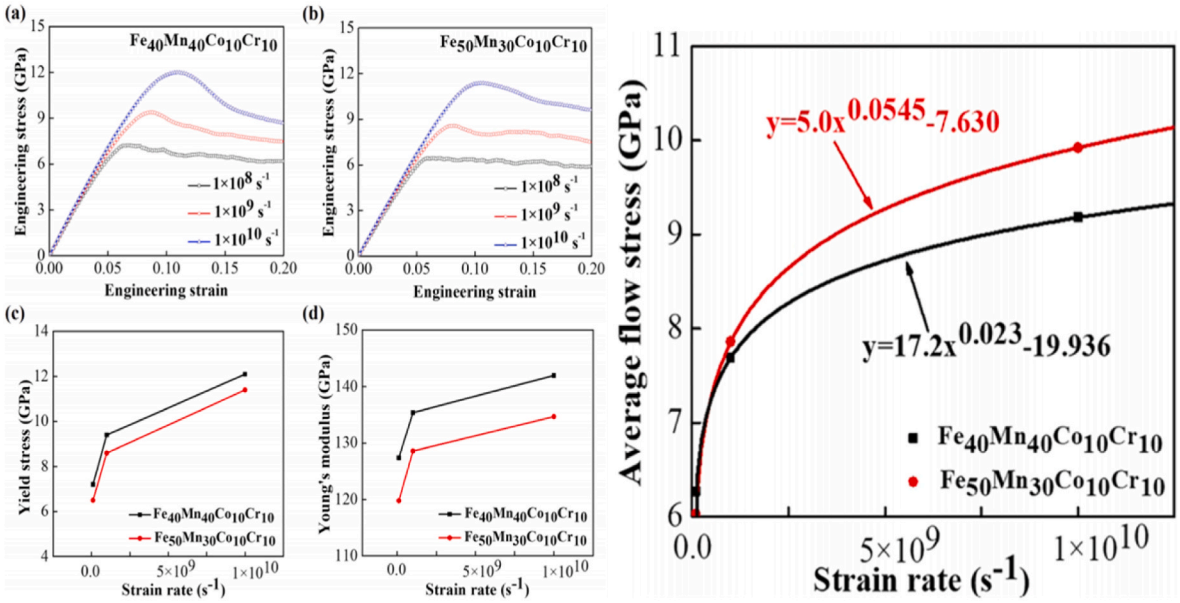

Fig. 26. Stress-strain curves and average flow stress for $Fe_{80-x}Mn_xCo_{10}Cr_{10}$ (x = 30, 40) at different strain rates [113]. Culled with permission from Elsevier.

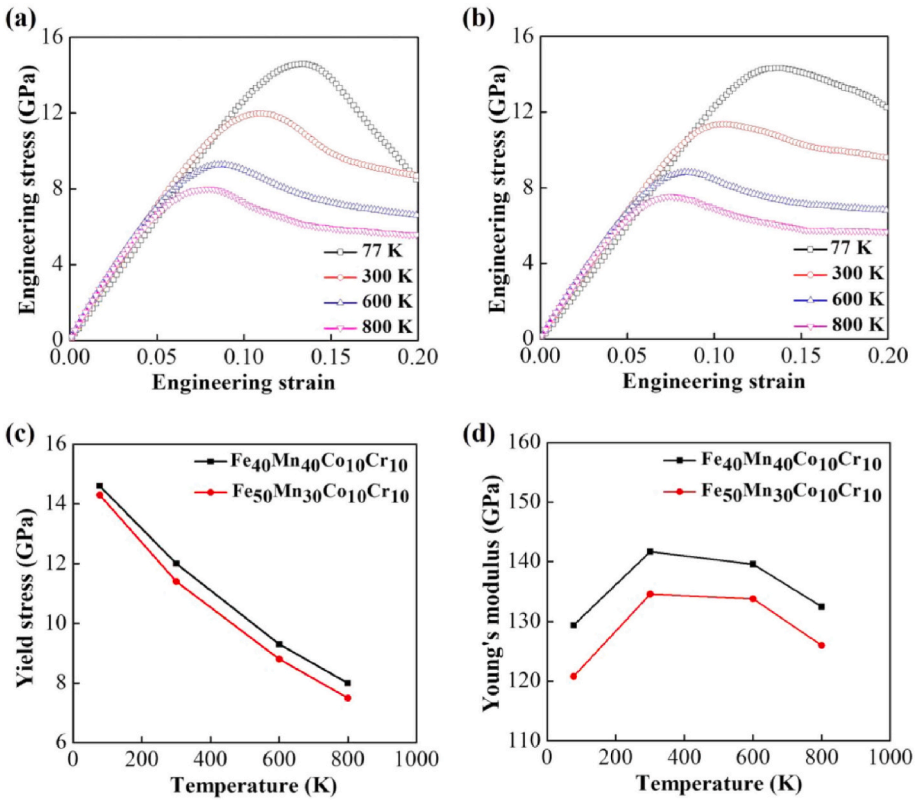

Fig. 27. Stress-strain curves for $Fe_{80-x}Mn_xCo_{10}Cr_{10}$ (x = 30, 40) at different temperatures [113]. Culled with permission from Elsevier.

describing potential fields for multi-component compositions [112].

However, Pan et al. [113] utilized Special Quasirandom Structures (SQS) to provide the seed for creating MEA models with an atomically disorganized arrangement and constructed the polycrystalline structure using the Voronoi method. The research examined the deformation in $Fe_{80-x}Mn_xCo_{10}Cr_{10}$ alloy systems using a 200 × 200 × 200 Å 3D polycrystalline model containing around 685,900 atoms. The polycrystalline MEA exhibits random crystallographic orientations and is characterized by a spherical grain model with an average grain size varying from 3.9 nm to 19.7 nm. To simulate the plastic deformation behavior of $Fe_{80-x}Mn_xCo_{10}Cr_{10}$ MEA during uniaxial stretching, a second closest neighbor modified embedded-atom method (2NN MEAM) interatomic potential was employed. The lattice constants, melting points, as well as the cohesive energies were utilized to confirm the validity of the interatomic interaction potentials employed, and they demonstrated consistency with other sources. Periodic boundary conditions were used to reduce border effects.

The researchers examined how the strain rate influences the me-

chanical properties and microstructure of $Fe_{80-x}Mn_xCo_{10}Cr_{10}$ (x = 30, 40) MEAs subjected to deformation at 300 K under varying strain rates. Additionally, atomic-scale uniaxial stretching was applied to $Fe_{80-x}Mn_xCo_{10}Cr_{10}$ (x = 30, 40) MEAs at four different temperatures (77 K, 300 K, 600 K, and 800 K). In Fig. 26, it is illustrated that with an increase in the strain rate, there is an elevation in the yield point, followed by a softening phenomenon. This softening could potentially be attributed to shear localization and the presence of high free volume during plastic deformation. The relationship between average flow stress and strain rate is elucidated using a power function connection in Eq. (66). It is noted that at higher strain rates, the amplitude of the average flow stress rise gradually diminishes. The intrinsic relation is in good agreement with the power function, highlighting the materials' sensitivity to strain rate. Understanding and predicting the mechanical characteristics of Fe–Mn–Co–Cr MEAs is made more accessible by these essential insights into the behavior of the materials at different strain rates.

$$\sigma_y = a + b\dot{\varepsilon}^c \tag{66}$$

At a strain rate of 10^{10} s^{-1}, the impact of temperature on the tensile strength of $Fe_{80-x}Mn_xCo_{10}Cr_{10}$ MEAs is examined. As shown in Fig. 27, both MEA models show homologous fluctuations in stress with increasing tensile strain below a strain threshold of 20%. The yield stress and deformation temperature show a clear negative connection in the stress-strain curves, with higher yield stress occurring at lower temperatures during tensile simulation. Following earlier findings, the yield stress for $Fe_{40}Mn_{40}Co_{10}Cr_{10}$ MEA rises from 8 GPa to 14.6 GPa when the temperature drops from 800 K to 77 K. Martensite production during cryogenic deformation might explain the temperature-dependent fluctuation in flow stress, as lower temperatures are often associated with lower stacking fault energy (SFE). By inhibiting dislocation climb and cross-slip, a decrease in SFE raises the average flow stress, concentrating stress and causing twinning coordination for deformation.

Nevertheless, both $Fe_{40}Mn_{40}Co_{10}Cr_{10}$ and $Fe_{50}Mn_{30}Co_{10}Cr_{10}$ MEAs show substantially smaller Young's moduli at 77 K than at 300 K, which is consistent with experimental findings. Increased GB activity in the distribution of shear strain provides evidence that this drop in elastic modulus at 77 K may be due to grain boundary sliding or rotation. These results shed light on how temperature affects the tensile characteristics and microstructural development of Fe–Mn–Co–Cr MEAs and give insights into temperature-dependent mechanical behavior.

Also, Zhang et al. [114] conducted a study on how temperature affects the elastic modulus of CoCrNi MEA, assessed through elastic constant computations. At a constant grain size, the material demonstrates a higher elastic modulus at lower temperatures. In Fig. 28, simple tension tests were performed on all models at 77, 200, 300, and 600 K to investigate the influence of temperature on the mechanical properties of CoCrNi MEA. For each model, a decrease in temperature results in an increase in both the material's yield strength and maximum flow stress. Plastic deformation in the materials is primarily governed by grain boundary slips and dislocation slips. When the grain size is below the critical grain size of 15.2 nm, grain boundary slips become the dominant factor influencing plastic deformation. Earlier research has indicated that the heat activation process of materials can impact the movement of grain boundaries.

8.1. First-principles

Density functional theory (DFT) is a first-principle theoretical tool within statistical mechanics, providing a foundational framework for the contemporary description of thermodynamic and transport properties in systems consisting of three or more actual or virtual quantum or classical particles [115]. Tang et al. [116] utilized DFT to assess the deformation response of $Fe_{33.3}Cr_{33.3}Ni_{33.3}$. The study employed a spin-polarized electronic structure scheme, the Projector Augmented Wave (PAW) approach, and DFT within the Vienna Ab-initio Simulation Package (VASP) for the calculation of elastic constants. The Perdew-Burke-Ernzerhof parametrization-treated generalized gradient approximation (GGA) was applied for the electron exchange-correlation function. In the calculations for Cr, Fe, and Ni, semi-core electrons were excluded, and specific core topologies were considered. The majority of the computations utilized a 400 eV plane wave cut-off energy to ensure the convergence of force and total energy components. Monkhorst-Pack

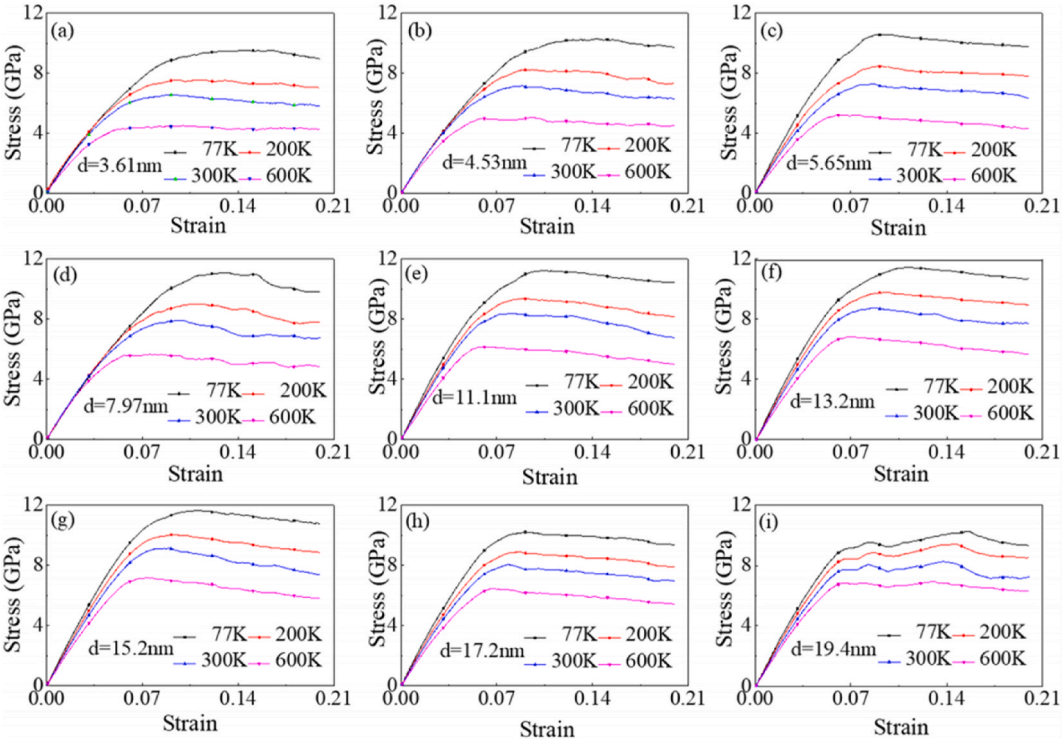

Fig. 28. The curves of the simple tension stress–strain versus grain size for CoCrNi MEA at various temperatures [114]. Culled with permission from Elsevier.

meshes with different k-point configurations, such as 4 × 4 × 4 and 6 × 6 × 6 meshes, were used for the elastic constant computations.

An innovative DFT method was used for disordered alloys, combining exchange Monte Carlo (MC) simulations with a first-principles-designed Cluster Expansion (CE) Hamiltonian. This technique made it possible to examine disorder-order transitions and elastic characteristics while considering chemical Short-Range Order (SRO) effects between various atomic pairs. The theoretical expression of SRO parameters is in Eq. (67). The deformation of unstrained structures was used to derive the elastic constants, and the elastic constant matrix elements were obtained by analyzing changes in total energy. Eq. (68) describes how the deformation affects the crystal's energy. Using well-established techniques, the anisotropy of elastic characteristics, such as Poisson's ratio and Young's modulus, was examined, adding to a thorough comprehension of the mechanical behavior of the FeCrNi system.

$$\alpha_n^{A,B} = 1 - \frac{y_n^{A,B}}{x_A x_B} \tag{67}$$

$$U = \frac{E_{tot} - E_0}{V_0} = \frac{1}{2}\sum_{i=1}^{6}\sum_{j=1}^{6} c_{ij}\varepsilon_i\varepsilon_j \tag{68}$$

where y $y_n^{A,B}$ represents the pair probability, x_A and x_B represent the concentration of A and B atoms, respectively. Segregation and chemical ordering between A and B components are represented as positive and negative $\alpha_n^{A,B}$, respectively. E_0 represents the total energy of the unstrained lattice, V_0 represents the volume of the undistorted cell, and the C_{ij} are the elements of the elastic constant matrix with a notation that follows standard convention. The values of i and j run from 1 to 6.

The accuracy of the DFT calculations was proven to be consistent with the actual. The DFT indicates that the FCC phase in FeCrNi alloy stays stable until it melts. Atomistic arrangements derived from Monte Carlo (MC) simulations conducted at temperatures 300 K and 2000K show a temperature-dependent shift from an ordered to a disordered form. The analysis of SRO characteristics shows chemical interactions between Fe–Cr and Fe–Ni pairings, with more excellent ordering between Fe and Cr. Positive SRO parameters show a repulsive interaction between Cr and Ni. Supercell designs showing the impact of SRO effects show orthorhombic symmetry at 300 K and *Pnnm* symmetry at 2000K for DFT calculations of elastic constants at equiatomic composition. Elastic constants computed using DFT exhibit temperature dependence: larger temperatures result in smaller elastic constants because of increasing disorder. Magnetic moments and predicted lattice constants show considerable structural variations between disordered and ordered systems. The impact of the disorder on elastic characteristics is highlighted by DFT calculations, which consider both relaxed and unrelaxed configurations and demonstrate good agreement with experimental data [116].

In an earlier research by Tang et al. [117], the DFT technique was used for the dislocation density evolution in FeCrNi MEA during deformation. The DFT results demonstrate the critical influence of disorder on chemical ordering by showing that elastic constants are less at high temperatures than in low-temperature configurations. DFT elastic characteristics predicted for disordered configurations at 2000K are in good agreement with experimental observations, suggesting that the FeCrNi alloy samples obtained in the experiments are probably metastable phases that were not subjected to annealing. The observed elastic characteristics have a strong resemblance to the DFT predictions, indicating the lack of the ordered intermetallic phases and SROs anticipated at lower temperatures. The fact that SROs were not formed in the experimental alloys is in line with findings in other alloy systems, where SROs were only discovered following extensive annealing at high temperatures. For example, SROs were found in CrCoNi alloy after 120 h of annealing at 1000 °C.

9. Challenges and prospects of MEA processed by hot deformation processes

One viable approach for achieving microstructural refinement that is both practical and suitable for industrial applications involves the exploitation of dynamic recrystallization (DRX) through hot deformation [118–121]. This overview also presented evidence that the use of DRX for grain refining in MEAs is highly effective. The notable impact of hot working in mitigating the presence of defects has considerable significance; this is particularly relevant for powder metallurgy components, as it aids in lowering the amount of porosity.

It is interesting to note that a few research have been conducted on the use of thermomechanical processing at high temperatures for the purpose of producing superplastic microstructures. Subsequent investigations may direct their attention towards alternative conventional processing techniques in order to achieve enhanced superplasticity at high strain rates.

As previously stated, the DRX process is recognized as a significant mechanism for restoring the microstructure during the hotworking of MEAs. The phenomenon of DRX propagation through the necklace mechanism has been seen in several MEAs. Furthermore, it has been established that as the strain rate decreases and the deformation temperature increases, there is a surge in the grain size of the recrystallized grains and recrystallization percentage [52,56,60,66].

Investigating the influence of the initial microstructure on the hotworking behavior of various MEAs is a topic of significant research interest. Hence, a significant portion of future research should focus on examining the impact of deformation variables, such as the deformation temperature, strain rate, and strain, as well as the influence of different phases on the microstructural development and behavior of dynamic recrystallization. Also, the effect of strain rate on the grain size may not be direct as the diffusion pathways during hot working of MEAs are not straightforward. It was noted from some of the studies reviewed that the influence of strain rate on grain refinement is not consistent. Also, the deformation heating effect at strain rate $>0.01\ s^{-1}$ can influence the anomalous behavior of the microstructures. Hence, further studies should be conducted to understand these anomalies fully. Furthermore, some of the experiments are not fully isothermal. Therefore, further research should also be carried out under this condition.

The majority of the evaluated papers examined the phenomenon of compressive deformation in relation to the flow behavior and the underlying dominant mechanisms. The influence of stress state can be substantial as it varies in compression, torsion tests, and tension. Taking into account the state of stress is crucial in order to attain comprehensive control over the microstructure of a component. Studying how deformation parameters under different forming processes, such as hot-extrusion, hot-rolling, hot forging, and hot torsion, affect the flow behavior and deformation mechanisms of MEAs would be of great scientific interest. The understanding of CDRX and DDRX mechanisms in grain recrystallization is well-established in the literature [48,52,66,71]. However, the comprehension of precipitation-induced DRX, twinning-induced DRX, strain-induced precipitation, and strain-induced grain boundary migration mechanisms in the context of the hot deformation of MEAs remains insufficient. Future research should prioritize investigations that examine the relationship between the mechanisms of deformation and microstructural changes.

Based on the findings derived from the examined literature, it is imperative to construct processing maps to facilitate the use of hot working techniques in MEAs for practical purposes. It should be emphasized that flow softening behavior can occur due to the initiation of cracking and flow instability [51,53,77,86]. Hence, more than the hot-deformation flow curves are required to provide a comprehensive assessment of the hot working behavior of MEAs. Therefore, future research should place major emphasis on the analysis of hot working behavior via processing maps. Furthermore, it is essential to consider the impact of the stress state on the instability zones of the processing map.

The occurrence of cracking in the instability regimes of the processing map may be attributed to the process of hot deformation. Conversely, regions characterized by high power dissipation efficiency may undergo microstructural refinement by dynamic recrystallization, hence mitigating any issues associated with hot-working in these regimes [51,53,77,86].

The novelty of modeling the hot deformation behavior of MEAs has only attracted the attention of a few researchers who have mostly used the Arrhenius model in predicting the hot deformation behavior. It is also noted that ANN stand out as a potent machine learning model for predicting MEA flow stress. While ANN has demonstrated superior accuracy compared to other models, alternative machine learning models, such as Random Forest (RF) and Radial Basis Function Support Vector Machine (RBF SVM), exhibit comparable performance. Notably, there has been limited research on MEA utilizing ANN, indicating its promising potential for future applications. In addition to machine learning, first principles and molecular dynamics are noteworthy techniques employed for predicting the hot deformation of MEA. First principles utilize Density Functional Theory (DFT) calculations to forecast the impact of strain rate and temperature on MEA's hot deformation behavior. Similarly, Molecular Dynamics (MD) simulations leverage atomistic models to gain insights into the high-temperature deformation of MEA. However, the precision of these models has yet to be validated against experimental values, particularly under dynamic loading conditions (high strain rates) and elevated temperatures. Future research in this area should prioritize obtaining more experimental data under extreme conditions to enhance the accuracy and applicability of these predictive models.

A study has been undertaken to examine the hot-deformation characteristics of MEAs produced using additive manufacturing methods. This investigation is motivated by the capability of various additive manufacturing techniques to create intricate and complex structures, as well as the requirement for thermomechanical post-processing treatments in specific cases [43,88]. In the near future, there will be a significant amount of research conducted on these subjects.

The evaluation of flow stress in MEAs is commonly conducted through the utilization of uniaxial compression testing machines such as servo-hydraulic and screw-driven machines. Standard machines like the Gleeble 1500 thermo-mechanical simulator and Instron universal testing machine can conduct tests at strain rates up to 5 s^{-1}, while specialized equipment like the Gleeble 3800 as well as Gleeble 3500 can attain strain rates of around 100 s^{-1}. Nevertheless, these strain rates are significantly lower compared to those found in conventional manufacturing processes such as hot forging [102,118,119]. Hence, in order to tackle this challenge, it is imperative to investigate the potential of finite element simulation as a viable alternative to experimental testing. Also, future research should focus on using finite element software to simulate the deformation data of MEAs under high strain rates, which encompasses a broad spectrum of industrial processing settings.

Declaration of competing interest

The authors declare that they have no known competing financial interests or personal relationships that could have appeared to influence the work reported in this paper.

Acknowledgements

The authors wish to appreciate the support of their respective institutions, and the National Research Foundation (NRF), South Africa through the Grant No: 138062, administered by The University of Johannesburg, South Africa.

References

[1] Cantor B, Chang ITH, Knight P, Vincent AJB. Microstructural development in equiatomic multicomponent alloys. Mater Sci Eng, A 2004;375:213–8. https://doi.org/10.1016/j.msea.2003.10.257.
[2] Yeh JW, Chen SK, Lin SJ, Gan JY, Chin TS, Shun TT, Tsau CH, Chang SY. Nanostructured high-entropy alloys with multiple principal elements: novel alloy design concepts and outcomes. Adv Eng Mater 2004;6(5):299–303. https://doi.org/10.1002/adem.200300567.
[3] Garcia Filho FDC, Ritchie RO, Meyers MA, Monteiro SN. Cantor-derived medium-entropy alloys: bridging the gap between traditional metallic and high-entropy alloys. J Mater Res Technol 2022;17:1868–95. https://doi.org/10.1016/j.jmrt.2022.01.118.
[4] He QF, Ding ZY, Ye YF, Yang Y. Design of high-entropy alloy: a perspective from nonideal mixing. J Occup Med 2017;69:2092–8. https://doi.org/10.1007/s11837-017-2452-1.
[5] Miracle DB, Senkov ON. A critical review of high entropy alloys and related concepts. Acta Mater 2017;122:448–511. https://doi.org/10.1016/j.actamat.2016.08.081.
[6] Zhang W, Liaw PK, Zhang Y. Science and technology in high-entropy alloys. Sci China Mater 2018;61:2–22. https://doi.org/10.1007/s40843-017-9195-8.
[7] Cheng CY, Yang YC, Zhong YZ, Chen YY, Hsu T, Yeh JW. Physical metallurgy of concentrated solid solutions from low-entropy to high-entropy alloys. Curr Opin Solid State Mater Sci 2017;21(6). https://doi.org/10.1016/j.cossms.2017.09.002.
[8] Cui P, Ma Y, Zhang L, Zhang M, Fan J, Dong W, Yu P, Liu R. Effect of Ti on microstructures and mechanical properties of high entropy alloys based on CoFeMnNi system. Mater Sci Eng, A 2018;737:198–204. https://doi.org/10.1016/j.msea.2018.09.050.
[9] Kucza W, Dabrowa J, Cieslak G, Berent K, Kulik T, Danielewski M. Studies of "sluggish diffusion" effect in Co-Cr-Fe-Mn-Ni, Co-Cr-Fe-Ni and Co-Fe-Mn-Ni high entropy alloys; determination of tracer diffusivities by combinatorial approach. J Alloys Compd 2018;731:920–8. https://doi.org/10.1016/j.jallcom.2017.10.108.
[10] Laplanche G, Gadaud P, Barsch C, Demtroder K, Reinhart C, Schreuer J, George EP. Elastic moduli and thermal expansion coefficients of medium-entropy subsystems of the CrMnFeCoNi high-entropy alloy. J Alloys Compd 2018;746:244–55. https://doi.org/10.1016/j.jallcom.2018.02.251.
[11] Ding J, Yu Q, Asta M, Ritchie RO. Tunable stacking fault energies by tailoring local chemical order in CrCoNi medium-entropy alloys. Proc Natl Acad Sci USA 2018;115(36):8919–24. https://doi.org/10.1073/pnas.1808660115.
[12] Zhang R, Zhao S, Ding J, Chong Y, Jia T, Ophus C, Asta M, Ritchie RO, Minor AM. Short-range order and its impact on the CrCoNi medium-entropy alloy. Nature 2020;581(7808):283–7. https://doi.org/10.1038/s41586-020-2275-z.
[13] Zhou YJ, Zhang Y, Wang YL, Chen GL. Solid solution alloys of AlCoCrFeNiTix with excellent room-temperature mechanical properties. Appl Phys Lett 2007;90:181904. https://doi.org/10.1063/1.2734517.
[14] Hsu CY, Juan CC, Wang WR, Sheu TS, Yeh JW, Chen SK. On the superior hot hardness and softening resistance of AlCoCrxFeMo0.5Ni high-entropy alloys. Mater Sci Eng, A 2011;528:3581–8. https://doi.org/10.1016/j.msea.2011.01.072.
[15] Chuang MH, Tsai MH, Wang WR, Lin SJ, Yeh JW. Microstructure and wear behavior of AlxCo1.5CrFeNi1.5Tiy high-entropy alloys. Acta Mater 2011;59:6308–17. https://doi.org/10.1016/j.actamat.2011.06.041.
[16] Lin CM, Tsai HL. Evolution of microstructure, hardness, and corrosion properties of high entropy Al0.5CoCrFeNi alloy. Intermetallics 2011;19:288–94. https://doi.org/10.1016/j.intermet.2010.10.008.
[17] Zhang Y, Zuo TT, Cheng YQ, Liaw Pk. High-entropy alloys with high saturation magnetization, electrical resistivity, and malleability. Sci Rep 2013;3:1455. https://doi.org/10.1038/srep01455.
[18] Zhang Y, Zuo TT, Tang Z, Gao MC, Dahmen KA, Liaw PK, Lu ZP. Microstructures and properties of high-entropy alloys. Prog Mater Sci 2014;61:1–93. https://doi.org/10.1016/j.pmatsci.2013.10.001.
[19] Gludovatz B, Hohenwarter A, Catoor D, Chang EH, George EP, Ritchie RO. A fracture-resistant high-entropy alloy for cryogenic applications. Science 2014;345:1153–8. https://doi.org/10.1126/science.1254581.
[20] Jiang L, Cao ZQ, Jie JC, Zhang JJ, Lu YP, Wang TM, Li TJ. Effect of Mo and Ni elements on microstructure evolution and mechanical properties of the $CoFeNi_xVMo_y$ high entropy alloys. J Alloys Compd 2015;649:585–90. https://doi.org/10.1016/j.jallcom.2015.07.185.
[21] Singh S, Wanderka N, Murty BS, Glatzel U, Banhart J. Decomposition in multi-component AlCoCrCuFeNi high-entropy alloy. Acta Mater 2011;59:182–90. https://doi.org/10.1016/j.actamat.2010.09.023.
[22] Manzoni A, Daoud H, Volkl R, Glatzel U, Wanderka N. Phase separation in equiatomic AlCoCrFeNi high-entropy alloy. Ultramicroscopy 2013;132:212–5. https://doi.org/10.1016/j.ultramic.2012.12.015.
[23] Cheng CY, Yeh JW. High thermal stability of the amorphous structure of GexNbTaTiZr(x = 0.5, 1) high-entropy alloys. Mater Lett 2016;181:223–6. https://doi.org/10.1016/j.matlet.2016.06.040.
[24] Chattopadhyay C, Satish Idury KSN, Bhatt J, Mondal K, Murty BS. Critical evaluation of glass forming ability criteria. J Mater Sci Technol 2016;32:380–400. https://doi.org/10.1179/1743284715Y.0000000104.
[25] Yang X, Zhang Y. Prediction of high-entropy stabilized solid-solution in multi-component alloys. Mater Chem Phys 2012;132:233–8. https://doi.org/10.1016/j.matchemphys.2011.11.021.

[26] Guo S, Hu Q, Ng C, Liu CT. More than entropy in high-entropy alloys: forming solid solutions or amorphous phase. Intermetallics 2013;41:96–103. https://doi.org/10.1016/j.intermet.2013.05.002.

[27] Otto F, Yang Y, Bei H, George EP. Relative effects of enthalpy and entropy on the phase stability of equiatomic high-entropy alloys. Acta Mater 2013;61:2628–38. https://doi.org/10.1016/j.actamat.2013.01.042.

[28] Laurent-Brocq M, Perriere L, Pires R, Champion Y. From high entropy alloys to diluted multi-component alloys: range of existence of a solid-solution. Mater Des 2016;103:84–9. https://doi.org/10.1016/j.matdes.2016.04.046.

[29] Li BS. Microstructure formation mechanisms and properties of micro/nano structured high-entropy alloys and composites. Ph. D. thesis. HIT, China: School of Materials Science and Engineering; 2012.

[30] Ma D, Yao M, Pradeep KG, Tasan CC, Springer H, Raabe D. Phase stability of non-equiatomic CoCrFeMnNi high entropy alloys. Acta Mater 2015;98:288–96. https://doi.org/10.1016/j.actamat.2015.07.030.

[31] Yao MJ, Pradeep KG, Tasan CC, Raabe D. A novel, single phase, non-equiatomic FeMnNiCoCr high-entropy alloy with exceptional phase stability and tensile ductility. Scripta Mater 2014;72:5–8. https://doi.org/10.1016/j.scriptamat.2013.09.030.

[32] Stepanov ND, Shaysultanov DG, Tikhonovsky MA, Salishchev GA. Tensile properties of the Cr-Fe-Ni-Mn non-equiatomic multicomponent alloys with different Cr content. Mater Des 2015;87:60–5. https://doi.org/10.1016/j.matdes.2015.08.007.

[33] Li Z, Pradeep KG, Deng Y, Raabe D, Tasan CC. Metastable high-entropy dual-phase alloys overcome the strength-ductility trade-off. Nature 2016;534:227–30. https://doi.org/10.1038/nature17981.

[34] Hu R, Jin S, Sha G. Application of atom probe tomography in understanding high entropy alloys: 3D local chemical compositions in atomic scale analysis. Prog Mater Sci 2022;123:100854. https://doi.org/10.1016/j.pmatsci.2021.100854.

[35] Alaneme KK, Okotete EA. Recrystallization mechanisms and microstructure development in emerging metallic materials: a review. J Sci: Adv Mater Devices 2019;4:19–33. https://doi.org/10.1016/j.jsamd.2018.12.007.

[36] Sathiaraj GD, Pukenas A, Skrotzki W. Texture formation in face-centered cubic high-entropy alloys. J Alloys Compd 2020;826:154183. https://doi.org/10.1016/j.jallcom.2020.154183.

[37] Alaneme KK, Anaele JU, Bodunrin MO. Hot deformation processing of shape memory alloys: a review of effects on plastic flow behaviour, deformation mechanisms, and functional characteristics. Alex Eng J 2022;61:12759–83. https://doi.org/10.1016/j.aej.2022.06.055.

[38] Alaneme KK, Okotete EA. Enhancing plastic deformability of Mg and its alloys—a review of traditional and nascent developments. J Magnesium Alloys 2017;5:460–75. https://doi.org/10.1016/j.jma.2017.11.001.

[39] Patnamsetty M, Ghosh S, Somani MC, Peura P. Characterization of hot deformation behavior of Al0.3CoCrFeNi high- entropy alloy and development of processing map. J Alloys Compd 2022;914:165341. https://doi.org/10.1016/j.jallcom.2022.165341.

[40] Alaneme KK, Kareem SA, Olajide JL, Sadiku RE, Bodunrin RMO. Computational biomechanical and biodegradation integrity assessment of Mg-based biomedical devices for cardiovascular and orthopedic applications: a review. Int J Lightweight Mater Manuf 2022;5:251–66. https://doi.org/10.1016/j.ijlmm.2022.02.003.

[41] Alaneme KK, Anaele JU, Kareem SA. Hot deformability, microstructural evolution and processing map assessment of high entropy alloys: a systematic review. J Mater Res Technol 2023;26:1754–84. https://doi.org/10.1016/j.jmrt.2023.07.242.

[42] Savaedi Z, Motallebi R, Mirzadeh H. A review of hot deformation behavior and constitutive models to predict flow stress of high-entropy alloys. J Alloys Compd 2022;903:163964. https://doi.org/10.1016/j.jallcom.2022.163964.

[43] Tran MT, Nguyen TH, Kim DK, Woo W, Choi SH, Lee HW, Wang H, Kim JG. Effect of hot isostatic pressing on the cryogenic mechanical properties of CrCoNi medium entropy alloy processed by direct energy deposition. Mater Sci Eng, A 2021;828:142110. https://doi.org/10.1016/j.msea.2021.142110.

[44] Liao YC, Chen PS, Tsai PH, Jang JSC, Hsieh KC, Chang HW, Chen CY, Huang JC, Wu HJ, Lo YC, Huang CW, Tsao IY. Effect of thermomechanical treatment on the microstructure evolution and mechanical properties of lightweight $Ti_{65}(AlCrNb)_{35}$ medium-entropy alloy. Intermetallics 2022;143:107470. https://doi.org/10.1016/j.intermet.2022.107470.

[45] Kwon H, Sathiyamoorthi P, Karthik GM, Asghari-Rad P, Zargaran A, Kim HS. 2.3 GPa cryogenic strength through thermal-induced and deformation-induced body-centered cubic martensite in a novel ferrous medium entropy alloy. Scripta Mater 2021;204:114157. https://doi.org/10.1016/j.scriptamat.2021.114157.

[46] Jiang W, Cao Y, Yuan S, Zhang Y, Zhao Y. Creep properties and deformation mechanisms of a $Ni_2Co_1Fe_1V_{0.5}Mo_{0.2}$ medium-entropy alloy. Acta Mater 2023;245:118590. https://doi.org/10.1016/j.actamat.2022.118590.

[47] Chen PS, Shiu SJ, Tsai PH, Liao YC, Jang JS, Wu HJ, Chang SY, Chen CY, Tsao IY. Remarkable enhanced mechanical properties of TiAlCrNbV medium-entropy alloy with Zr additions. Materials 2022;15(18). https://doi.org/10.3390/ma15186324.

[48] He G, Zhao Y, Gan B, Sheng X, Liu Y, Tan L. Mechanism of grain refinement in an equiatomic medium-entropy alloy CrCoNi during hot deformation. J Alloys Compd 2020;815:152382. https://doi.org/10.1016/j.jallcom.2019.152382.

[49] Guan B, Wang Y, Li J, Zhang Y, Wang H, Xin Y. Comprehensive study of strain hardening behavior of CrCoNi medium- entropy alloy. J Alloys Compd 2021;882:1–9. https://doi.org/10.1016/j.jallcom.2021.160623.

[50] Liu Y, He G, Yang Y, Li K, Gong H, Gan B, Huang C. Revealing the microstructural evolution and mechanism during the thermomechanical treatment of polycrystalline CrCoNi medium-entropy alloy. J Alloys Compd 2021;870:159518. https://doi.org/10.1016/j.jallcom.2021.159518.

[51] Wang HJ, Hu ZT, Cao JS, Zhuang S, Cheng T, Wang QY. Hot deformation and workability of a CrCoNi medium entropy alloy. Met Mater Int 2022;28(2):514–22. https://doi.org/10.1007/s12540-021-01057-9.

[52] Yi HL, Wei D, Wang Y, Wang L, Fang MY, Yang K, Kato H. Hot deformation and dynamic recrystallization behaviour of CoCrNi and (CoCrNi)94Ti3Al3 medium entropy alloys. Metals 2020;10(10):1341. https://doi.org/10.3390/met10101341.

[53] Qiao L, Zhu J. Constitutive modeling of hot deformation behavior of AlCrFeNi multi-component alloy. Vacuum 2022;201:111059. https://doi.org/10.1016/j.vacuum.2022.111059.

[54] Yan X, Zhang Y. A body-centered cubic $Zr_{50}Ti_{35}Nb_{15}$ medium-entropy alloy with unique properties. Scripta Mater 2020;178:329–33. https://doi.org/10.1016/j.scriptamat.2019.11.059.

[55] Lee D, Agustianingrum MP, Park N, Tsuji N. Synergistic effect by Al addition in improving mechanical performance of CoCrNi medium-entropy alloy. J Alloys Compd 2019;800:372–8. https://doi.org/10.1016/j.jallcom.2019.06.005.

[56] M. Schneider, G. Laplanche, Effects of temperature on mechanical properties and deformation mechanisms of the equiatomic CrFeNi medium-entropy alloy, Acta Mater. 204 2021 116470, http://doi.org/10.1016/j.actamat.2020.11.012.

[57] Yang Y, Chen T, Tan L, Poplawsky JD, An K, Wang Y, Samolyuk GD, Littrell K, Lupini AR, Borisevich A, George EP. Bifunctional nanoprecipitates strengthen and ductilize a medium-entropy alloy. Nature 2021;595:245–9. https://doi.org/10.1038/s41586-021-03607-y.

[58] Weng F, Chew Y, Zhu Z, Yao X, Wang L, Ng FL, Liu S, Bi G. Excellent combination of strength and ductility of CoCrNi medium entropy alloy fabricated by laser aided additive manufacturing. Addit Manuf 2020;34:101202. https://doi.org/10.1016/j.addma.2020.101202.

[59] Liua Y, Hea G, Yang Y, Li K, Gong H, Gan B, Huang C. Revealing the microstructural evolution and mechanism during the thermomechanical treatment of polycrystalline CrCoNi medium-entropy alloy. J Alloys Compd 2021;870:159518. https://doi.org/10.1016/j.jallcom.2021.159518.

[60] Fu A, Liu B, Li Z, Wang B, Cao Y, Liu Y. Dynamic deformation behavior of a FeCrNi medium entropy alloy. J Mater Sci Technol 2022;100:120–8. https://doi.org/10.1016/j.jmst.2021.05.049.

[61] Park JM, Moon J, Bae JW, Jang MJ, Park J, Lee S, SeopKim H. Strain rate effects of dynamic compressive deformation on mechanical properties and microstructure of CoCrFeMnNi high-entropy alloy. Mater Sci Eng: A 2018;719:155–63. https://doi.org/10.1016/j.msea.2018.02.031.

[62] Su J, Raabe D, Li Z. Hierarchical microstructure design to tune the mechanical behavior of an interstitial TRIP-TWIP high-entropy alloy. Acta Mater 2019;163:40–54. https://doi.org/10.1016/j.actamat.2018.10.017.

[63] Wang Y, Zhao G, Xu X, Chen X, Zhang C. Constitutive modeling, processing map establishment and microstructure analysis of spray deposited Al-Cu-Li alloy 2195. J Alloys Compd 2019;779:735–51. https://doi.org/10.1016/j.jallcom.2018.11.289.

[64] Tan L, Li Y, He G, Liu F, Nie Y, Jiang L. Optimized hot workability of a powder metallurgy nickel-base superalloy. Mater Char 2019;147:340–52. https://doi.org/10.1016/j.matchar.2018.11.023.

[65] Choi M, Ondicho I, Park N, Tsuji N. Strength–ductility balance in an ultrafine-grained non-equiatomic $Fe_{50}(CoCrMnNi)_{50}$ medium-entropy alloy with a fully recrystallized microstructure. J Alloys Compd 2019;780:959–66. https://doi.org/10.1016/j.jallcom.2018.11.265.

[66] Jiang W, Yuan S, Cao Y, Zhang Y, Zhao Y. Mechanical properties and deformation mechanisms of a $Ni_2Co_1Fe_1V_{0.5}Mo_{0.2}$ medium-entropy alloy at elevated temperatures. Acta Mater 2021;213:116982. https://doi.org/10.1016/j.actamat.2021.116982.

[67] Gu J, Song M. Annealing-induced abnormal hardening in a cold rolled CrMnFeCoNi high entropy alloy. Scripta Mater 2019;162:345–9. https://doi.org/10.1016/j.scriptamat.2018.11.042.

[68] Zhang L, Zhang L, Wang H, Li J, Man J, Xu Z, Yu J, Wan G, Wang W, Wu B. Evolution of the microstructure and mechanical properties of a sigma hardened high-entropy alloy at different annealing temperatures. Mater Sci Eng: A 2022;831:142140. https://doi.org/10.1016/j.msea.2021.142140.

[69] Gu L, Liang N, Zhang D, Fan Y, Liu J, Zhao Y, Y. Tailoring microstructure of Ni_2CoFe medium entropy alloy to achieve optimal comprehensive mechanical properties. J Mater Res Technol 2023;23:4258–67. https://doi.org/10.1016/j.jmrt.2023.02.066.

[70] Wang Y, Liu B, Yan K, Wang M, Kabra S, Chiu YL, Dye D, Lee PD, Liu Y, Cai B. Probing deformation mechanisms of a FeCoCrNi high-entropy alloy at 293 and 77 K using in situ neutron diffraction. Acta Mater 2018;154:79–89. https://doi.org/10.1016/j.actamat.2018.05.013.

[71] Hua D, Xia Q, Wang W, Zhou Q, Li S, Qian D, Shi J, Wang H. Atomistic insights into the deformation mechanism of a CoCrNi medium entropy alloy under nanoindentation. Int J Plast 2021;142:102997. https://doi.org/10.1016/j.ijplas.2021.102997.

[72] de Silva Septimio R, Button ST, Van Tyne CJ. Processing maps for the analysis of hot workability of microalloyed steels 38MnSiVS5 and 0.39 C1.47Mn. J Mater Sci 2016;51:2512–28. https://doi.org/10.1007/s10853-015-9563-2.

[73] Zhu Y, Cao Y, He Q, Zhang J, Luo R, Di H, Huang G, Liu Q. Three-dimensional hot processing map of a nickel-based superalloy (Alloy 925) established by modified artificial neural network model. Intermetallics 2022;141:107423. https://doi.org/10.1016/j.intermet.2021.107433.

[74] Prasad YVRK. Processing maps: a status report. J Mater Eng Perform 2003;12:638–45. https://doi.org/10.1361/105994903322692420.

[75] Prasad YVRK, Gegel HL, Doraivelu SM, Malas JC, Morgan JT, Lark KA, Barker DR. Modeling of dynamic material behavior in hot deformation: forging of Ti-6242. Metall Mater Trans 1984;15:1883–92. https://doi.org/10.1007/BF02664902.
[76] Prasad YVRK, Sasidhara S. Hot working guide: a compendium of processing maps. Materials Park, OH: ASM International; 1997.
[77] Zhang H, Chen K, Zhou H, Shi C, Qin S, Liu J, Lv T, Xu J. Hot deformation behavior and processing map of a novel CFeNi$Si_{0.15}$ medium entropy alloy. Available at: SSRN. 2023. https://doi.org/10.2139/ssrn.4333715. https://ssrn.com/abstract=4333715.
[78] Derazkola HA, Garcia E, Murillo-Marrodán A, Conde Fernandez A. Review on modeling and simulation of dynamic recrystallization of martensitic stainless steels during bulk hot deformation. J Mater Res Technol 2022;18:2993–3025. https://doi.org/10.1016/j.jmrt.2022.03.179.
[79] Wang P, Liang M, Ma X, Xu X, Li J. Hot deformation constitutive analysis and processing maps of Cu-18 wt.% Nb composite wires. J Mater Eng Perform 2023. https://doi.org/10.1007/s11665-023-08008-y.
[80] Prasad YVRK, Rao KP, Sasidhar S. Hot working guide: a compendium of processing maps. Materials Park: ASM International; 2015. p. 1–29.
[81] Kang J, Wang Y, Wang Z, Zhao Y, Peng Y, Wang T. Hot deformation behavior and processing maps of Fe-30Mn-0.11C steel. Materials 2018;11(10):1940. https://doi.org/10.3390/ma11101940.
[82] Gao P, Chen L, Luo R, Peng CT, Sheng D, Liu T, Cheng X. Investigation of hot working performance and microstructure evolution of GH1059 superalloy based on processing map. Trans Indian Inst Met 2021;74:2729–37. https://doi.org/10.1007/s12666-021-02354-y.
[83] Neethu N, Chakravarthy P. Development of processing maps for hot deformation: algorithm and common errors. Metall Mater Trans 2020;51:3398–402. https://doi.org/10.1007/s11661-020-05817-x.
[84] Prasad YVRK. Processing maps: a status report. J Mater Eng Perform 2013;22:2867–74. https://doi.org/10.1007/s11665-013-0732-7.
[85] Lakshmi AA, Rao CS, Gangadhar J, Srinivasu C, Singh SK. Review of processing maps and development of qualitative processing maps. Mater Today Proc 2017;4(2):946–56. https://doi.org/10.1016/j.matpr.2017.01.106.
[86] Nayan N, Singh G, Narayana Murty SVS, Jha AK, Pant AB, George KM. High-temperature deformation processing map approach for obtaining the desired microstructure in a multi-component (Ni-Ti-Cu-Fe) alloy. Metall Mater Trans 2015;46:2201–15. https://doi.org/10.1007/s11661-015-2799-2.
[87] Sun B, Zhang T, Song L. Flow behavior and dynamic recrystallization of a power metallurgy nickel-based superalloy during hot compression in ($\gamma + \gamma'$)-phase region. J Alloys Compd 2022;891. https://doi.org/10.1016/j.jallcom.2021.161944.
[88] Motallebi R, Savaedi Z, Mirzadeh H. Additive manufacturing – a review of hot deformation behavior and constitutive modeling of flow stress. Curr Opin Solid State Mater Sci 2022;26(3):100992. https://doi.org/10.1016/j.cossms.2022.100992.
[89] Wang D, Zhu Q, Wei Z, Lin B, Jing Y, Misra RDK, Li J. Hot deformation behaviors of AZ91 magnesium alloy: constitutive equation, ANN-based prediction, processing map and microstructure evolution,". J Alloys Compd 2022;908:164580. https://doi.org/10.1016/j.jallcom.2022.164580.
[90] Zhou Y, Chen XM, Qin S. A strain-compensated constitutive model for describing the hot compressive deformation behaviors of an aged Inconel 718 superalloy. High Temp Mater Process 2019;38:436–43. https://doi.org/10.1515/htmp-2018-0108.
[91] Lv S, Jia C, He X, Wan Z, Li Y, Qu X. Hot deformation characteristics and dynamic recrystallization mechanisms of a novel nickel-based superalloy. Adv Eng Mater 2020;22(12):4553. https://doi.org/10.1002/adem.202000622.
[92] Venkatesh B, Khan F, Sahoo BN, Panigrahi SK. A high temperature manufacturability study of ultrafine grained Magnesium Rare-Earth alloy using processing map and constitutive analysis. J Alloys Compd 2023;954:169991. https://doi.org/10.1016/j.jallcom.2023.169991.
[93] Su Z, Wan L, Sun C, Cai Y, Yang D. Hot deformation behavior of AZ80 magnesium alloy towards optimization of its hot workability. Mater Char 2016;122:90–7. https://doi.org/10.1016/j.matchar.2016.10.026.
[94] Hedayati-Marzbali M, Jafarian HR, Park N. Understanding hot deformation behavior and microstructural evolution in a novel $Fe_{50}(CoCrMnNi)_{50}$ medium entropy alloy. J Mater Res Technol 2023;27:3396–410. https://doi.org/10.1016/j.jmrt.2023.10.033.
[95] Liu Y, Ning Y, Yao Z, Li H, Miao X, Li Y, Zhao Z. Plastic deformation and dynamic recrystallization of a powder metallurgical nickel-based superalloy. J Alloys Compd 2016;675:73–80. https://doi.org/10.1016/j.jallcom.2016.03.093.
[96] Mei RB, Bao L, Huang F, Zhang X, Qi XW, Liu XH. Simulation of the flow behavior of AZ91 magnesium alloys at high deformation temperatures using a piecewise function of constitutive equations. Mech Mater 2018;125:110–20. https://doi.org/10.1016/j.mechmat.2018.07.011.
[97] Mirzaie T, Mirzadeh H, Cabrera JM. A simple Zerilli–Armstrong constitutive equation for modeling and prediction of hot deformation flow stress of steels. Mech Mater 2016;94:38–45. https://doi.org/10.1016/j.mechmat.2015.11.013.
[98] Seif CY, Hage IS, Hamade RF. Extracting HCP Zerilli-Armstrong material parameters for magnesium alloy AZ31B from orthogonal cutting tests. J Mater Process Technol 2021;290:116982. https://doi.org/10.1016/j.jmatprotec.2020.116982.
[99] Qiao L, Inoue J, Zhu J. Machine learning guided constitutive model and processing map for Fe2Ni2CrAl1.2 multi-principle element alloys. J Mater Res Technol 2024;29:353–63. https://doi.org/10.1016/j.jmrt.2024.01.119.
[100] Babbar N, Kumar A, Verma VK. Crop management: wheat yield prediction and disease detection using an intelligent predictive algorithms and metrological parameters. In: Deep learning for sustainable agriculture; 2022. p. 273–95. https://doi.org/10.1016/B978-0-323-85214-2.00006-9.
[101] Abiodun OI, Jantan A, Omolara AE, Dada KV, Mohamed NA, Arshad H. State-of-the-art in artificial neural network applications: a survey. Heliyon 2018;4:e00938. https://doi.org/10.1016/j.heliyon.2018.e00938.
[102] Kareem SA, Anaele JU, Aikulola EO, Olanrewaju OF, Omiyale BO, Bodunrin MO. Hot deformation behaviour, constitutive model description, and processing map analysis of superalloys: an overview of nascent developments. J Mater Res Technol 2023;26:8624–69. https://doi.org/10.1016/j.jmrt.2023.09.180.
[103] Qiao L, Deng Y, Wang Y, Zhu J. A comparative study on Arrhenius equations and BP neural network models to predict hot deformation behaviors of a hypereutectoid steel. IEEE Access 2020;8:68083–90. https://doi.org/10.1109/ACCESS.2020.2986389.
[104] Wang J, Zhu B, Hui CY, Zehnder AT. Determination of material parameters in constitutive models using adaptive neural network machine learning. J Mech Phys Solid 2023;177:105324. https://doi.org/10.1016/j.jmps.2023.105324.
[105] Du JP, Yu P, Shinzato S, Meng FS, Sato Y, Li Y, Fan Y, Ogata S. Chemical domain structure and its formation kinetics in CrCoNi medium-entropy alloy. Acta Mater 2022;240:118314. https://doi.org/10.1016/j.actamat.2022.118314.
[106] Cigizoglu HK, Alp M. Generalized regression neural network in modelling river sediment yield. Adv Eng Software 2006;37:63–8. https://doi.org/10.1016/j.advengsoft.2005.05.002.
[107] Ding L, Rangaraju P, Poursaee A. Application of generalized regression neural network method for corrosion modeling of steel embedded in soil. Soils Found 2019;59:474–83. https://doi.org/10.1016/j.sandf.2018.12.016.
[108] Martínez F, Charte F, Frías MP, Martínez-Rodríguez AM. Strategies for time series forecasting with generalized regression neural networks. Neurocomputing 2022;491:509–21. https://doi.org/10.1016/j.neucom.2021.12.028.
[109] Specht DF. A general regression neural network. IEEE Trans Neural Network 1991;2:568–76. https://doi.org/10.1109/72.97934.
[110] Wang L, Zhou X, Zhu X, Dong Z, Guo W. Estimation of biomass in wheat using random forest regression algorithm and remote sensing data. Crop J ;4:212–9. https://doi.org/10.1016/j.cj.2016.01.008.
[111] Dewangan SK, Nagarjuna C, Jain R, Kumawat RL, Kumar V, Sharma A, Ahn B. Review on applications of artificial neural networks to develop high entropy alloys: a state-of-the-art technique. Mater Today Commun 2023;37:107298. https://doi.org/10.1016/j.mtcomm.2023.107298.
[112] Chen KT, Wei TJ, Li GC, Chen MY, Chen YS, Chang SW, Yen HW, Chen CS. Mechanical properties and deformation mechanisms in CoCrFeMnNi high entropy alloys: a molecular dynamics study. Mater Chem Phys 2021;271:124912. https://doi.org/10.1016/j.matchemphys.2021.124912.
[113] Pan Z, Fu Y, Wei Y, Yan X, Luo H, Li X. Deformation mechanisms of TRIP–TWIP medium-entropy alloys via molecular dynamics simulations. Int J Mech Sci 2022;219:107098. https://doi.org/10.1016/j.ijmecsci.2022.107098.
[114] Zhang C, Han B, Shi M. The effects of grain size and temperature on mechanical properties of CoCrNi medium-entropy alloy. J Mol Model 2023;29:104. https://doi.org/10.1007/s00894-023-05502-x.
[115] Pozhar LA. Transport properties of spatially inhomogeneous quantum systems from the first principles. In: Virtual synthesis of nanosystems by design. Elsevier; 2015. p. 3–60. https://doi.org/10.1016/B978-0-12-396984-2.00001-7.
[116] Tang L, Jiang FQ, Wróbel JS, Liu B, Kabra S, Duan RX, Luan JH, Attallah ZBMM, Nguyen-Manh D, Cai B. In situ neutron diffraction unravels deformation mechanisms of a strong and ductile FeCrNi medium entropy alloy. J Mater Sci Technol 2022;116:103–20. https://doi.org/10.1016/j.jmst.2021.10.034.
[117] Tang L, Jiang FQ, Wróbel JS, Liu B, Kabra S, Duan RX, Luan JH, Jiao ZB, Liu Y, Attallah MM, Nguyen-Manh D, Cai B. Deformation mechanisms of FeCrNi medium entropy alloy at 293 and 15 K. UKAEA Scientific Publications; 2021.
[118] Bodunrin M, Obiko J, Klenam D. On the uniaxial compression testing of metallic alloys at high strain rates: an assessment of DEFORM-3D simulation. Appl Sci 2023;13(4):2686. https://doi.org/10.3390/app13042686.
[119] Alaneme KK, Kareem SA, Bodunrin MO. Hyperbolic–sine constitutive model determined hot deformation mechanisms and workability response of Al–Zn/Cu and Al–Zn/SiC based composites. Results Eng 2023;19:101255. https://doi.org/10.1016/j.rineng.2023.101255.
[120] Qiao L, Ramanujan RV, Zhu J. Optimized hot working parameters of Fe2. 5Ni2. 5CrAl multi-principal element alloys. J Alloys Compd 2022;925:166594. https://doi.org/10.1016/j.jallcom.2022.166594.
[121] Qiao L, Deng Y, Liao M, Zhu J. Modelling and prediction of thermal deformation behaviors in a pearlitic steel. Mater Today Commun 2020;101134. https://doi.org/10.1016/j.mtcomm.2020.10113.

Sodiq Abiodun Kareem is a PhD candidate in the Department of Metallurgical and Materials Engineering, Federal University of Technology, Akure, Nigeria. His research interests include structure-property relationships in biomedical materials, metal matrix composites, shape memory alloys, high entropy alloys, and thermomechanical processing, among others.

Justus Uche Anaele is a lecturer I in the Department of Metallurgical and Materials Engineering, Federal University of Technology Owerri, Nigeria. He is a registered engineer with the Council for Regulation of Engineering in Nigeria (COREN) and is currently a PhD research student at the Department of Metallurgical and Materials Engineering, Federal University of Technology Akure, Nigeria.

Olajesu Favor Olarewaju is a PhD candidate in the Department of Material Science and Engineering, Iowa State University, USA.

Esther Dolapo Adewale is a Master of Engineering Graduate Student in the Department of Metallurgical and Materials Engineering, Federal University of Technology, Akure, Nigeria.

Nkemakolam Chikodinaka Osondu-Okoro is a Master of Engineering Graduate Student in the Department of Metallurgical and Materials Engineering, Federal University of Technology, Owerri, Nigeria.

Emmanuel Omosegunfunmi Aikulola is a Master of Engineering Graduate Student in the Department of Metallurgical and Materials Engineering, Federal University of Technology, Akure, Nigeria.

Samuel Olumide Falana is a Master of Engineering Graduate Student in the Department of Metallurgical and Materials Engineering, Federal University of Technology, Akure, Nigeria.

Bharat Gwalani is an Assistant Professor of Materials Science and Engineering at North Carolina State University, USA.

Michael Oluwatosin Bodunrin is a senior lecturer at the School of Chemical and Metallurgical Engineering, University of Witwatersrand, Johannesburg, South Africa. He is a registered engineer with the Council for Regulation of Engineering in Nigeria (COREN). His research interests include Titanium alloys, Metal Matrix Composites, Corrosion, Hot working, Tribocorrosion, DEFORM.

Kenneth Kanayo Alaneme is a professor in the Department of Metallurgical and Materials Engineering, Federal University of Technology Akure. He is currently the director of the Centre for Research and Development (CERAD), Federal University of Technology Akure, and a visiting professor at the University of Johannesburg, South Africa. He currently has close to 200 well-cited articles published in high-impact Journals and peer-reviewed conference proceedings.